EFFECT OF NANOPARTICLE INCLUSIONS AND SOLVENT ANNEALING ON BLOCK COPOLYMER MORPHOLOGY

A Thesis
Presented to
The Academic Faculty

by

Deepali Palta

In Partial Fulfillment
of the Requirements for the Degree
Doctor of Philosophy in the
School of Polymer, Textile and Fiber Engineering

Georgia Institute of Technology
December 2007

EFFECT OF NANOPARTICLE INCLUSIONS AND SOLVENT ANNEALING ON BLOCK COPOLYMER MORPHOLOGY

Approved by:

Dr. David Bucknall, Advisor
School of Polymer, Textile and Fiber Engineering
Georgia Institute of Technology

Dr. Lawrence Bottomley
School of Chemistry and Biochemistry
Georgia Institute of Technology

Dr. Haskell Beckham
School of Polymer, Textile and Fiber Engineering
Georgia Institute of Technology

Dr. J. Carson Meredith
School of Chemical and Biomolecular Engineering
Georgia Institute of Technology

Dr. Yonathan Thio
School of Polymer, Textile and Fiber Engineering
Georgia Institute of Technology

Dr. Mark Dadmun
Department of Chemistry
University of Tennessee

Date Approved: 22 August 2007

To the everlasting love and support of

my Dad, Col.(Dr.) S.C. Palta,

my mom, Sanyog

and my sister, Shaifali

ACKNOWLEDGEMENTS

First and foremost, I would like to express my gratitude to my advisor, David who had faith in me and gave me an opportunity to work with him as his first student in USA. He gave me independence in coming up with ideas for my work and helped me whenever things were tough. It was a wonderful experience working with him.

I would like to thank - Drs. Beckham, Bottomley, Dadmun, Meredith and Thio for serving on my thesis committee and for their most valued inputs. I would like to thank Dr. Beckham who allowed me to use his lab space whenever I needed a fume hood. Dr. Bottomley was always there to answer questions ranging from organic chemistry to intricacies of AFM measurements. Thanks to Dr. Henderson and his group for letting me use their ellipsometer through out my research work. I am grateful to Dr. Leisen for carrying out NMR experiments and Dr. Thio for his help with the CHESS experiments in New York. I am also thankful to Dr. Jacob and Dr. Griffin for their support and understanding.

There is a whole bunch of my colleagues/reseach scientists who have helped me on a day to day basis. I would like to thank Kane Barker (Chemistry Department), Dr. Philip Watson, Marcus Foston and Han Gi Chae for their helpful discussions relating different aspects of my project. Trevor Hoskins trained me on the ellipsometer. Matija Crene was always there in the lab next door to help me with the optical microscopes. Zhan Liu helped me with preparing the substrates for the last set of experiments. I was inspired by Dr. Philip Mcmullan - his teaching skills and his zest for making new things. Shaobo and Michelle (IPST) were very patient while training me on TEM. Thanks to Prashant and Neetu (Chemistry Department) for their help with the gold nanoparticle dispersion work.

I would like to thank the administrative staff - Mike, Angie, Hope and Linda. They were a great help in helping me take care of small things and of course, the paper work that I needed to do research effectively. I would like mention Dan Brooks as well because he was always there to help. I call him the "Muscle man" of the department.

Thanks to Xi and Bilge for making life easier especially during the last few months. Xi - I owe you a round of shots for volunteering to help me with CHESS experiments in New York. I am going to miss the endless "sarcasm", the laughs and of course, the daily ritual of getting coffee every morning. I have to thank my friends - Shakti, Swati, Wanting and Pratap for their unconditional friendship. Shakti and her husband Pushkar were my guardian angels in Atlanta especially in this last year when Anshul was not around. A special thanks to Ritwik Chatterjee who has been a great friend for almost eight years now.

I would like to thank my Papa, Mummy and my elder sister Shaifali for their constant encouragement via telephones to keep me pumped up and full of positive attitude through out writing. I would like to thank them for believing in me and trusting all my decisions. And, in the end, I would like to thank the love of my life - my husband, Dr. Anshul Dubey. He is my strength and I am the luckiest person on earth to have him by my side for the rest of my life. I love you Anshul.

TABLE OF CONTENTS

DEDICATION iii

ACKNOWLEDGEMENTS iv

LIST OF TABLES ix

LIST OF FIGURES x

GLOSSARY xiv

SUMMARY xviii

I INTRODUCTION 1

1.1 Motivation and Objectives 1

1.2 Scope of dissertation 2

II LITERATURE REVIEW 3

2.1 Block copolymers 3

2.1.1 Microphase Separation and Morphology 3

2.1.2 BCP thin films 9

2.1.3 Why use block copolymers for self assembly? 11

2.2 Nanoparticle templating 12

2.2.1 Templating approaches 12

2.2.2 Block copolymer nanotemplating 19

2.3 Long range ordering methods 26

2.3.1 Solvent vapor annealing 29

2.3.2 Shear field 32

2.3.3 Electric field alignment 34

2.3.4 Magnetic field alignment 35

2.3.5 Thermal gradients 36

III MATERIALS, METHODS AND TECHNIQUES 38

3.1 Block copolymer-nanoparticle composite studies 38

3.1.1 Materials . . . 38
3.1.2 Sample Preparation Methods . . . 39
3.1.3 Characterization techniques . . . 43
3.2 Long range order - Solvent annealing studies . . . 48
3.2.1 Materials . . . 48
3.2.2 Methods - thin film formation and solvent annealing . . . 50
3.2.3 Characterization techniques . . . 51
IV BULK COPOLYMER-NANOPARTICLE COMPOSITE STUDIES . . . 60
4.1 Gold nanoparticle inclusions . . . 60
4.1.1 Structure Analysis results . . . 60
4.1.2 Location of gold . . . 70
4.1.3 Discussion . . . 78
4.2 Fullerenes (C_{60}) inclusions . . . 86
4.3 Conclusions . . . 89
V LONG RANGE ORDERING (SOLVENT ANNEALING) STUDIES . . . 92
5.1 Solvent annealing effects on mica . . . 98
5.1.1 Ordering kinetics . . . 103
5.1.2 Degree of order . . . 105
5.2 Solvent annealing effects on Silicon wafer . . . 109
5.2.1 GISAXS Data Analysis . . . 109
5.2.2 Morphology of SBS-I films . . . 111
5.2.3 Effect of solvent exposure time . . . 113
5.2.4 Effect of incidence angle . . . 127
5.2.5 In-situ studies . . . 133
5.3 Conclusions . . . 136
VI CONCLUSIONS AND FUTURE DIRECTIONS . . . 138
6.1 Conclusions . . . 138
6.1.1 BCP-nanoparticle composite studies . . . 138

6.1.2 Solvent annealing studies 139
6.2 Future directions 140
6.2.1 BCP-nanoparticle composite studies 140
6.2.2 Solvent annealing studies 141
APPENDIX A THIN FILM STUDIES - (DEWETTING) 142
REFERENCES 145

LIST OF TABLES

1 Characteristics of the different triblock and diblock copolymers used in these studies 39

2 Peak position of Bragg reflections for various BCP equilibrium structures 44

3 Properties of the solvents used for solvent annealing studies 50

4 Gaussian width (FWHM in nm^{-1}) of the primary SAXS peak for the BCP systems 80

5 SAXS data analysis - Dimensions (in nm) for BCP systems along with the corresponding morphologies 81

6 Characteristics of the BCP systems 82

7 Dimensions (in nm) for block copolymer with C_{60} inclusions 88

8 Order parameter determined from the orientation analysis of the AFM images of SBS-I 50 nm thick films annealed in DME and EAC vapors 108

9 Characteristics of the 1D GISAXS integral plots of the solvent annealed SBS-I films 125

LIST OF FIGURES

1 Theoretical phase diagram for block copolymer 5

2 BCP segregation regimes 5

3 Bulk block copolymer morphologies 6

4 Experimental phase diagram for PS-PI diblock copolymer 6

5 Triblock morphologies 7

6 Experimental phase map for a triblock copolymer 8

7 Configurations of lamellae in BCP film 9

8 Summary of potential and current Block copolymer enabled nanotechnologies 11

9 Summary of top-down approaches 13

10 Epitaxial self-assembly 16

11 Schematics to produce holes and dots in silicon nitride 18

12 Schematics to high density nanowire production 19

13 Gold nanoparticles in diblock copolymer 22

14 CdSe nanoparticles in PS-P2VP 23

15 Size selective nanoparticle distribution in PS-PEP 24

16 Selective segregation of CdS nanoparticles in P4VP phase of PS-P4VP copolymer 25

17 Gold templating using Osmium tetraoxide 26

18 CdSe nanoparticles in PS-P2VP 27

19 Mechanism of solvent annealing in a thin film 30

20 AFM phase images of PS-PEO - solvent annealing 32

21 Chemical structure of BCP 38

22 UV measurements on gold dispersions 42

23 Schematic layout of a SAXS set up 44

24 SAXS for block copolymer morphology 45

25 2D scattering data of silver behenate 46

26 General schematic of TEM 47
27 Contact angles for mica and piranha-treated silicon wafer 49
28 Solvent annealing chamber 51
29 Principle of Atomic force microscope 52
30 A typical example of AFM phase image in SBS 53
31 FFT insets of SBS-I 53
32 Schematics of GISAXS experimental set-up 54
33 Signature GISAXS patterns for a diblock copolymer film 55
34 A characteristic 2D GISAXS pattern 56
35 Set up for in-situ solvent annealing 56
36 Vector construction of specular reflectivity from a flat surface 57
37 X-ray reflectivity data corrections 58
38 SAXS patterns for SBS-I system 61
39 TEM images - effect of different percent gold on the phase morphology of SBS-I 64
40 SAXS patterns for SBS-II system 65
41 SAXS patterns for SB-I system 67
42 SAXS patterns for SB-I system 69
43 TEM of stained and unstained SBS-I with 1 % gold nanoparticles . . 72
44 ^{1}H NMR spin diffusion measurement 73
45 Spin diffusion NMR analysis within the mobile domain (PB and thiol capped gold) 74
46 NOESY - 2D exchange spectra at initial mixing time and at 200 ms . 76
47 NMR - Normalized intensity of the relative ratio of peaks as a function of mixing time 77
48 Schematic of gold location in the BCP system 77
49 FWHM of the primary peaks from the scattering data of BCP-gold nanoparticle systems 79
50 BCP domain spacing as a function of percent gold inclusions 82
51 Apparent volume fraction of PB in SBS-I and SBS-II with Au inclusions 83

52 Schematic of gold nanoparticles in a triblock copolymer 84

53 DSC thermograms for SBS-I and SBS-I with 1% gold inclusions . . . 85

54 Predicted phase diagram of a diblock copolymer - nanoparticle composite 85

55 SAXS patterns for bulk block copolymer with fullerene nanoparticle inclusions 87

56 TEM images - effect of different percent C_{60} on the phase morphology of SBS-I 90

57 Schematic of the location of C_{60} in BCP system 91

58 AFM phase images - effect of solvent annealing in the vapors of the spin casting solvent on 260 nm thick SBS-I (4%) film 93

59 AFM phase images - effect of different solvent vapors on 260 nm thick SBS (4%) film spun cast from toluene 95

60 AFM phase images of 50 nm thick SBS-I film spun cast from toluene (on mica) after 6 hours of solvent exposure 97

61 AFM phase images of 50 nm thick SBS-I annealed using dimethoxyethane 99

62 AFM phase images of 50 nm thick SBS-I annealed using ethyl acetate 101

63 Calculated effective interaction parameter as a function of solvent volume fraction 105

64 Filtering process of AFM images used for degree of order analysis . . 106

65 False color maps calculated using OAAP software of the degree of lateral order in 50 nm thick SBS-I films annealed using EAC and DME solvent vapors 107

66 Example of GISAXS data analysis 110

67 AFM micrographs of SBS-I (50 nm) film after DME-6 hour annealing 112

68 AFM micrographs of SBS-I (50 nm) film after DME-6 hour annealing 113

69 GISAXS plots for 50 nm thick SBS-I films annealed in toluene 115

70 GISAXS plots for 260 nm thick SBS-I films annealed in toluene . . . 115

71 GISAXS plots for 50 nm thick SBS-I films annealed in DME 117

72 GISAXS plots for 260 nm thick SBS-I films annealed in DME 117

73 GISAXS plots for 50 nm thick SBS-I films annealed in ethyl acetate . 119

74 GISAXS plots for 260 nm thick SBS-I films annealed in ethyl acetate 119

75 GISAXS plots for 50 nm thick SBS-I films annealed in cyclohexanone 122

76 GISAXS plots for 260 nm thick SBS-I films annealed in cyclohexanone 122

77 Comparison of different solvents used for annealing SBS-I films 124

78 Effective interaction parameter as a function of solvent volume fraction 126

79 2D GISAXS patterns at different incident angles for 50 nm SBS-I film annealed in DME for 6 hours 127

80 GISAXS data - Intensity of the peak as a function of the incident angle 129

81 Electron density as a function of the vertical distance for a 50 nm film 130

82 In-situ annealing on 50 nm SBS-I film 131

83 In-situ annealing on 50 nm SBS-I film 132

84 In-situ annealing on 50 nm SBS-I film 133

85 2D GISAXS plots for in-situ solvent annealing experiments 134

86 In-situ annealing on 50 nm SBS-I film 135

87 AFM micrographs of 50 nm SBS-I film with 1 (wt%) addition of gold (5 nm) particles 144

88 AFM micrographs of 50 nm SBS-I film with 3 (wt%) addition of gold (5 nm) particles 144

89 Optical micrographs of dewetted (after 10 days) 50 nm SBS-I film with different weight % addition of gold (5 nm) particles 144

90 Optical micrographs of annealed 50 nm SBS-I film with different weight % addition of gold (5 nm) particles 144

GLOSSARY

^{1}H NMR	Proton nuclear magnetic resonance spectroscopy.
AB	Diblock copolymer of polymer A and polymer B.
ABA	Triblock copolymer of polymer A and polymer B.
ABC	Triblock copolymer of polymers A, B and C.
AFM	Atomic force microscopy.
BCC	Body centered cubic.
BCP	Block copolymer.
χ	Interaction parameter.
χ_ϵ	Effective interaction parameter used in solvent annealing study.
d	Block copolymer repeat spacing.
δ_p	Solubility parameter of the polymer.
δ_s	Solubility parameter of the solvent.
DFT	Density functional theory.
dis	Disordered polymer.
DME	Dimethoxyethane.
DSC	Differential scanning calorimetry.
EAC	Ethyl acetate.
f	Volume fraction.
F	free energy of mixing for a diblock copolymer.
FWHM	Full width at half maximum.
γ_A	Surface energy of A.
γ_{AB}	Interfacial energy between A and B.
γ_B	Surface energy of B.
GISAXS	Grazing incidence small angle X-ray scattering.
gyr	Gyroid morphology.

HCP Hexagonal close packing.

HEX Hexagonal morphology.

$\mathbf{k}_i$ Angle of incidence for SAXS.

$\mathbf{k}_s$ Angle of scattering for SAXS.

L Block copolymer domain spacing.

LAM Lamellar morphology.

λ Wavelength of X-ray used for SAXS.

LAOS Large amplitude oscillatory shear.

LC Liquid crystalline.

MEK Methyl ethyl ketone.

$\mathbf{M}_n$ Number average molecular weight.

$\mathbf{N}_A$ Number of molecules of polymer A.

NMR Nuclear magnetic resonance spectroscopy.

NOESY 2D nuclear overhauser effect spectroscopy.

Np Nanoparticle.

ODT Order disorder transition.

P2VP Poly(2-vinylpyridine).

P2VP-SH Thiol terminated Poly(2-vinylpyridine).

P4VP Poly(4-vinylpyridine).

PB Polybutadiene.

PDMS Poly(dimethylsiloxane).

P(dS-b-MMA) Poly(deuterated styrene-b-methyl methacrylate).

PEE Poly(ethylethylene).

PEO Poly(ethylene oxide).

PEP Poly(ethylene propylene).

PFS Poly(ferrocenylsilane).

PI Polyisoprene.

PI-PLA Poly(isoprene-b-lactide).

PPO Poly(propylene oxide).

PS Polystyrene.

PS-b-PMMA Poly(styrene-b-methylmethacrylate).

PS-PFS Poly(styrene-b-ferrocenyldimethylsilane).

PS-SH Thiol terminated Polystyrene.

PVP Poly(vinyl pyridine).

Q Scattering vector for SAXS.

$\mathbf{R}_g$ Radius of gyration.

RIE Reactive ion etching.

ROMP Ring opening metathesis.

SAXS Small angle x-ray scattering.

SB Poly(styrene-b-butadiene).

SBS Poly(styrene-butadiene-styrene).

SC-CO_2 Supercritical state carbon dioxide.

SCFT Self consistent field theory.

Si Silicon.

SSL Strong segregation limit.

SWNT Single wall carbon nanotubes.

t Thickness of the block copolymer film.

T Temperature.

TEM Transmission electron microscope.

$\mathbf{T}_g$ Glass transition temperature.

TGA Thermogravimetric analysis.

θ Half the scattering angle for SAXS.

TOPO Tri-n-octylphosphine oxide.

UV-vis Ultra-violet visible.

v/v	Volume by volume.
WSL	Weak segregation limit.
w/v	Weight by volume.
w/w	Weight by weight.
ξ	Order paramter.
XPS	X-ray photoelectron spectroscopy.

SUMMARY

Using block copolymers for large-area periodic structure fabrication in potential applications like ultra-high density storage devices and quantum information computers is of great interest because of the potential for low fabrication costs and simplicity of the processing. The concept is that by selective inclusion of the nanoparticles into one of the blocks of a self-assembling copolymer, the nanoparticles are forced into a defined spatial arrangement determined by the phase morphology of the copolymer. Although copolymers can form well defined structures, they inherently have a 'polycrystalline' structure in the bulk, meaning that there is no long-range order of the domains. This thesis addresses both the effect of inclusion of the nanoparticles and the long range ordering of block copolymer domains.

The first part of the thesis focuses on the study of the effect of gold (5 nm diameter) and fullerene (C_{60} - 1 nm) nanoparticle inclusions on the phase morphology of the poly(styrene-butadiene) diblock and poly(styrene-butadiene-styrene) triblock copolymers. For gold inclusions, it was found that even at relatively low concentrations of inclusions (less than 1 wt./vol.%) the block copolymer phase morphology is altered from that of the native copolymer. TEM and solid-state NMR experiments have proved that the gold nanoparticles are only found in the bulk of the polybutadiene domains. By contrast to the block copolymer-gold system, no significant changes in bulk morphology is observed for fullerene concentrations up to 5 wt./vol.% except for poly(styrene-butadiene) system with a low volume fraction of PB minor component.

In the second part of the thesis, the evolution of the order in cylinder-forming poly(styrene-butadiene-styrene) triblock copolymer thin films as a function of the type of solvent vapor, exposure time to the saturated vapors and substrate surface

energy is discussed. We have shown that for a cylinder-forming block copolymer thin film, appropriate choice of substrate can be used to tune the alignment of the cylinders either perpendicular or parallel to the interface. Using solvent annealing, the incommensurate films spun cast on mica induces cylindrical phase domain alignment perpendicular to the interface with near perfect ordering but after extended exposure to the solvent vapors the cylinders reorient parallel to the surface. However, the same films spun cast on silicon wafers always form cylinders normal to the surface. Solvent vapors of dimethoxyethane, ethyl acetate and cyclohexanone were found to be the most effective in ordering the structure for our polymer films. Solvent vapors differing in their selectivity towards the block copolymer domains lead to different kinetics of ordering which is explained in terms of the difference in the interaction of the solvent between the two different copolymer blocks.

CHAPTER I

INTRODUCTION

1.1 Motivation and Objectives

Nanotechnology is widely seen as the corner-stone of the development of new materials and is often referred to as the "Next Industrial Revolution". The phrase "nanotechnology" is used to describe all kinds of research involving structures with characteristic dimensions of several hundred nanometers or less. Due to their intrinsic length scale, macromolecules are ideally suited as building blocks of nanostructured materials in the form of polymer-based self-assembled structures.

Fabrication of large-area periodic structures on the nanoscale using polymer based self-assembly is of great interest because of the potential simplicity and low cost of the process [1]. Out of all the polymer based systems, block copolymers are especially attractive for potential applications like electronic, optoelectronic and magnetic devices either as pure components or as a composite with nanoparticles [2]. Block copolymers have the desirable feature that their morphology can be systematically controlled by varying the number of blocks, their chemical compositions, and their characteristic dimensions [3]. However, self-assembly alone usually leads to polydomain structures with random orientation between the domains. These structures lack long range positional properties because the typical grain size over which the block copolymer is well defined is in the submicron range. For practical applications of lithography, for example in metal dot arrays, one should be able to address each dot independently. It is therefore of great importance to develop methods for long range order. In addition, it would be significant to understand the influence of inorganic nanoparticles on the phase behavior of block copolymers so that potential of nanocomposite materials

could be fully exploited. In the light of these factors, the objectives of this project are two-fold.

- to study changes in block copolymer bulk and thin film microstructures due to inclusions of inorganic nanoparticles.
- to understand and obtain long range ordering in block copolymer systems by macroscopic ordering of nanoscopic (phase separated) domains.

1.2 Scope of dissertation

Chapter 2 introduces and reviews the relevant literature. In Chapter 3, the sample preparation methods along with the various characterization techniques utilized, such as atomic force microscopy and small-angle x-ray scattering, are discussed. In Chapter 4, the effect of different sized nanoparticle inclusions in triblock and diblock bulk samples is discussed for a number of different polymers. Long range ordering in block copolymer thin films utilizing solvent vapor annealing is discussed in Chapter 5. In Chapter 6, the conclusions from this thesis are presented and possible lines of extension for future research are outlined.

CHAPTER II

LITERATURE REVIEW

2.1 Block copolymers

Block copolymers (BCP) are a class of macromolecules that are produced by covalent bonding two or more chemically distinct homopolymers. Depending upon the number (n) of constituent blocks, the nomenclature for such a polymer is diblock ($n = 2$), triblock ($n = 3$), etc. They represent a subject of wide interest in fields of macromolecular physics and chemistry because of their remarkable ability to self-assemble into a variety of ordered structures with nanoscale periodicities.

2.1.1 Microphase Separation and Morphology

In a diblock copolymer, AB, the two block components are usually immiscible in bulk. However, due to covalent bonding, the blocks cannot form macroscopically large phases of A and B, instead they minimize contacts with each other by exhibiting microphase separation and forming mesoscale periodic structures with a length scale on the order of R_g, where R_g is the copolymer radius of gyration [4].

This phase separation is driven by two opposing forces: unfavorable enthalpic interactions and entropic energy [5, 4]. In order to minimize the unfavorable contacts or interactions between different block types, the block phases separate locally and stretch. Stretching reduces the interfacial area between the domains, however, it also reduces the number of conformations at the same time. With respect of entropy, the blocks want to mix and favor less extended conformations, maximizing the number of possible conformations, i.e. the entropy. Thus, the enthalpic interactions tend to separate the BCPs, whereas entropically the polymers favor mixing. It depends critically on the temperature and the strength of interaction to decide which tendency

prevails. At elevated temperatures, the entropy dominates and the BCPs are in a disordered state. On reducing the temperature, the enthalpic interactions start to dominate and microphase separated structures are formed.

The microphase separation can be thermodynamically expressed in terms of Flory-Huggins theory for a system with two components A, with N_A molecules occupying a volume fraction *f*, and B, with N_B molecules occupying a volume fraction (1-*f*) [6]. For such a system, free energy of mixing, *F*, can be expressed as:

$$\frac{F}{(k_B T)} = \frac{f}{N_A} ln(f) + \frac{1-f}{N_B} ln(1-f) + \chi f(1-f) \tag{1}$$

where the first two terms are the entropic contributions (proportional to N_A and N_B respectively) and the third term accounts for the energetic penalty due to mixing. This latter term is proportional to χ, Flory-Huggins interaction parameter which is temperature dependent and can be expressed as:

$$\chi = \frac{\alpha}{T} + \beta \tag{2}$$

where T is the temperature and α and β are experimentally determined parameters which may depend on *f*, N and T. The system will phase separate only when the entropic term is overcome by the energy gain due to phase separation. Thus, the product χN represents the enthalpic-entropic balance and is used to characterize phase behavior of BCP together with the volume fraction of one block (f). Figure 1 represents the theoretical phase diagram for an AB diblock copolymer where the degree of segregation, χN is plotted as a function of *f*.

The presence or absence of microphase separation depends on the segregation strength between the blocks [8, 9]. At χN << 10, the polymer is disordered as the two polymers are miscible. The transition from a homogeneous melt of chains to ordered microphase separated domains is called the order-disorder transition (ODT). In symmetric diblock copolymers ($f = 0.5$), the critical value of χN for microphase separation is about 10.5. At χN $\sim$ 10, the system is in the weak segregation limit

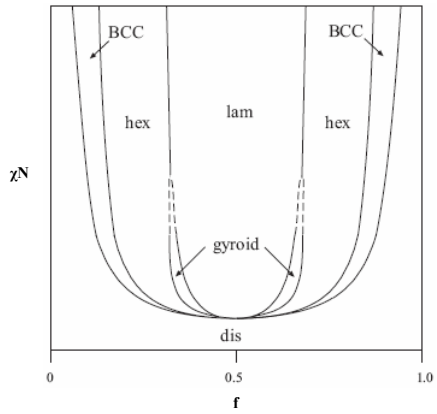

Figure 1: Theoretical phase diagram for a diblock copolymer (Reproduced from [7]).

(WSL) which is characterized by diffuse and non-distinct domains. The volume fraction of one of the blocks varies sinusoidally about the average value. For χN >> 10, the BCP system is in the strong segregation limit (SSL) where the interphase between the blocks is sharp and localized [8]. These regimes of segregation are depicted in Figure 2.

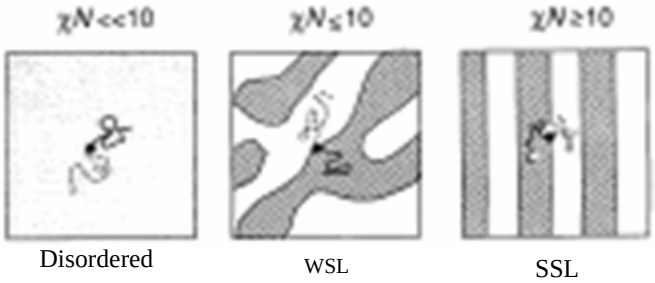

Figure 2: Various regimes of diblock copolymer phase separation (Reproduced and modified from [8]).

The morphology of the BCP resulting from the microphase separation is determined by the relative volume fraction f of each block as shown in Figure 3. As the volume fraction (f) of one component increases from 0 to $\sim$ 0.5, the morphology changes from body centered cubic (bcc) spheres to hexagonal (hex) cylinders, gyroid (gyr), and fnally lamellar (lam). At values of $f \geq 0.5$, the phases repeat themselves with the blocks reversed. Besides these common morphologies, other less frequently

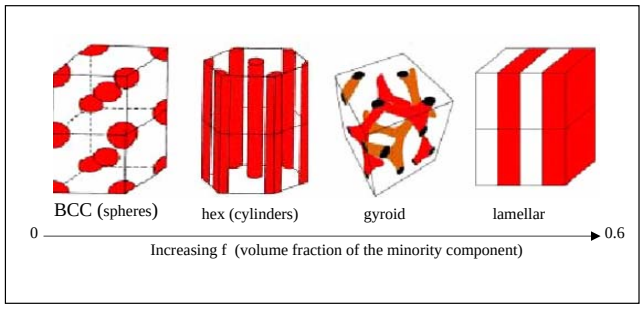

Figure 3: Schematics of morphologies based on increasing volume fractions (Reproduced from [10])

observed morphologies such as perforated-lamellar and perforated-hexagonal structures have been reported experimentally [11]. Figure 4 shows the well known experimental phase diagram for poly(styrene-b-isoprene) (PS-PI) diblock copolymer. Different morphologies were found for a series of diblock copolymers where the vol-

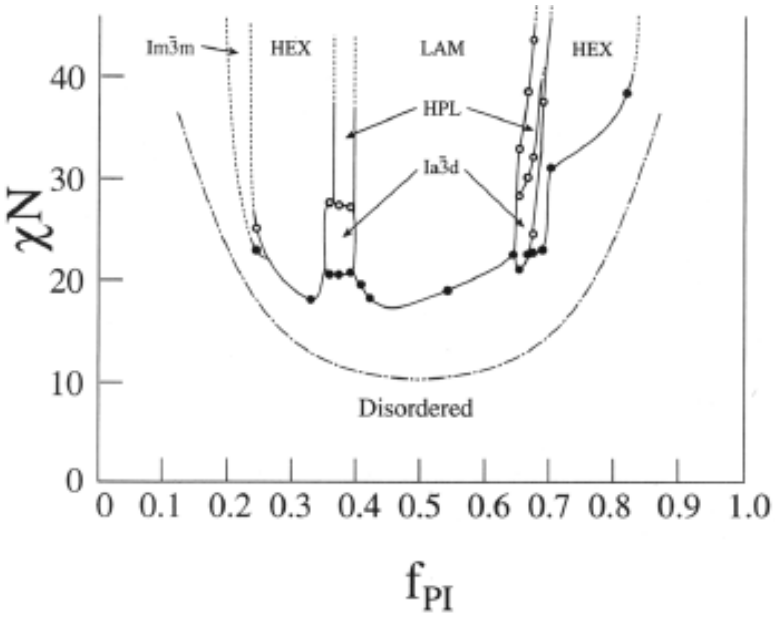

Figure 4: A χN vs. volume fraction of polyisoprene (f_{PI}) phase diagram for PS-PI diblock copolymer (Reproduced from [11]). The different morphologies shown in are : Im$\bar{3}$m = bcc spherical, HEX = hexagonally packed cylinders, HPL = hexagonally perforated lamellae, LAM = lamellar and Ia$\bar{3}$d = gyroid phases.

ume fraction of the polyisoprene (f_{PI}) was varied from 0.24 to 0.82 and five distinct morphologies - spherical (Im$\bar{3}$m), hexagonally packed cylinders (HEX), hexagonally

perforated lamellae (HPL), lamellar (LAM) and gyroid ($Ia\bar{3}d$) phases were observed. By contrast to the theoretical phase diagram (see Figure 1), the experimentally determined phase diagram is asymmetric about volume fraction, f =0.5 which results from the unequal statistical segment lengths of PS and PI. The HPL structure was later found to be a metastable state [12].

In addition to diblock copolymers, triblock copolymers (ABA, ABC) offer the opportunity to create ordered morphologies simultaneously containing mesoscopic structures of different dimensionality. Some of the theoretically predicted morphologies for linear triblock (ABC) copolymers are shown in Figure 5 [13]. A number of different

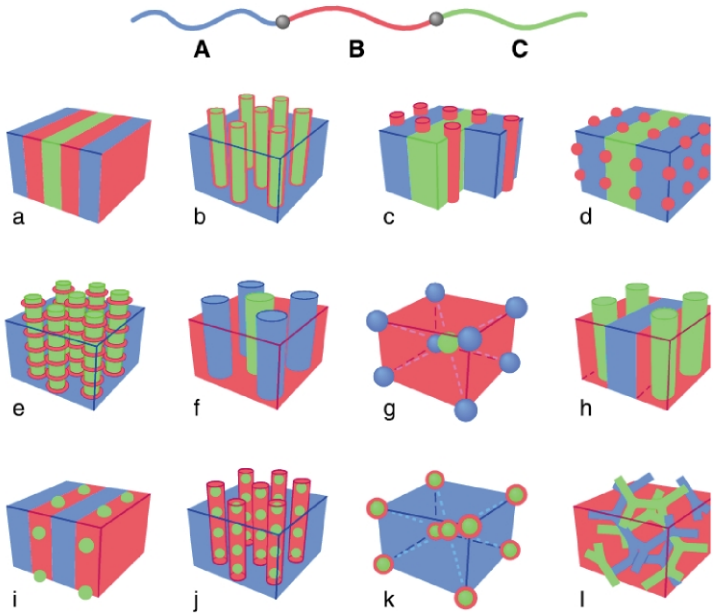

Figure 5: Schematic of morphologies possible in linear ABC triblock copolymers where the three blocks are represented in different colors (Reproduced from [14]).

possible morphologies in triblock copolymers have been studied experimentally by different groups [15, 16, 17]. A comprehensive phase map for poly(styrene-b-isoprene-b-ethylene oxide) (ISO) was plotted using a wide range of compositions at weak to intermediate segregation strengths. To achieve these results, nearly monodisperse ISO polymers were synthesized using living anionic polymerization and the resulting ordered phases were characterized using a variety of techniques including small

angle X-ray scattering, transmission electron microscopy and dynamic mechanical spectroscopy. Figure 6 shows the ternary phase diagram of ISO where the axes identify the volume fraction of each block and different colored circles represent different morphologies. Six ordered states were found - lamellar (LAM) (found in the center

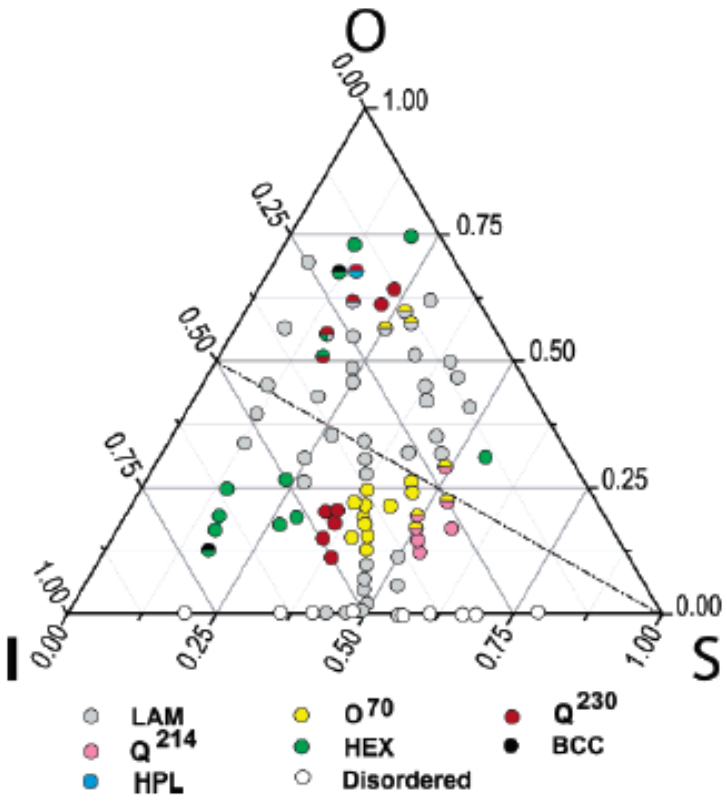

Figure 6: Phase map of poly(styrene-b-isoprene-b-ethylene oxide). The axes represent the volume fraction of each component and each structure is represented by an individual colors. Symbols with different color top and bottom halves represent the respective high and low temperature states of the order-order transitions (Reproduced from [17]).

of the phase diagram), hexagonal (HEX), double gyroid (Q^{230}), alternating gyroid (Q^{214}), spherical (BCC) and orthorhombic network (O^{70}). In addition to these ordered states, a metastable state of hexagonallly perforated lamellae (HPL) and mixed states of coexisting lamellar and hexagonal phases were also found. The complexity of this ternary phase diagram mirrors those of other systems in which a majority of the theoretically predicted triblock phase morphologies have been observed.

2.1.2 BCP thin films

Bulk BCP morphologies are typified by grains of ordered domains oriented randomly with respect to each other, much like the grain structure of small molecule or atomic crystals [18, 19]. In contrast, BCP thin films have an advantage of simultaneous microphase separation and oriented domains [20, 21].

In thin films, besides composition and molecular weight, the mesoscopic structure and orientation is dependent on the surface energies of the blocks and on geometrical constraints introduced by the confinement in a thin film [22]. Consequently, the presence of a substrate and/or a free surface introduces additional driving forces for morphological development due to preferential segregation of one block to the substrate or surface [23]. For a lamellae-forming diblock copolymer confined in a thin film, some of the possible configurations are shown in Figure 7. By convention, if the same block is found at each boundary, the BCP is said to have symmetric wetting. However, if one block preferentially wets the interface with the substrate or air, wetting is desribed as asymmetric. At equilibrium, symmetric films are stable at a total film thickness $t = nd$, whereas asymmetric films are stable at $t = (n+1/2)d$ where n is an integer $(n = 1, 2, 3, 4)$ and d is the BCP repeat spacing.

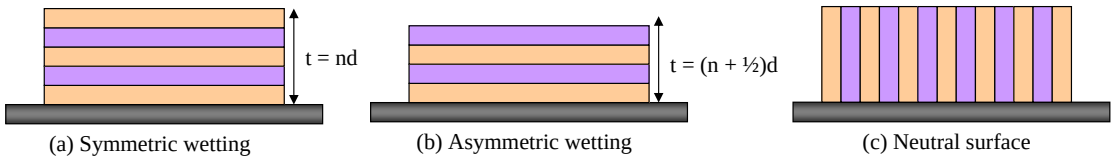

Figure 7: Possible configurations of lamellae in BCP films confined at one surface.

When the thickness of the film is not commensurate to the equilibrium lamellar spacing, either holes or islands are nucleated on the film surface to adjust the local film thickness to the preferred quantized values [24].

The influence of the confinement and the interfacial interactions on the morphology of diblock copolymers in thin films have been extensively studied theoretically

within mean field theories [25, 26, 27] and Monte Carlo simulations [28, 29]. The films are assumed to be confined between two surfaces thus, preventing formation of terraces. The calculations suggest that if there is no preference for blocks to wet the confining surfaces (neutral surface), the microdomains adopt perpendicular orientation having lower free energy, independently of gap between the confining surfaces [27]. For a surface showing substantial preference to one of the blocks, parallel orientation of microdomains is favored for all separation widths except when it equals $(n+1/2)d$ in the lamellar morphology and $(1/2)nd$ + 0.75 for the cylindrical morphology in the symmetrical wetting case, where the perpendicular orientation was observed [28]. This is explained by the fact that the interfacial interactions can not compensate for the increase of the free energy as a result of stretching or compression of chains to match the surface gap. The window of stability of the perpendicular orientation, however, gradually decreases with increasing surface separation and the surface interactions.

Ability to achieve a desired orientation of microdomains is crucial for a number of applications of BCPs in thin films. In practice, substrate-supported films with a free surface typically avoid perpendicular orientation by undergoing the formation of terraces. Indicative in this respect, are the results obtained by Kim and coworkers [30] who studied morphological evolution of a cylinder-forming poly(styrene-b-methyl methacrylate) (PS-PMMA) film having a thickness equal to the repeat spacing (d) upon annealing. Mismatch of the film thickness with the quantization relation resulted in the alignment of the cylinders normal to the film surface in the initial stages of annealing. The cylinders re-oriented in-plane when terraces of the height of the repeat spacing (d) were formed during later stages of annealing. In contrast, a stable lamellar morphology without the formation of terraces was observed for one period thick PS-PMMA films [31].

Recently, it was demonstrated by Russell et al. [32, 33, 34, 35] that PS-PMMA

films of the lamellar and cylindrical morphologies annealed on "neutral surfaces" adopt a perpendicular orientation, as theoretically predicted. Such neutral surfaces were obtained by deposition of random copolymer of appropriate composition.

2.1.3 Why use block copolymers for self assembly?

In diblock copolymers with well controlled architectures, equilibrium periodic structures can be selected by chemical design. By adjusting the degree of polymerization of the polymer, and the composition (volume fraction, f), the length scales associated with self assembled structures can be manipulated. The length scales typically are in the range of 10-200 nm [36, 22]. These length scales are also attractive for numerous potential applications where nanopatterning is required, such as in electronics, optoelectronics and magnetic storage devices. Thus, block copolymers are a good choice, both in terms of thermodynamics and dynamics of self-assembly systems to create new materials and patterns. Figure 8 summarizes some of the possible areas of nanotechnology where block copolymers could be used [14].

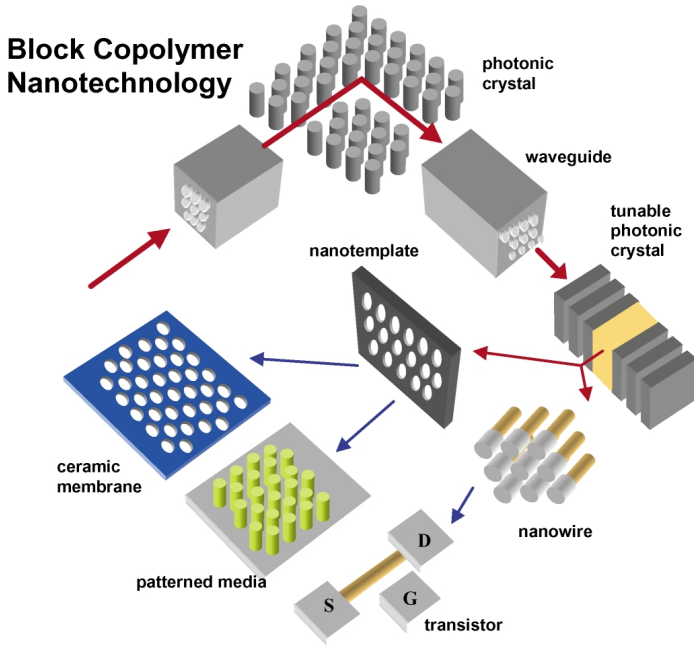

Figure 8: Summary of potential and current block copolymer enabled nanotechnologies (Reproduced from [14]).

2.2 Nanoparticle templating

Nanoparticles are a key component in the field of nanotechnology. One of the advantages of using nanoparticles is their large surface area-to-volume ratios. Nanoparticles can serve as fillers in a host of polymer matrices so that by using a small amount of material, a desired property could be achieved without much weight increase [37]. To realize the full potential of nanoparticles, fabrication of precisely ordered nanoscale structures is often essential. This would require templating these particles with precise control and uniform spacing to get a macroscopic order. This is best approached by directed assembly of materials through the interaction with a template.

2.2.1 Templating approaches

There are essentially two basic approaches of templating used to fabricate nanostructures, called top-down and the bottom-up approaches. Top-down fabrication, in general, refers to the traditional methods developed by the semiconductor industry in which a pattern is transferred from a master template into an underlying substrate. In bottom-up fabrication, the active components are directly self-assembled from the atomic or molecular level in scale.

2.2.1.1 Top-down approaches

Top-down approaches were outlined as early as 1959 when Richard Feynman suggested that large machines would be used to build smaller machines, which would build yet smaller machines, working towards molecular dimensions [38]. The top-down approach uses lithography, where the basic principle involves exposure of an appropriate material to electromagnetic radiation through a pattern mask which introduces a latent image into the material as a result of a set of chemical changes in its molecular structure, This latent image is then developed into a relief structure in the underlying substrate through selective etching. Figure 9 provides a summary of popular top-down methods with their inherent advantages and limitations [14].

Technique	Minimum resolution (nm)	Source materials	Nature of patterns	Intrinsic limitations	Advantages
UV photo lithography	250	248 nm KrF excimer laser	2D	Diffraction depth of focus	Easy replication
X-ray lithography	25	Soft X-ray with near 1nm	2D	Diffraction depth of focus	Easy replication
Interference lithography	>100	Holographic interactions between two or more lasers	2D, 3D	Diffraction depth of focus limited patterns	No mask easy replication
Zone plate array lithography	>100	Fresnel zone plates X-ray beam	2D	Zone plate fabrication	No mask
Near-field scanning optical lithography	~ 100	UV or VIS laser with fiber optic probe	2D	Serial patterning	No diffraction limit
Focused ion beam lithography	~ 50	Focused ion beam	2D	Electrostatic interactions serial writing small field writing	Writing pattern
Electron beam lithography	10–30	Focused electron beam	2D	Electrostatic interactions serial writing small field writing	Writing pattern
Nanografting	5–50	Modified AFM tip	2D	Serial patterning limited writing speed	High resolution arbitrary geometries chemical patterns
Dip-pen lithography	5–50	Modified AFM tip	2D	Serial patterning limited writing speed	High resolution arbitrary geometries chemical patterns
Nano imprint lithography	10–40	Stamp and polymeric resist	2D	Fabrication of stamp multi-step process alignment fidelity	High resolution large area printing relatively low cost

Figure 9: Summary of top-down approaches (Reproduced from [14]).

Polymeric materials have played an important role in the development of top-down approaches by allowing the continued reduction of the minimum feature size through the development of new resist materials that work at shorter exposure wavelengths. Using block copolymers for the resist material has an advantage - it has been shown that by separating the different functional groups of a resist material onto different block segments, the dimensional stability and etch behavior of the resist can be improved [39]. To protect the resist from airborne-based contamination, silicon or fluorine containing units can be incorporated in the block copolymers [40]. This incorporation causes the low surface energy to migrate to the top surface, thereby acting as a hydrophobic coat over the top of the resist. It has been shown that the segregation of the silicon containing block to the air-resist surface increases the dimensional stability of the pattern as well as the oxygen etch resistance [41].

Vasilev and coworkers [42] have described a process based on scanning probe

lithography where the heat from the probe (sharp tip < 50 nm) of an atomic force microscope had sufficient thermal energy to cause a localized reorganization of the poly(butadiene-b-ethylene oxide) to form periodic and non-periodic hierarchial patterns on the surface.

By using these top-down methods, it becomes problematic to go lower than 100 nm in terms of production costs and fabrication times. Therefore research is being focussed on alternative approaches, as discussed in the following sections.

2.2.1.2 Bottom-up approaches

To overcome, some of the limitations of top-down methods, an alternative approach is "bottom-up" methods. These bottom-up methods build toward larger and more complex systems by starting at the molecular level and maintaining precise control over the macroscopic structure. Through molecular interactions, the concept is based on molecular self-assembly, which means independent organization of components into patterns or structures with minimal external interference. The essential features of self- assembly are well recognized in biological based systems where a relatively small set of amino acids and nucleosides are combined in many different ways to form an infinite number of structures.

Capillary forces between particles have been used to obtain aggregates of nanoparticles. If a droplet of the colloidal suspension is dried slowly on an unpatterned polar surface, the particles aggregate at the rim of the droplet because of attractive capillary forces between the particle when the water film thickness is of the dimensions of the particle diameter [43] . Positioning and adhesion in the suspension liquid are controlled by charge and polar interactions between the substrate and particle surfaces. Thus, capillary forces between the particle and the surface laterally displace the particles during drying. When an aqueous dispersion of colloidal particles is allowed to dewet from a patterned solid surface with appropriate relief structures, the

particles get trapped and assemble into aggregates whose structures are determined by the geometric confinement provided by the templates. By this method, the capability and feasibility of assembling polystyrene beads and silica colloids ($\sim$ 150 nm in diameter) into complex aggregates has been demonstrated [43].

Colloidal particles can be trapped at a liquid surface as a result of the electrostatic and surface tension forces. The interaction between the ions/macromoelcules in solution and charged Langmuir layers drives the organization at the air-water interface. The nanoparticles organized in this fashion can then be transferred onto suitable substrates by the Langmuir-Blodgett method [44, 45]. The surface of these colloidal particles are modified such that they will only be partially immersed into the surface of a liquid after they have been spread onto the air-liquid interface [46]. It is the strong interactions between the colloidal particles that lead to the spontaneous formation of a 2D aggregate at the interface.

By taking advantage of protein as well as polymer self assembly, research has been undertaken to form molecular machines from these building blocks [47, 48]. Rapaport and coworkers synthesized triple-stranded β-sheet peptides designed for an ordered 2D molecular assembly at the air - water interface [47]. Pozzo and Walker [48] used long-range crystalline order of a water soluble triblock copolymer to template proteins. A poly(oxyethylene-b-oxypropylene-b-oxyethylene) copolymer (PEO-PPO-PEO) was used to form a core-corona micelle structure with PPO being the dehydrated core and PEO the hydrated corona. The protein particles were dispersed in these concentrated block copolymer solutions which then micellized. With increasing temperature, the micelles packed into organized structures with long-range crystalline order. This served as a highly organized template for proteins and has consequently potential for organizing other nanoparticles. Biological molecules like oligonucleotides and their analogues have been used as templates, to electrostatically

encapsulate cationic-capped gold nanoparticles [49]. The concept of DNA hybridization based self-organization of molecular compounds has been applied to the assembly of a number of DNA-derivatized gold colloids [50, 51].

2.2.1.3 Combined approaches

Combining the bottom-up approach, such as block copolymer self assembly, together with the top-down approach of templating is also an attractive method to allow nanostructures to be lithographically fabricated in precise positions on a substrate. In one such study, poly(styrene-b-methyl methacrylate) block copolymer (PS-b-PMMA) of molecular weight of 104 kg/mol was used [52]. Before the block copolymer was spun coated on the substrate, which was chemically patterned using lithography to obtain a surface directed morphology by the copolymer on annealing. Figure 10 explains the process where the silicon wafer was chemically patterned with alternating hydrophilic and hydrophobic lines with periods between 45 and 55 nm using ultraviolet interferometric lithography. The block copolymer (lamellar period $\sim$ 48 nm) was then spin coated onto the treated substrate and on annealing the BCP assembly is directed by the chemical patterning on the surface and replicates it exactly.

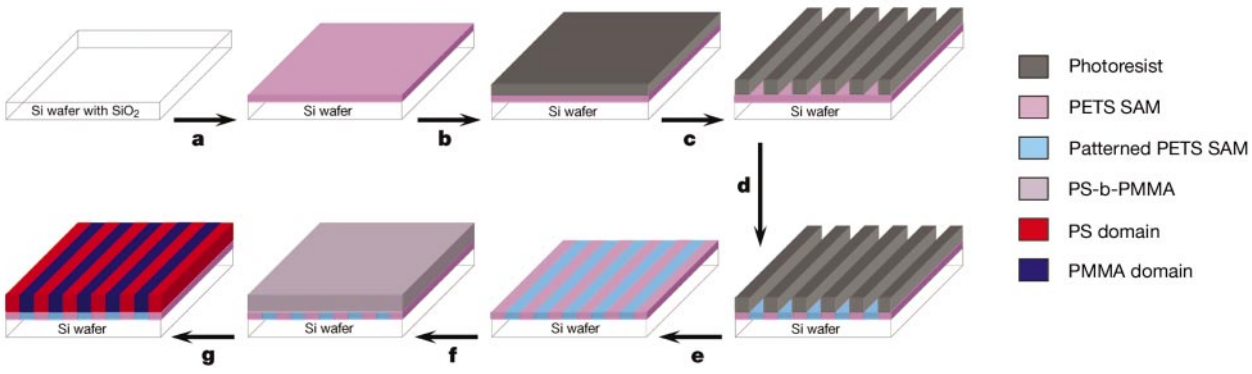

Figure 10: Step by step process of epitaxial assembly using chemically patterned substrates (Reproduced from [52]).

Sundarani and coworkers [53] reported a method for aligning poly(styrene-b-ethylene propylene) (PS-PEP) diblock films of total molecular weight 22 kg/mol,

where PS formed core of the cylinders. The films were prepared on a topographically patterned silicon nitride substrate created using electron beam lithography and reactive ion etching techniques to pattern the substrate with 35 nm deep grating lines. This patterned substrate was then used to guide and confine the self-assembly of PS cylinders along the length of the etched channels. These workers reported the alignment of cylindrical domains in the confined volume initiated by the preferential wetting of the PS layers on the vertical sidewalls of the troughs.

Ordered copolymer films have been used as a sacrificial etching mask for lithographic processes [1, 2]. The key is to have a block copolymer film with good chemical selectivity between its constituents so that one may be removed and the other can act as an etch mask to pattern an underlying film. Cheng et al. used poly(styrene-b-ferrocenyldimethylsilane) (PS-PFS) BCP to spin cast on silica substrates with grating lines made by interference lithography. The BCP self assembled structure was then used as an etching mask, to create hexagonally close packed arrays of silica pillars with 20 nm feature sizes [2]. Park et al. fabricated hexagonal arrays of holes and dots in silicon nitride by using sphere forming PS-PB monolayer as an etching mask [1]. In this case, PS-PB was spin coated on silicon nitride and then reactive ion etching (RIE) used to selective remove the PS or PB. The remaining polymer then acts as a mask to transfer the microdomain pattern to the underlying silicon nitride in order to create dots and holes respectively. Figure 11 shows the details of the process used where Fig 11(A) and (B) show the schematics of producing holes and dots respectively.

Since the etching rates of PS and PB are almost the same under RIE conditions, successful pattern transfer was ensured by introducing selective etching in the polymer to create both the holes and dots. To create holes, PB phase was degraded and removed by exposing the surface to ozone which predominantly attacks the carbon-carbon double bonds in the PB. To create dots, a selective etching rate was achieved

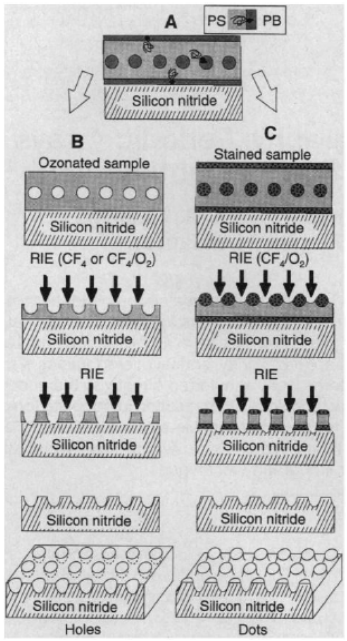

Figure 11: Schematics to produce holes and dots in silicon nitride (Reproduced from [1]).

by staining the PB phase with osmium tetraoxide. In this way, the etching rate of PB was reduced to almost half of that of PS.

In another example, Thurn-Albrecht et al. produced ultrahigh-density cobalt metal arrays using a cylinder-forming PS-PMMA BCP template [54]. The schematic illustration of the process is shown in Figure 12 where PMMA cylinders were oriented normal to the substrate by applying an electric field across the polymer film (Fig 12(A)). The PMMA was then degraded by deep UV radiation, which simultaneously cross-linked the PS. The degraded PMMA was removed by acid rinsing and the resulting pores were filled with cobalt by electrodeposition from a methanol solution.

The effectiveness of the directed assembly of block copolymers is evident from the above examples. But these approaches often need expensive lithography equipment. Also, bulk block copolymers can not be used in this approach. To get cost-effective 3D templating, bottom-up approaches need to be combined with other methods such as external fields if long-range order is to be created.

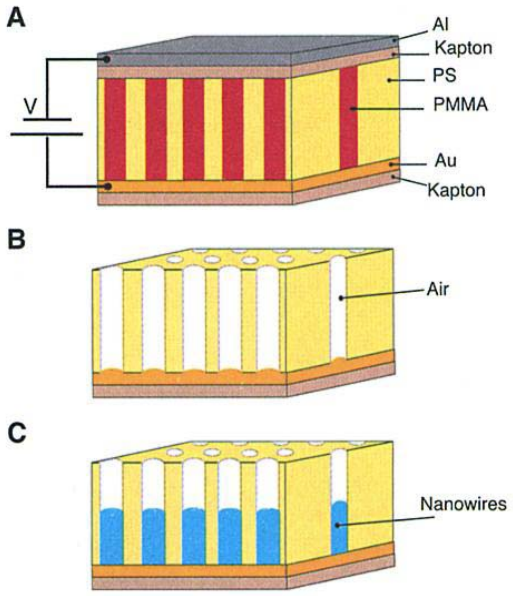

Figure 12: Schematics of high density nanowire (cobalt) production using PS-PMMA BCP film (Reproduced from [54]).

2.2.2 Block copolymer nanotemplating

Work done on block copolymers used for nanoparticle templating can be divided into three main approaches as discussed below.

2.2.2.1 In-situ approach

An in-situ approach means that the monomers needed for the BCP synthesis are preloaded with chemical moieties and precursors necessary for nanoparticle synthesis. This could be done either by directly attaching the metal to the polymer chain [55, 56] or loading the BCP monomer with metal salts so that there is formation of nanoparticles within the copolymer domains [57, 58, 59, 60, 61]. Synthesis of nanoparticles in block copolymers has the advantage of getting some degree of control over metal cluster formation.

A number of studies have demonstrated direct attachment of nanoparticles by

starting out with functionalized monomers [55, 56]. Chemical treatment of the copolymer after the synthesis converts the organometallic compound into a metallic nanocluster. The nanoparticles are located within the predetermined block copolymer domain. Iron oxide (γ-Fe_2O_3) nanoparticles with diameters of about 8 nm were incorporated in monomers of norborene based diblock copolymer precursors where ring opening metathesis polymerization (ROMP) at room temperature of this precursor mixture was used as the synthesis method to create uniformly dispersed nanoparticles in a polymer matrix [55]. Other nanoparticles like cadmium selenide, and zinc sulphide were included in the diblock copolymers using this method [56]. Even though selective segregation of nanoparticles is achieved in this case, the nanoclusters formed this way generally were found to have a broad size distribution.

An alternative approach to functionalizing monomers is the use of metal salts. To control the location of the nanoparticles, metal salts and the BCP system have to be chosen carefully. Boyen et al. used polystyrene-b-polyvinylpyridine (PS-PVP) with a $CoCl_2$ metal chloride solution [58], to take advantage of the fact that this metal salt would selectively coordinate to PVP. After oxygen etching and hydrogen plasma treatment, a short range hexagonal templating order was achieved. Similar work on PS-PVP and cobalt nanoparticles was reported using a dicobalt octacarbonyl ($Co_2(CO)_8$) complex as the metal salt for cobalt [57]. The metal salt was added to the PS-PVP solution in toluene and allowed to dry. To decompose the salt, films were heated up to 210^0C under an inert atmosphere. Tannenbaum and coworkers reported the formation of iron oxide nanoparticles with non-spherical shapes (in their case, pyramidal) in the presence of poly(vinylidene difluoride) [59]. In this case, the polymer present in the system interacted with the preferred crystallographic planes in the growing iron oxide nanoparticles, thus imposing limitations on the evolution of the cluster shape.

The kinetics of nanoparticle growth inside the polymer is still being studied but

recent work by King and coworkers on the growth of cobalt oxide nanoclusters inside PMMA suggests that the stabilization of the particles occurs after a critical size is reached [60]. This may be critical for potential technological applications, where specific size and properties are required from the nanoparticles.

Even though the in-situ methods are effective in introducing the nanoparticles in the BCPs, they have a drawback when it comes to the volume fraction of the nanoparticles in the BCP domains. These methods result in less than half of the BCP volume containing particles which may be too low a density to be an effective template to create metal dots on a surface [37].

2.2.2.2 Ex-situ approach

To get around some of the limitations of the in-situ methods, ex-situ approaches exploit the surface chemistry of the desired nanoparticles so that they favor one component of the block copolymer more than the other [62, 63, 64, 65]. In this way, once phase separation of the copolymer has occurred, the nanoparticles would be confined to one of the segregated domains. Hamdoun et al. [63] reported iron oxide (γ-Fe_2O_3) crystals of 3.5 nm diameter surface grafted with polystyrene, which were subsequently solubilized in the PS domain of a lamellar poly(styrene-b-butyl methacrylate). However, the periodicity of the copolymer's lamellar microstructure was too small to clearly resolve the metal particles within the domains. Similar work was done where gold nanoparticles were coated with polystyrene and dispersed in a PS-PEP block copolymer [62]. The gold preferentially located in the PS phase (as shown in Figure 13), where gold nanoparticles can be seen as black dots in the gray colored PS domains.

Chiu et al. synthesized gold nanoparticles in the presence of polystyrene-poly(2-vinylpyridine) diblock (PS-P2VP) copolymer [61]. The gold nanoparticles used in the study were stabilized by carrying out synthesis in 1:1 molar ratio mixtures of

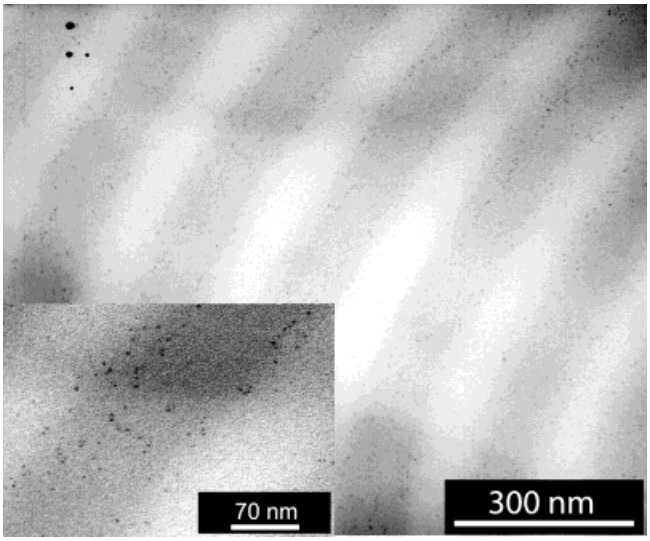

Figure 13: TEM micrograph of a cross-section of PS-PEP block copolymer with gold nanocrystals. The gray areas are PS layers and the bright regions to PEP layers. The gold nanocrystals appear as black dots in PS domains (Reproduced from [62]).

thiol terminated polystyrene (PS-SH) and thiol terminated P2VP (P2VP-SH). The equimolar ratio ensured that the nanoparticles remained at the interface of PS-P2VP copolymer.

More recently, surface modification of cadmium selenide (CdSe) nanoparticles with tri-n-octylphosphine oxide (TOPO) has been exploited [64]. These modified nanoparticles were dispersed in PS-P2VP copolymer solutions in toluene and when spun to form thin films, it was shown that these nanoparticles were selectively segregated in the P2VP phase (Figure 14). This selective segregation behavior was attributed to the balancing of the surface interactions of PS with that of P2VP with the higher surface energy P2VP covered with lower surface energy nanoparticles. Figure 14(a) shows the height and phase images from AFM measurements of the diblock copolymer without CdSe particles. CdSe self-assembly in PS-P2VP is shown in Figure 14(b), where the CdSe increased the phase contrast between the polymers.

The location of nanoparticles in the block copolymer has theoretically been shown to depend on the relative ratio of the dimensions of the nanoparticle diameter to that

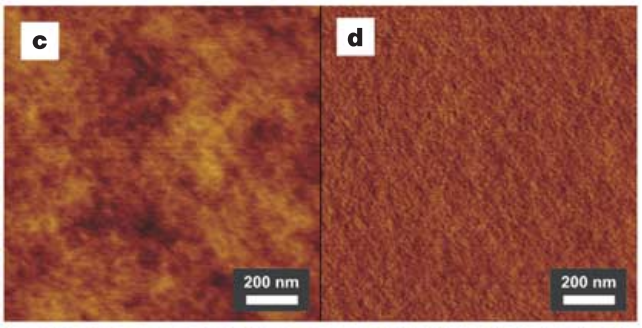

(a) height and phase image of annealed PS-P2VP film

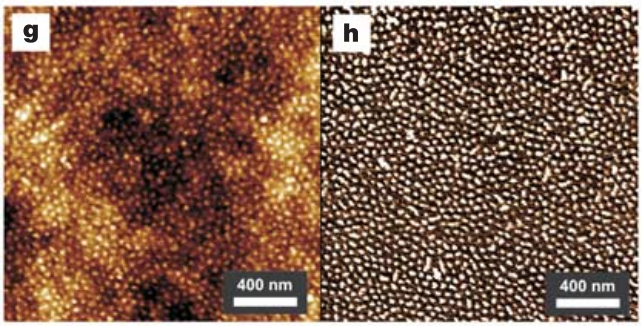

(b) Height and phase image of annealed PS-P2VP film with CdSe nanoparticles

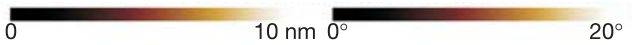

Figure 14: AFM micrographs of thin films from PS-P2VP with and without Cadmium selenide nanoparticles (Reproduced from [64]).

of the BCP domain size [66, 67]. Theoretical work was carried out for a 2-D system of lamellar diblock BCP (domain spacing = L) and spherical nanoparticles (particle diameter = d) where self consistent field theory (SCFT) was used for the BCP and density functional theory (DFT) was used for the nanoparticles. The particles were assumed to like one component of the diblock BCP. It was found that the smaller particles with a d/L ratio of about 0.2 segregate at the interface whereas for particles with a d/L ratio of 0.3 concentrate at the center of the BCP domain [66]. There is also experimental evidence of differential segregation based on particle size in the case of PS-PEP, where the gold particles ($d/L = 0.06$) were located at the interface, and silica particles ($d/L = 0.26$) in the center of PEP domains of the PS-PEP diblock system [67]. As shown in Figure 15, the gold particles appear as dark spots along the

interface and the silica nanoparticles reside in the center of the PEP domain. In a

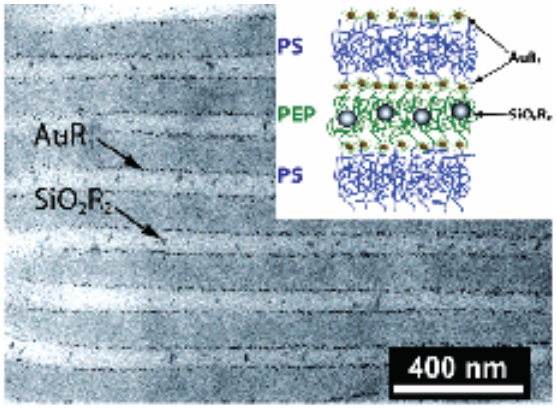

Figure 15: TEM micrograph of PS-PEP with gold and silica nanoparticle inclusions where the inset shows the schematic of particle distribution in PS-PEP (Reproduced from [67]).

related study on PS-b-PEP-b-PS with polydisperse gold nanocrystals, small particles ($d < 3$ nm) within the PS domains were found along the interface while the larger particles ($d > 5$ nm) segregated to the center of the PS domains [68]. In this case, entropic contributions play an important role in the selforganization of the different sized nanoparticles

The phase morphology of the block copolymer system can be transformed by adding selectively segregating nanoparticles but the prediction of the resulting structures is difficult, as it is dependent not only on the copolymer block length, composition and architecture, but also the particle size, volume fraction and interaction energy [69, 70]. Using self consistent field theory (SCFT) for the diblock copolymer and density functional theory (DFT) for the particles, Buxton et al. found that the introduction of monodisperse, selective particles to a lamellar copolymer swells the relevant microdomain whereas the non-selective particles reside at the interface [69]. Similar theortical work by Lee and coworkers looked at the effect of two different sized particles where a morphology transition was predicted attributed to the tuning of the particle/polymer interaction to induce a transformation [70].

In some diblock systems, the phase morphology transformation of the BCP has

been observed experimentally when the nanoparticles are incorporated [71, 72, 73]. Yeh and coworkers have reported morphology transformation from cylinders to spheres in the case of PS-PEO thin films due to hydrogen bonding between the surface hydroxylated cadmium sulfite (CdS) nanoparticles and the PEO phase [71]. The same group

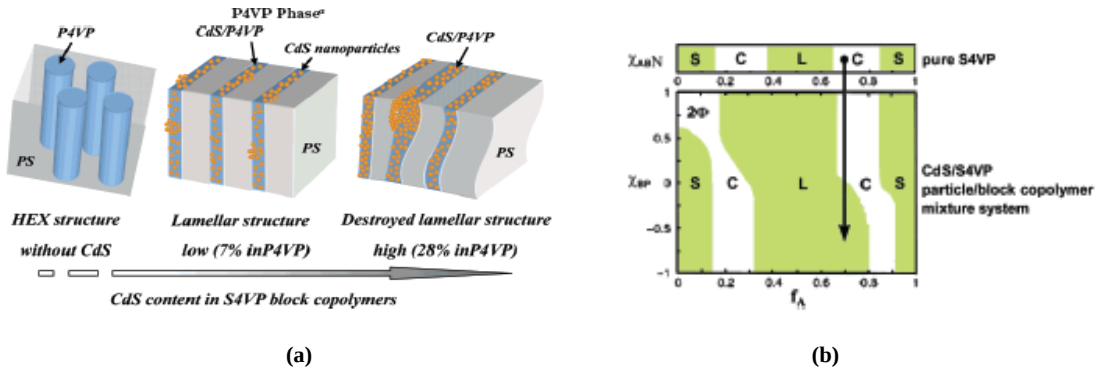

Figure 16: (a) Morphological transformation of PS-P4VP from hexagonal to lamellar structure (b) Phase diagram of the transformed system showing the reduced interaction parameter (Reproduced from [72]).

also reported a morphology change from cylinder to lamellae when CdS nanoparticles were added to the PS-P4VP block copolymer film due to the hydrogen bond formation between CdS and the minor BCP phase (P4VP) [72] as schematically shown in Figure 16. The transformation is caused by hydrogen bonding which reduces the effective interaction parameter of the block copolymer and nanoparticle mixture. In other work [73], hexagonal morphology was changed to spherical morphology by adding C_{60} fullerenes to PS-P4VP block copolymer system. In this case, the morphology change was attributed to C_{60} forming charge-transfer complexes with multiple pyridine groups from different P4VP chains.

2.2.2.3 Nanoparticle vapor deposition approach

Other than in-situ synthesis and surface modification of nanoparticles, templating can also be done by thermally evaporating metal onto a copolymer thin film and then allowing the metal to diffuse into the film. Lopes and Jaeger [74] carried out

extensive experiments of a series of metals to show that there was a differential wetting of the cylinder-forming PS-PMMA diblock copolymer by metal (gold, silver, lead, tin, indium and bismuth) so that particles diffused into one of the domains. They also found that to achieve better filling in individual domains, it was better to anneal the system after every metal layer was deposited.

Ansari et al. [75] successfully demonstrated templating of gold nanoparticles in poly(styrene-isoprene-styrene) triblock copolymer films stained with osmium tetraoxide (OsO_4). The selective staining of polyisoprene with osmium tetraoxide (OsO_4)

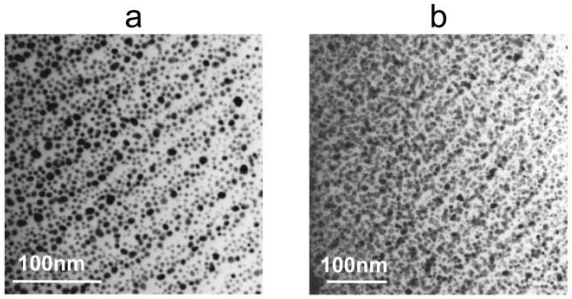

Figure 17: TEM images of of gold sputtered onto stained PS-PI-PS triblock copolymer after first coating (left) and second coating (right) of gold (Reproduced from [75]).

enabled vapor deposited and sputtered gold particles to be patterned over osmium labeled PI domains, as shown in Figure 17. The selectivity of the gold was shown to increase by staining PI with OsO_4.

Although these experiments have been tried on thin films, these can not be extended for bulk samples.

2.3 Long range ordering methods

Precise control over the orientation and ordering of microdomains is critical where a BCP is to be used as a template, for example in addressable memory applications [76]. Depending on BCP molar mass, incompatibility of block components and preparation conditions, thin films self-assemble into morphologies with a liquid-like or crystalline

order of microdomains. In the liquid-like case, the order only persists a distance which does not exceed a few repeat periods of a microdomain structure, hence being short-range. In the case with crystalline order, BCPs reveal regions called grains (or domains) which have a random orientation with respect to each other.

In-plane patterns formed by cylinder-forming BCPs demonstrate a variety of topological defects. The first type of defect is a disclination, which is recognized from either "bending" of the crystal planes or points where planes with three different orientations meet. The second type of defect is a dislocation, which corresponds to the insertion of an extra period in the crystal plane. Figure 18 shows both these types of defects.

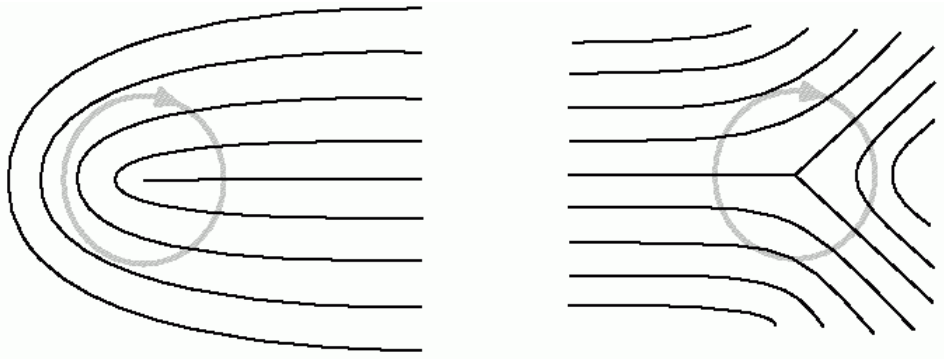

(a) Disclinations

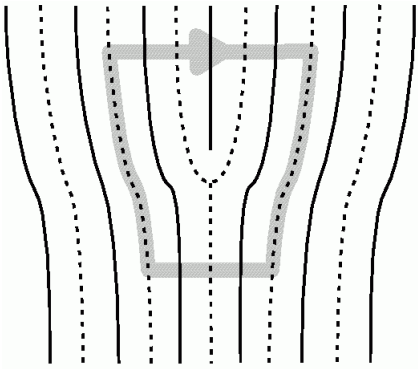

(b) Dislocation

Figure 18: Defects in the in-plane patterns formed by cylinder-forming block copolymers. (Reproduced from [77]).

In sphere and cylinder-forming systems (where cylinders orient normal to the substrate), defects occur when the number of neighbors surrounding each microdomain changes. The six-fold symmetry of the hexagonal pattern is broken at the grain boundaries where a string of microdomains are surrounded by four, five, seven or even eight close neighbors. These defects of microdomain packing lead to dislocation defects. Since the fraction of defects in the BCP directly relates to the grain size, it is usually used as a criterion of the structural order. While the grain size reflects the orientational order of the BCP structure, the distribution of the microdomain spacing is the characteristic of its translational order. The BCP structure which has only the short-range translational but quasi-long-range orientation order is called a hexatic phase [78]. In the hexatic phase, microdomains have on average 6 neighbors, i.e. each five-neighbored microdomain is always adjacent to another having seven close neighbors. This hexatic phase is also referred to as a the five-seven dislocation.

In diblock copolymer thin films, the defect spacing and the measure of the order is described by a parameter, ξ_2 which is called the orientation correlation parameter. This is defined by the distance over which the microdomain orientation is maintained. The value of ξ_2 increases as the order in the system increases and for a perfectly ordered sample, ξ_2 will be ∞. To increase the order of the film, defect annihilation, for instance by annealing, increases the grain size and a consequent reduction in defect density. For cylinder-forming systems, the main process for the reduction in defect density occurs when 3 or 4 disclination defects recombine to form the fewest number of additional defects [79, 80]. By measuring ξ_2 over a period of time, it was found that for thermal annealing, the magnitude of ξ_2 grows with time according to a power law dependence with an exponent of (1/4).

Well-ordered structures of high molecular weight can not be obtained directly by thermal annealing due to kinetic barriers that arise from chain entanglement and the thermodynamic barriers to diffusion of one block through the domains of another.

Moreover, unassisted self-assembly is not sufficient for most applications, since the nanoscale domains in the phase separated block copolymers have a typical grain size only in the sub micron range.

Combining block copolymer self-assembly with long-range ordering methods could potentially produce nanostructures which can be lithographically fabricated in precise positions on a substrate. A lot of interest in the field of block copolymers has been focused on the alignment of the microdomain patterns by various means. It was demonstrated that regular profiling and chemical patterning of the substrate allow the macroscopic crystal-like ordering of microdomains in thin films [81, 82, 83]. The required pattern periodicity is typically much larger than the spacing between adjacent microdomains and can be fabricated by methods like photolithography and microprinting.

The following sections provide a short review of some of the other methods that have shown to generate macroscopic alignment in block copolymer samples.

2.3.1 Solvent vapor annealing

One effective mechanism of achieving long-range order is the use of solvent vapor annealing - exposure of the polymer to solvent vapor for differing times - where solvent imparts mobility to the system, enabling alignment of the microdomains without any thermal treatment. In addition, the solvent can also mediate interactions between the block copolymer and reduce their surface energy differences. The mechanism of solvent annealing in thin films is driven by the non-uniform solvent evaporation and a gradient in the solvent concentration through the film thickness. As the solvent evaporates, the concentration of solvent increases from the surface to the substrate and a gradient in the solvent concentration develops normal to the surface. Consequently, the ordering front propagates normal to the surface, [84] as shown in Figure 19.

Russell and coworkers [86] have shown that solvent flow can induce alignment

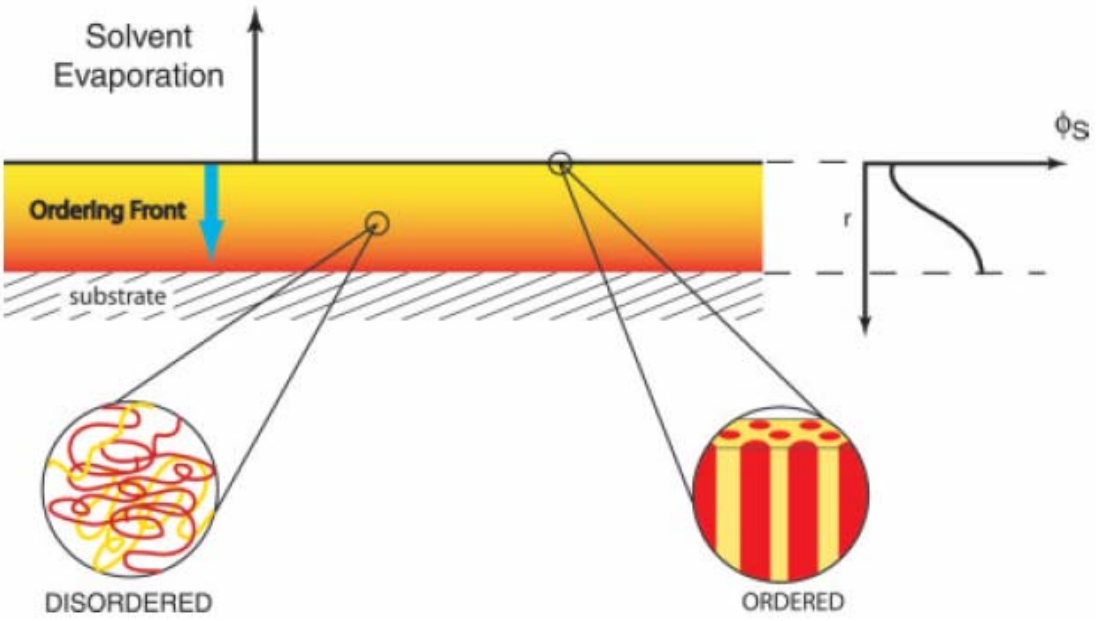

Figure 19: Schematic representation of the solvent evaporation in a block copolymer thin film - gradient in the ordering front can be seen (Reproduced from [85]).

of the butadiene cylindrical domains in poly(styrene-butadiene) BCPs. The solvent (methyl ethyl ketone) was slowly evaporated from a cylinder-forming BCP solution droplet, which was pinned on an inclined substrate. The solvent flow induced in the droplet caused the cylindrical domains to align. This technique is a good method for thicker films to achieve alignment over millimeter scales.

Knoll et al. showed that SBS block copolymer films that were solvent annealed with chloroform [87], produced morphologies that were kinetically trapped after the solvent was rapidly removed. A phase diagram was constructed for their specific system by plotting the observed phases as a function of the film thickness and polymer concentration in the films. Lodge and coworkers derived the phase diagram of PS-PI copolymer thin film when annealed in PS selective solvents (di-n-butyl phthalate, diethyl phthalate and dimethyl phthalate) [88]. It was shown that the selective solvent affects the interfacial curvature, but that this selectivity decreases as the temperature increases.

The rate of solvent evaporation has an effect on the orientation of the copolymer domains with rapid solvent evaporation shown to produce a vertical orientation and a slower evaporation yielding a parallel orientation [89, 90]. Kim and Libera reported vertically aligned cylinders of PS in a PB matrix at an evaporation rate of 5 nL/s solvent (toluene) evaporation rate and in-plane PS cylinders for the same system at 0.2 nL/s. Similar findings of perpendicular alignment at high evaporation rate and in-plane for slow evaporation rate were reported for a different system poly(styrene-b-2vinylpyridine-b-tert-butylmethacrylate) solution in tetrahydrofuran [89]. It has also been shown that carefully controlled solvent selectivity and rate of evaporation can lead to the formation of kinetically trapped transient inverted phases where the minority component forms the continuum phase [91, 92]. The other factor that determines the orientation of the microdomains is the commensurability of the film thickness [93]. For cylinder-forming poly(isoprene-b-lactide) (PI-PLA) diblock copolymer when annealed in chloroform, it was found that the PLA cylinders oriented perpendicular to the film surface when the film thickness was incommensurate with the total film thickness.

To control the characteristic length scales in the block copolymer structure, co-solvents having specific copolymer component solubilities can be used. In a PS-PEO system, the co-solvent used was water which is highly selective for PEO. Due to the retention of water in the PEO domains, the size and center-to-center distance of the cylindrical PEO domains were controlled [85]. The ordering behavior in terms of defect reduction was plotted as a function of annealing time as shown in Figure 20. From the AFM micrographs, the effect of annealing a spin coated PS-PEO film in benzene vapors for 48 hours can be seen. A triangulation routine (using a software developed at Princeton University [94]) was used to connect the centers of adjacent cylindrical domains as shown in Figure 20(C) where a blue color indicates six neighbors for each domain and a red color means five nearest neighbors and thus, a defect.

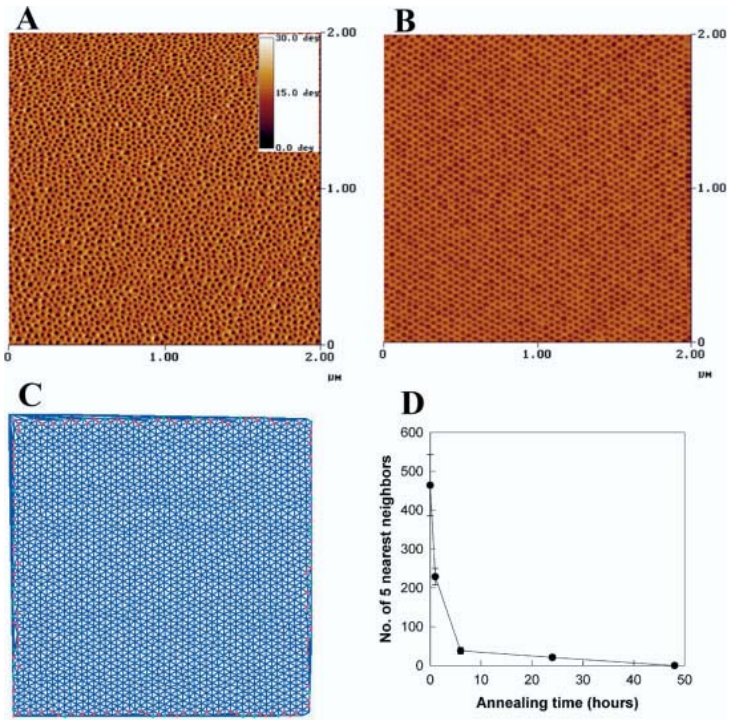

Figure 20: AFM images (2μ x 2μ) of 255 nm PS-PEO film - (A) spin coated film, (B) after annealing in benzene vapor for 48 hours, (C) triangular image of the image in (B) and, (D) the number of five-neighbor defects as a function of solvent annealing time (Reproduced from [85]).

As the annealing time increased (shown in Figure 20(D)), the annihilation of defects occurred rapidly for the first few hours and then slowed down and after about 50 hours of annealing all the defects were removed.

To enhance the propagation of the orientation of the microdomains normal to the surface over large distances, a small amount of homopolymer PEO has been added to the core of cylindrical microdomains of PS-PEO BCP [95]. Removing this homopolymer from the block copolymer creates a nanoporous template with arrays of long-range order.

2.3.2 Shear field

One of the first flow-induced alignment results were reported in PS-PB-PS (Kraton) triblock copolymer by Keller and coworkers [96]. They used melt extrusion on the

microphase separated PS-PB-PS, when the molten material was squeezed through the die into a heated glass capillary, the shear gradient developed resulted in axially well ordered cylindrical domains. Hadziioannou et al. [97] subsequently reported alignment of cylindrical as well as lamellar domains of PS-PI diblock copolymers by reciprocating shear techniques using parallel plates with an adjustable gap. Reciprocating shear was used by Almdal et al., a spherical phase (bcc) forming diblock of poly(ethylene-propylene)-b-poly(ethylethylene) (PEP-PEE) was studied, and shear resulted in producing twinned crystals of bcc spherical domains of PEE [98].

The mechanism of shear alignment in diblock copolymers has been studied theoretically [99, 100] and experimentally [101, 102, 98] by a number of groups. They suggest that shear ordering is achieved by suppressing the disordering fluctuations in the copolymer concentrations. The degree of alignment achieved by shear depends on many factors like shearing rate and polymer composition etc. Of these factors controlling the degree of alignment, the most important is shear rate. Balsara et. al [103] reported that shear could not only lead to ordering but also disordering depending on which shear rate was chosen. They explained that in a cylinder-forming poly(styrene-isoprene) diblock copolymer, increasing the shear rate from $0.004s^{-1}$ - $0.1s^{-1}$, increased the order of the system. However, in the higher shear rate range of $0.1s^{-1}$ - $10s^{-1}$, increasing the shear rate led to more disorder in the sample. It was suggested that these high shear rates ($0.1s^{-1}$ - $10s^{-1}$) were greater than the inverse relaxation time of cylinder fluctuations and that the cylinders were not quick enough to respond to the shear rate. Alignment of cylinders and spherical BCP (PS-PEP) domains have been reported by using a soft PDMS mask as a one of the surfaces, the other being a silicon wafer onto which the BCP film was spun coated [104, 105]. The degree of order in a model hexagonal phase BCP was studied theoretically using cell dynamics simulations and it was found that the orientational correlation length grew with time according to a power law with an exponent of (1/4) [79, 106].

In addition to aligning the domains, shear can also change the morphology of the microdomains [107]. This was reported by Park and coworkers where application of shear on poly(styrene-b-(ethylene-propylene)-b-ethylene) triblock copolymer changed the morphology from spherical microdomains into the cylindrical phase [107]. This was achieved by roll casting where BCP solution in decalin was poured onto heated counter rotating cylinders while at the same time the solvent was allowed to evaporate.

Large amplitude oscillatory shear (LAOS) has been applied to both diblock and triblock copolymers [108, 109, 110]. PS-PI diblock copolymer, it was found that the lamellae could align parallel or perpendicular to the shear gradient direction depending on the frequency and temperature applied to the system [109]. On the other hand, for PS-PI-PS, only perpendicular alignment of the lamellae was achieved as the middle block formed bridges and hindered the sliding motion [108]. Stangler et. al also reported better LAOS aligment in the case of diblock (PS-PI) rather than triblock copolymers (PS-PI-PMMA) because of sliding mechanism suppression [110].

2.3.3 Electric field alignment

Electric fields can be used to align a BCP system by taking advantage of the dielectric constant difference between the components of the system. Amundson et al. [111, 112, 113] demonstrated the alignment of lamellar PS-PMMA diblock copolymers using an in-plane electric field of 20 kV/cm. The domains oriented themselves normal to the direction of the applied field. Similar experiments with electric fields up to 35 kV/cm were performed on cylinder-forming PS-PMMA diblock copolymer thin films to achieve micrometer-length scale alignment of the cylinders parallel to the direction of the field [114]. Examples of cylinders oriented normal to the substrate by using electrodes normal to the substrate have been reported [54, 115]. It was also found that a threshold electric field strength existed above which complete orientation of the cylindrical domains was achieved. At field strengths slightly below this value there

was a coexistence of the parallel and perpendicular domains [116].

Electric fields have not been limited to alignment in BCP thin films but have also achieved long-range order for thicker samples (few microns) in the melt [117]. 30 μm thick films were oriented using a strong electric field of 20 kV/μm when annealed above their glass transition temperatures, with in-plane alignment extending laterally over hundreds of microns [117]. The use of BCP melts for electric alignment has been restricted to low molecular weights because of the higher melt viscosities of the polymers, and a need for high temperatures, which are close to the decomposition temperatures. A better approach for high molecular weight BCP polymers may be using electric field in solution rather than melts. This approach has been investigated by Böker and coworkers where a lamellar morphology of a high molecular weight (M_n 82,000 g/mol) poly(styrene-b-(2-hydoxyethyl methacrylate)-b-methyl methacrylate) was aligned preferentially in the field direction [118]. The field strength of 1.8 kV/mm was applied during solvent evaporation until a solid film was formed.

2.3.4 Magnetic field alignment

With respect to BCP-nanoparticle composites, the magnetic properties of the nanoparticles could present the basis of attaining long-range order in the system by a magnetic field. Under the influence of a magnetic field, the alignment of magnetic nanoparticles could allow some control over the alignment of the BCP domain they reside in. Work on magnetic alignment that demonstrates the principle has been undertaken on aligning micron sized iron particles (1-3 μ diameter) in a polyimide film [119]. A magnetic field of around 400 Gauss was used to align the iron particles when annealed for 6 hours at 180^{o}C. The resultant film showed iron particles arranged in columns in the direction of the magnetic field. Casavant et al. have studied the alignment of surfactant suspended single wall carbon nanotubes (SWNT) by using a magnetic field [120]. They were able to produce a highly ordered thin film ribbon made of carbon

nanotubes by magnetic alignment.

There has been some work on magnetically aligning liquid crystalline (LC) diblock copolymer of poly(styrene-b-isoprene) where LC mesogens were attached to the isoprene block [121]. A magnetic flux of about 9 Tesla was applied at elevated temperatures to achieve alignment of non-LC PS cylinders in the LC matrix of isoprene. This approach is interesting as the orientation of the LC phase helps in the alignment of the microphase structure [122]. Thus, magnetic nanoparticles and LC phases in BCPs can serve as the driving force for the BCP itself.

2.3.5 Thermal gradients

Thermal gradients in combination with the surface effects have been investigated in bulk samples of lamella forming PS-PI block copolymers [123, 124]. The sample was placed in a teflon cell and was enclosed by a PS-coated glass plate at one end. A temperature gradient of 70^0C was moved normal to the glass plate at 25 nm/s [123]. The ordering of the microdomains was observed normal to the glass substrate and parallel to the temperature gradient that extended through the material. It was hypothesized that the lamellae orient parallel to the temperature gradient when the temperature differences dominate over the surface energy effects [124]. This happened at distances further from the glass plate. The lamellae were oriented perpendicular when the surface energy effects dominated at distances closer to the glass-sample interface.

De Rosa et al. have also investigated the thermal effects on the alignment of the block copolymers [125, 126]. A crystallizable block copolymer was dissolved in a crystallizable solvent and allowed to cool from above their combined melting point. It was shown that the rapid solidification of the system caused trapping of the kinetically formed microdomain structure of the copolymer. Using this method, cylinder-forming PS-PEP where PE is the crystallizable block component was ordered using benzoic

acid as the solvent.

CHAPTER III

MATERIALS, METHODS AND TECHNIQUES

There are two main sections in this chapter, firstly, block copolymer nanoparticle composite studies and secondly, long-range order (solvent annealing) studies. The materials, methods and the characterization tools used for each of these are explained in separate sections.

3.1 Block copolymer-nanoparticle composite studies

3.1.1 Materials

All the polymers used in this thesis were purchased from Polymer source, Inc. (Canada) where these polymers were synthesized using living anionic polymerization where the blocks were added sequentially. Different triblock and diblock copolymer systems have been chosen for this study as described in Table 1 where S stands for polystyrene and B for polybutadiene (see Figure 21).

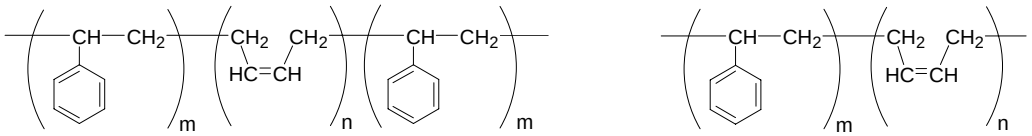

(a) SBS (b) SB

Figure 21: Chemical structure of the block copolymers used.

SBS-I and SBS-II were chosen because they vary in configuration and molecular weight but have the same PS volume fraction. SB-II was chosen to compare directly with SB-I but had twice the molecular weight and the volume fraction almost half.

This diverse selection of these block copolymers was made in order to allow better understanding of how different sized nanoparticle inclusions influence the behavior of different molecular weight diblock and triblock copolymers.

Gold (Au) nanoparticles (5 nm diameter) were purchased as aqueous solutions from Tedpella, Inc with a concentration of 5.0 x 10^{13} particles/ml. These solutions have a characteristic pink-red color associated with the scattering of light from the nanoparticles. Buckminsterfullerene (C_{60}) (98% pure) was obtained from Aldrich. Both the gold solutions and C_{60} were used without further purification. Toluene (>99.8%, Fisher Scientific) was used as a film casting solvent. Methanol (ACS certified, Fisher Scientific) was used as a non-solvent in the BCP-nanoparticle dispersion process. 1-dodecanethiol (98%, Fisher Scientific) was used as a surfactant to disperse aqueous gold nanoparticles in the organic medium [63]. The methanol, toluene and 1-dodecanethiol solvents were used as supplied without further purification.

3.1.2 Sample Preparation Methods

3.1.2.1 Pure copolymers

Bulk samples (2 - 3 mm thick) of all the pure copolymers were prepared from 3% (w/v) polymer solutions in toluene. To make these solutions, 150 mg of polymer was dissolved in 5 ml of toluene. To ensure complete dissolution, the solutions were sonicated using a FS20, Fisher Scientific sonicator for one hour at room temperature and then checked to ensure that there was no residual solid (polymer) visible in the solution. These polymer solutions in toluene were then poured into silicone rubber molds (Pelco 110 flat embedding mold, Tedpella, Inc.) and dried at room temperature over a period of a week. These samples were subsequently dried at reduced pressure

Table 1: Characteristics of the different triblock and diblock copolymers used in these studies

Notation	Total Mol. weight (M_n in kg/mol)	Mol. weight of components (M_n in kg/mol)	PDI	PS weight (%)	PS volume (%)
SBS-I	108	39 - 30 - 39	1.15	72.2	67.7
SBS-II	54	19.5 - 15 - 19	1.15	72.2	67.7
SB-I	31.9	22.8 - 9.1	1.04	71.5	66.9
SB-II	70	61 - 9	1.06	87.1	84.9

of 10^{-5} mbar in a vacuum oven for two days at 80^0C.

3.1.2.2 BCP with gold nanoparticle (Au) inclusions

To add gold nanoparticles to the polymer solutions, the nanoparticles had to be transferred from the supplied aqueous phase to the organic phase (in our case, toluene). In order to achieve this, the gold nanoparticles were dispersed in toluene by surface stabilization and then added to the 3% (w/v) polymer solution in toluene using the following method. One ml of aqueous solution of Au was vigorously stirred at 1120 rpm at room temperature. To this, 0.5 ml of 50% (v/v) solution of 1-dodecanethiol in toluene was added drop wise to the stirring gold solution. After all the 1-dodecanethiol solution was added, the mixture was stirred at the same speed for a further 20 minutes. At this point, 1 ml of methanol (non-solvent) was added and the resultant mixture was continued to be stirred for another 15 minutes. The solution was left to stand for 5 minutes after which the reddish-pink color (characteristic of gold) was visible only in the toluene phase. This less dense top organic layer containing gold nanoparticles was carefully pipetted off. The required amount of this gold dispersion in toluene was then added to the polymer solution to make 0.1 - 5% (w/w) gold in polymer solutions. Bulk samples were then made using the same solution conditions as specified in Section 3.1.2.1.

To ensure that there was both complete transfer of gold to toluene and also that there was no agglomeration of gold nanoparticles in the toluene caused by the transfer process, UV spectroscopy measurements were performed on the gold aqueous solution before and after the transfer using a Shimadzu UV-1601 UV-Visible Spectrophotometer in the wavelength range of 400 - 650 nm. The scan started at the longest wavelength and proceeded to the shortest wavelengths.

Figure 22(a) shows the UV spectrum of the gold aqueous solution with a distinct peak at 517 nm characteristic of the dispersed gold nanoparticles. After the transfer,

the loss of the peak at 517 nm indicates that there is no significant amount of gold left in the aqueous phase. However, it was not clear if all the gold was transferred or the amount of gold left in the aqueous phase was too small to be picked up in the UV-measurements.

To answer this question, a series of measurements were performed to find out the minimum amount of gold that could be detected in the UV measurements. To accomplish this, 0.5 ml gold aqueous solution was measured using the UV spectrophotometer and was labeled as a 100% sample. Using 0.5 ml as a control (100%) sample, different dilutions were made by adding deionized water down to a concentration of 0.001%. All these solutions were then measured using the UV spectrophotometer, the results of which are shown in Figure 22(b), where it can be seen that the intensity of the characteristic peak at 517 nm decreases as the dilution of gold increases. The peak intensity continues to decrease and at 0.001%, is only just visible. Comparing these data with the aqueous solution after the transfer process, where no peak was visible in the remaining solution (see Figure 22(a)), it can be estimated that at least 99.99% of the gold nanoparticles must be getting transferred to the toluene phase.

The thiol stabilized gold nanoparticles were successfully dispersed in toluene at all concentrations. However the same is not true when mixed with the copolymers. At concentrations of 0.1-3% (w/w) solution in the BCP, the gold remained fully dispersed after removing the solvent. However, gold nanoparticles could not be dispersed at a concentration of 5% (w/w) in the copolymer, gold aggregates were formed during evaporation of the casting solution. The value of 5% (w/w) therefore appears to be the solubility limit of gold in the polymer.

3.1.2.3 BCP with fullerene (C_{60}) inclusions

To make the BCP-fullerene (BCP-C_{60}) nanocomposites, the polymer and C_{60} were independently dispersed in toluene. For the polymer, 3% (w/v) solutions in toluene

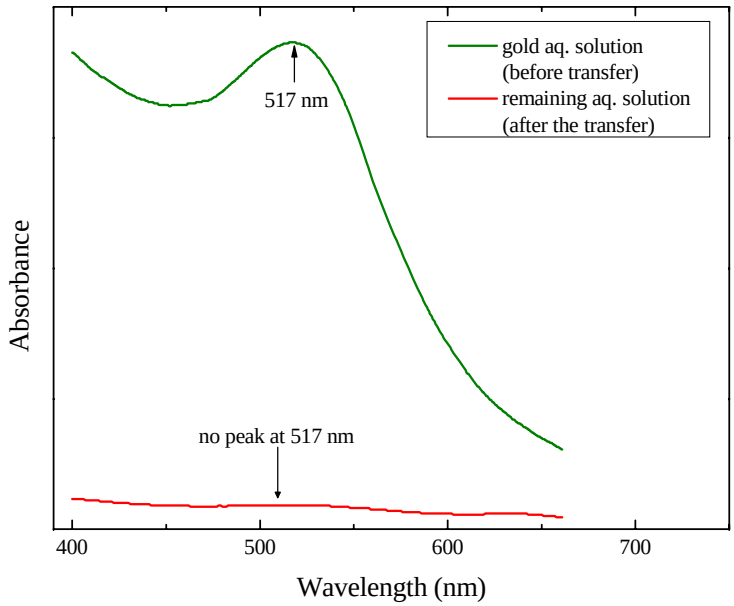

(a) UV-vis data from gold aqueous solution before and after the transfer to toluene

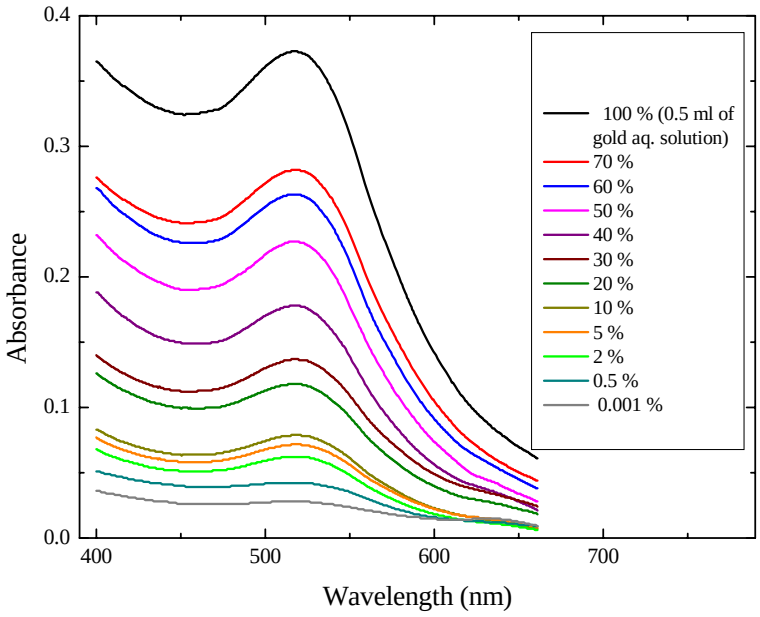

(b) UV-vis data from series for gold aqueous solution (increasing in dilution)

Figure 22: UV-vis data from gold nanoparticles - (a)UV-vis data from the gold aqueous solution before and after the transfer to the organic phase (measurement was performed on the remaining aqueous solution after the transfer and, (b) Dilution series for gold aqueous solution to find out the lowest amount of gold needed for UV signal at 517 nm

were prepared. A master batch of C_{60} was dispersed in toluene (0.01 g C_{60} in 6 ml toluene[1]) by sonicating (using Fisher Scientific FS20 sonicator) until no precipitates were seen which took approximately 2 hours. A brilliant purple color was observed for the C_{60} solutions in toluene indicating a complete dispersion. The polymer solution was stirred at room temperature at 1100 rpm (using Corning hot plate stirrer) and the appropriate amount of C_{60} dispersion was added slowly to make up the required concentration solutions in the range 0.1 - 5% (w/v) C_{60} in the block copolymer. Stirring of the mixture was continued at 1100 rpm for another 15 minutes. The resultant BCP-C_{60} solution was then added dropwise to a rapidly stirred (at 1100 rpm) excess of methanol (1 liter for every 10 ml of BCP-C_{60} solution). Since methanol is a non-solvent for the system, the resulting BCP-C_{60} precipitated and it was then filtered off under suction aspirator pump using a 0.45μ nylon filter membrane (from Whatman, Inc.). The solid was then dried overnight in a vacuum oven at 45^0C, and then further dried at a reduced pressure of 10^{-5} mbar in a vacuum oven for two days at 80^0C.

3.1.3 Characterization techniques

3.1.3.1 Small angle X-ray scattering

Small angle X-ray scattering (SAXS) is a powerful tool which can be used to identify morphology of phase separated domains in BCPs. The wavelength of X-rays is on the order of $1\mathring{A}$ making X-rays an ideal method to probe structures like microphase separated block copolymer systems. Figure 23 shows a general layout and the scattering diagram for the SAXS experiments, where the incident, $\vec{k_i}$, and scattering vectors $\vec{k_s}$ as well as the momentum transfer $\vec{Q}$ are defined.

As can be seen the momentum transfer is defined by the vector product $\vec{Q} = \vec{k_i} \cdot \vec{k_s}$, where the magnitude of $\vec{Q}$ is given by $Q = (4\pi/\lambda)\ \sin\theta$, where θ is the scattering angle

[1]The solubility limit of C_{60} in toluene is 2.8 mg/ml [127]; we have kept our dispersion below the limit at 1.67 mg/ml.

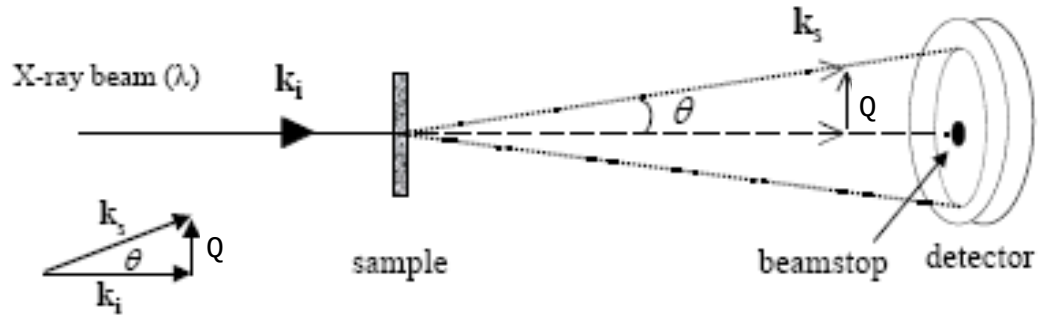

Figure 23: Schematic layout of a SAXS experimental set-up showing the incident, scattered and transmitted beams relative to the sample and the detector (Reproduced from [128]).

and λ is the X-ray wavelength. This scattering vector $\vec{Q}$ is related to the interdomain spacing (d) via the relationship - Q = $(2\pi/\mathrm{d})$.

Multiple orders of Bragg reflection can be observed for strongly segregated ordered samples. For a specific morphology, multiple order peaks occur in a sequence as a function of momentum transfer that can be depicted in terms of a shape dependent structure factor. The expected peaks for various structures are listed in Table 2 and Figure 24 is an example of SAXS data showing the peaks corresponding to different phase morphologies exhibited by poly(oxyethylene-b-oxybutylene) diblock copolymers of varying PEO content [129].

Table 2: Peak position of Bragg reflections for various BCP equilibrium structures

Structure	Ratio Q/Q^*
Lamellar	1, 2, 3, 4, 5, 6,....
Hexagonal	1, $\sqrt{3}$, $\sqrt{4}$, $\sqrt{7}$, $\sqrt{9}$, $\sqrt{12}$,....
BCC	1, $\sqrt{2}$, $\sqrt{3}$, $\sqrt{4}$, $\sqrt{5}$, $\sqrt{6}$,....
FCC	1, $\sqrt{4/3}$, $\sqrt{8/3}$, $\sqrt{11/3}$, $\sqrt{12/3}$, $\sqrt{16/3}$,....
Gyroid	1, $\sqrt{4/3}$, $\sqrt{7/3}$, $\sqrt{8/3}$, $\sqrt{10/3}$, $\sqrt{11/3}$,....

In our case, for SBS-I with and without nanoparticles (gold and C_{60}), 2D-SAXS measurements were performed using a BrukerAXS NanoSTAR using a CuKα source operated at 40 kV, 35 mA. The measurements were all taken in transmission geometry using a pinhole incident beam collimation system. The thickness of the samples

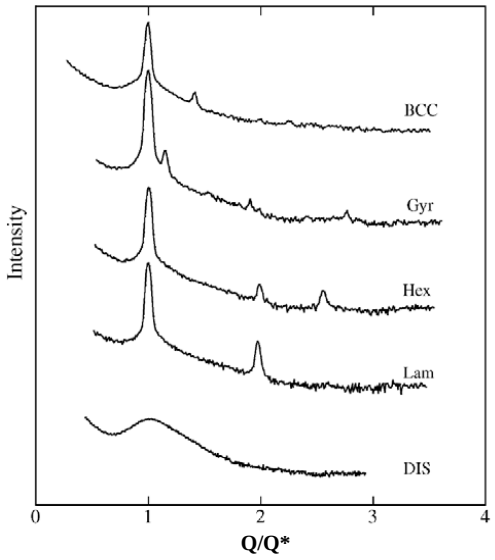

Figure 24: SAXS patterns observed for equilibrium structures formed in diblock copolymer melts of PEO-PBO(Reproduced from [129]).

were difficult to measure, so all data were plotted on a relative intensity (I) scale against the momentum transfer, Q. For all other samples, SAXS measurements were performed at station D1 of the Cornell High Energy Synchrotron source (CHESS). The monochromatic X-ray source operating at 10 keV gave a wavelength of 1.23 Å. The beam was apertured to 0.5 mm in both the vertical and horizontal directions. With a sample-to-detector distance of 1830 mm (determined via calibration against silver behenate - $CH_3(CH_2)_{20}COOAg$), SAXS data were collected using a Medoptics CCD detector with 47.2 μm pixel resolution. The scattering data was analyzed using Fit2d software (freeware from Andy Hammersley, European Synchrotron Radiation Facility, France [130]). All the data were corrected for background scattering and the Q values for the instrument were calibrated by using a silver behenate calibration. The 2D scattering data of the silver behenate standard is shown in Figure 25.

Silver behenate is known to have a strong primary peak at a d-spacing of 58.38 $\mathring{A}$ which corresponds to a scattering vector value, Q of 1.076 nm^{-1} [131]. From the raw scattering data of the silver behenate, the exact sample-to-detector distance was determined. In our case, as previously mentioned, the sample-to-detector distance

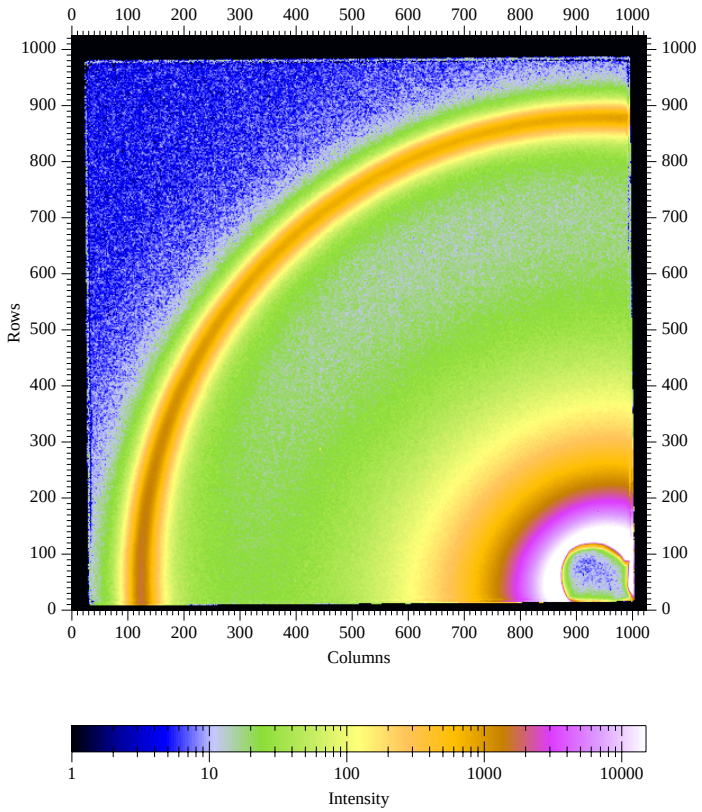

Figure 25: 2D scattering data of silver behenate used for calibrating SAXS data. The beam stop is clearly seen in the bottom right corner of the detector with beam center at pixel coordinates of (945, 50). The characteristic scattering from the silver behenate forms the arc of radius 820 pixels from the beam center. Since the scattering is well defined to occur at a Q = 1.076 nm^{-1}, the SAXS instrument can be calibrated.

value was found to be 1830 mm.

3.1.3.2 Transmission Electron Microscopy

Transmission electron microscope (TEM) makes use of high voltage electron beams generated by thermionic or field emission that are focused by magnetic lenses on to the sample [132]. They are then magnified by a series of magnetic lenses until they hit a photographic plate or light sensitive sensors producing an "electron micrograph". The image is produced by detecting electrons that are transmitted through the sample. Figure 26 shows the general schematics of a TEM.

For our experiments, bulk samples were microtomed using a cryo RMC Powertome

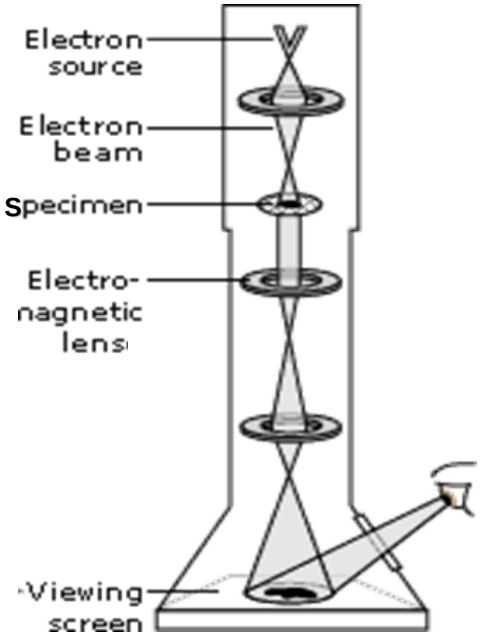

Figure 26: General schematic of TEM (Reproduced from [133]).

X and a Diatome diamond knife to yield sections of about 60 - 100 nm in thickness. These sections were then stained in a sealed vessel by the vapors of a 2% aqueous solution of osmium tetraoxide (OsO_4) overnight. Bright-field TEM was performed on a Hitachi H7600T transmission electron microscope operating at an accelerating voltage of 120 kV. To observe individual nanoparticles in the BCP, high magnification imaging was undertaken using Hitachi TEM-9500 at 200kV.

3.1.3.3 Differential scanning calorimetry

Differential scanning calorimetry (DSC) was performed on a SEIKO 220C instrument under a nitrogen atmosphere using 10-15 mg of sample in the standard aluminium DSC pans. Calibrations for the power and the temperature scales of the calorimeter were done using enthalpy of fusion and melting temperatures of pure indium and tin. The baseline correction for all spectra was made by subtracting the spectrum obtained from an empty aluminium pan measured under the same conditions. Each sample was rapidly cooled to -150^{0}C, heated to 200^{0}C (first heating cycle) and then held at 200^{0}C

for 10 minutes. This was followed by a slow cooling process down to -150^{0}C, held for 5 minutes and the sample was heated again (second heating cycle) to 200^{0}C. A heating and cooling rate of 10^{0}C/min was maintained for all the experiments except the initial cooling. All the thermograms discussed were obtained from the second heating cycle.

3.1.3.4 NMR experiments

All the NMR measurements were carried out by J. Leisen at the Georgia Tech NMR facility on a Bruker DSX-400 spectrometer (Bruker-Biospin, Rheinstetten/Germany) operated at a proton frequency of 400 MHz (at a magnetic field of 9.4 T). ^{1}H spin diffusion experiments and 2D exchange spectroscopy were carried out on 1% (w/w) gold in SBS-I samples. The details of these experiments are provided elsewhere [134]. However a brief outline of the technique is provided here. For spin diffusion experiments, all the protons in the sample are excited. The proton magnetization from the rigid phase (in our case PS) is then dephased. A mixing time is then allowed which leads to a diffusion of spin magnetization from the mobile to the rigid components. The spin diffusion process was then observed to yield information about the distances between different phases since the nanoparticle inclusions will behave differently depending on their surroundings (either PS or PB or both) [135]. It is then possible to determine the phase (or phases) in which the nanoparticle inclusion resides.

3.2 Long range order - Solvent annealing studies

3.2.1 Materials

Polymer : The polymer used in the solvent annealing studies was the SBS-I triblock copolymer, the details of which are provided in Table 1.

Substrates: Mica (25 x 25 mm pieces) obtained from Electron Microscopy Sciences (USA), was used as the substrate after it was freshly cleaved. In addition, silicon (Si) wafers (cut in (100) direction, from Novawafers, Inc.) cut in to 25 x 25

mm pieces were also used. These Si wafers were treated for 2 hours using a piranha solution consisting of a mixture of H_2O_2 (30 %) and H_2SO_4 (70%) (v/v) heated to 80^0C for 2 hours. The wafers were then rinsed with distilled water and dried in a stream of nitrogen gas. This treatment produced a native oxide layer of about 1.6 nm on the wafer surface.

A VCA-Optima XE system (AST Products, Inc.) was used to measure the contact angles of both the mica and silicon wafers. The measurements were performed by placing a 5 μL droplet of water on the substrate and measuring the profile using the digital camera attached to the instrument. To obtain a statistically meaningful result, an average value from 10 droplets was used in determining the contact angles. The contact angles for mica were found to be 8±2° (surface energy = 375 mJ/m^2 [136]) and for the piranha treated Si wafers, the contact angle was 20±3° with the calculated surface energy of 68 mJ/m^2 [137]. The contact angle images obtained for both these substrates are shown in Figure 27. The surface energy values for this

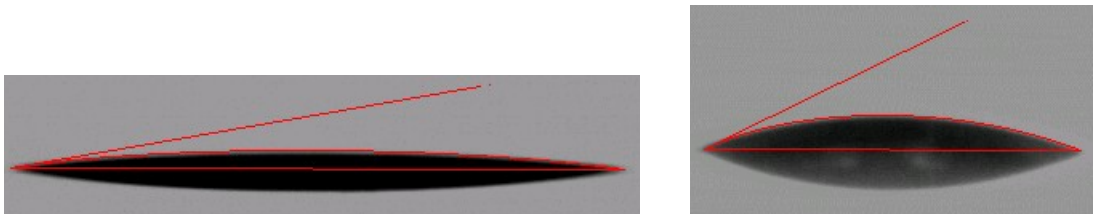

(a) Mica - 8±2°

(b) Silicon wafer (piranha-treated - 20±3°

Figure 27: Contact angle images for mica and silicon wafer substrates

treated silicon wafer is in agreement with the reported literature values [138]. The mean surface roughness determined by contact mode AFM for mica was measured to be 0.37±0.19 nm and for silicon wafer, equal to 0.24±0.1 nm.

Solvents: All solvents used in this study were purchased from Fisher Scientific. Toluene (>99.8%), cyclohexanone (≥98%) and chloroform (≥99.8%) were used as spin casting solvents for the films. The solvents used for annealing studies were:

toluene, chloroform, cyclohexanone, 1,2-dimethoxyethane (≥99%) (DME), ethyl acetate (≥99.9%) (EAC), diethyl phthalate (Lab grade), heptane (≥96%) and cyclohexanol. The solvent properties [139, 140] are summarized in Table 3.

Table 3: Properties of the solvents used for solvent annealing studies

Solvent	Formula	δ_S $(MPa)^{1/2}$	B.P. (^{0}C)	Vapor pressure (mm Hg @ 20^0)	Vapor density (air = 1)
Toluene	C_6H_5-CH_3	18.2	110.6	22	3.2
Dimethoxyethane (DME)	$CH_3O(C_2H_4)OCH_3$	15.6	85	48	3.1
Ethyl acetate (EAC)	$CH_3COOC_2H_5$	18.9	77	76	3
Cyclohexanone	$C_6H_{10}O$	20.23	156	2	3.4
Chloroform	$CHCl_3$	18.84	61	159	4.1
Diethylphthalate	$C_6H_4(CO_2C_2H_5)_2$	20.5	298	1	7.6
Cyclohexanol	$C_6H_{11}OH$	22.5	160	0.98	3.5
Heptane	C_7H_{16}	15.3	98	40	3.5

Out of the solvents listed in Table 3, grazing incidence small angle X-ray scattering (GISAXS) was performed on films annealed by toluene, cyclohexanone, DME and EAC. Toluene and cyclohexanone are relatively good solvents for both PB and PS [141]. However, DME is a selective solvent for polybutadiene (PB) [141], and EAC is a selective solvent for polystyrene (PS) [142].

3.2.2 Methods - thin film formation and solvent annealing

Polymer solutions of 1 and 4 %(w/v) were prepared in toluene. The resultant solutions were spun cast on to freshly cleaved mica (for AFM studies) or piranha-treated silicon wafers (for GISAXS) using a spin speed of 2500 rpm for 30 seconds to give 50±1 nm from 1% solutions and 260±1 nm from 4% solutions. The thickness of the films was measured using a VASE ellipsometer (J.A. Woollam Co., Inc.) after air drying at room temperature for 7 days.

These spun cast films were then exposed to saturated solvent vapors in a sealed glass chamber at room temperature for different lengths of time using the set-up

shown schematically in Figure 28. After the desired annealing time, the samples were removed from the chamber and dried at room temperature.

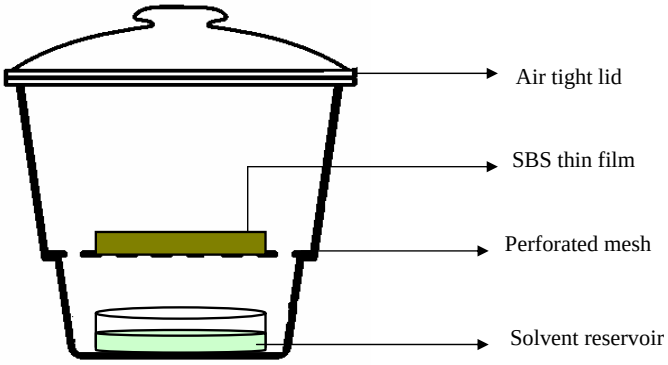

Figure 28: Schematic of the experimental set-up used for the solvent annealing process. The solvent reservoir contains 90 ml solvent in a 100 mm diameter glass petridish

It should be noted that the vapor pressure was not controlled in these experiments but the solvent atmosphere for all solvents was created in an identical way by using the same glass chamber (2200 ml volume) and 90 ml of solvent in a 100 mm diameter glass petridish.

3.2.3 Characterization techniques

3.2.3.1 Atomic Force Microscope

The sample surfaces were imaged using atomic force microscopy (AFM) in close contact mode (tapping mode). The AFM senses inter-atomic forces between the probe and the substrate. The imaging is achieved by recording the oscillation phase of a silicon cantilever terminated with a sharp tip, driven at its resonant frequency and scanned in close proximity to the polymer surface. An AFM set up is shown schematicallly in Figure 29.

Changes in sample height are detected by tip deflection and consequently the position of the reflected laser beam changes on the photodetector. In addition to obtaining height information, changes in the phase of the oscillation of the vibrating tip are a signature of varying surface hardness. In phase imaging, the oscillating

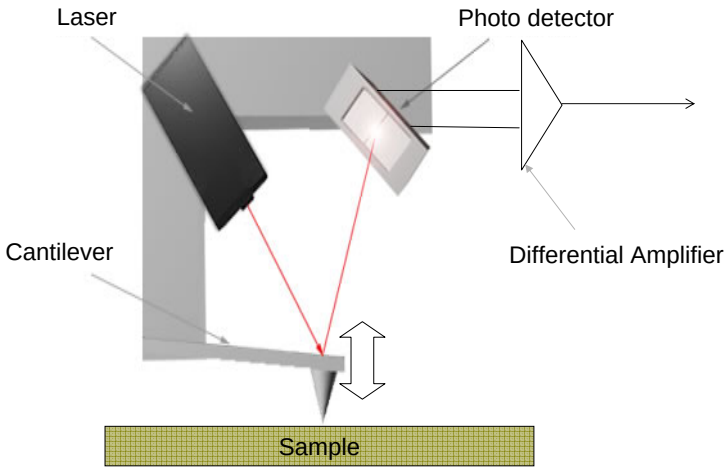

Figure 29: Atomic force microscopy set up showing the cantilever tapping on the surface of the sample. The laser spot is focussed on the back of the cantilever and reflected onto a photodetector (Reproduced from [143]).

amplitude of the tip is held constant by a feedback mechanism. The phase lag in the cantilever's oscillation and the signal sent to the cantilever's piezo driver are simultaneously monitored. When the tip (attached to the cantilever) taps a hard region of the surface, there is little phase lag in the cantilever's oscillation resulting in observation of a higher phase signal (brighter region in the image). Conversely when the tip hits a soft surface, there is a significant phase lag producing a very low signal (dark region in the image). A phase image thus reveals elastic modulus contrast on the sample surface.

In the case of a polystyrene-block-polybutadiene copolymer sample, for example, a hard PS microdomain yields a higher phase than that of the softer PB as shown in Figure 30. One can therefore image the lateral morphology of the BCP microdomains in a thin film by recording this phase image even if there is very little information obtained from the height image.

For our experiments, a Pacific Nanotechnology Nano-R atomic force microscope has been used operating in close-contact mode. Pyramidal shaped silicon tips of resonant frequency 250-300 kHz and radius less than 10 nm have been used. Processing

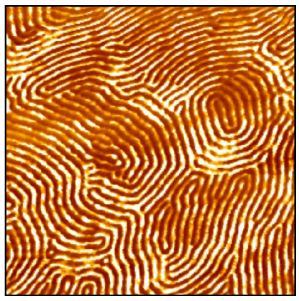

Figure 30: AFM phase image of SBS triblock copolymer where PS phase is the brighter phase.

and analysis of AFM images were performed with Nanorule software (provided by Pacific Technology). Use of Fourier transforms is a useful complimentary tool for evaluating the AFM micrographs as shown in Figure 31. For instance, a sample with a characteristic domain spacing but which is disordered in its orientation such as seen for a randomly ordered SBS cylinder forming thin film (see Figure 31(a)), the FFT shows a well defined halo. If on the other hand, the sample has a characteristic domain spacing which is well ordered, such as shown in Figure 31(b), a series of diffraction spots rather than a halo is observed in the FFT. For a disordered system, the FFT has no defined structure and the result is a diffuse scattering pattern.

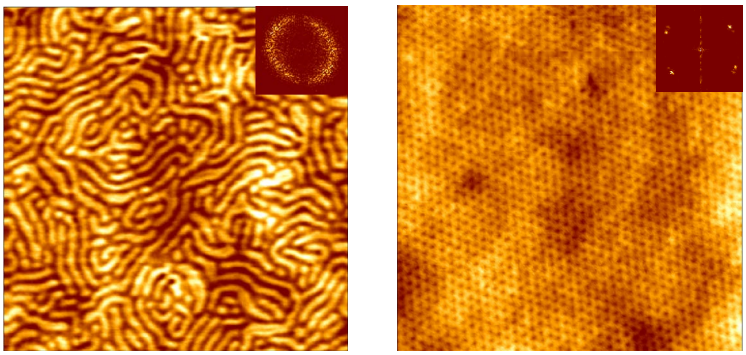

(a) disordered sample (b) ordered sample

Figure 31: Figure shows FFT insets of disordered (left) and ordered (right) SBS-I triblock thin films

3.2.3.2 Grazing Incidence small angle X-ray scattering

Grazing incidence small angle X-ray scattering (GISAXS) is essentially SAXS performed in the Bragg (reflection) geometry [144, 145]. A monochromatic X-ray beam is incident on a sample at a grazing angle α_i, typically, just above the critical angle α_c of the material (see Figure 32). The scattering observed is from objects on the surface of the film as well as a small depth below the surface caused by the scattering from an evanescent wave that extends a few tens of nanometers into the film. This penetration depth into the sample increases as the grazing incidence angle increases. The intensity of scattered X-rays is recorded by a two-dimensional detector and the scattering direction is described by the exit angle α_f and the out-of-plane angle ψ. GISAXS provides information both about lateral and normal ordering at a surface as

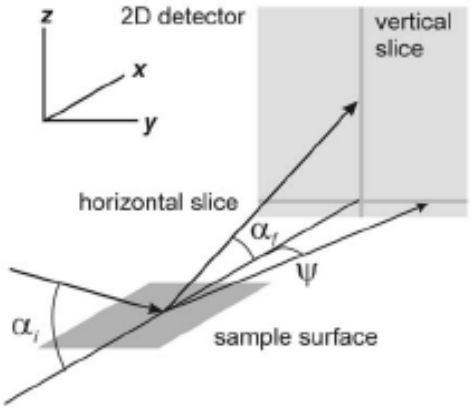

Figure 32: A schematics of the geometry for a GISAXS experiment (modified from [146])

well as inside a thin film. This is shown schematically in Figure 33 with an example of lamellar films formed by symmetric diblock copolymers. In this sample, the signature of lamellae oriented parallel to the substrate in GISAXS are stripes of intensity at regular spacings along the Q_z direction associated with the Kiessig fringes from the specular reflection. Lamellae ordered perpendicular to the substrate create diffraction peaks at fixed Q_y which extends along Q_z. In all cases, GISAXS patterns are usually symmetric about the specular reflection ridge, which extends along Q_z at $Q_y = 0$.

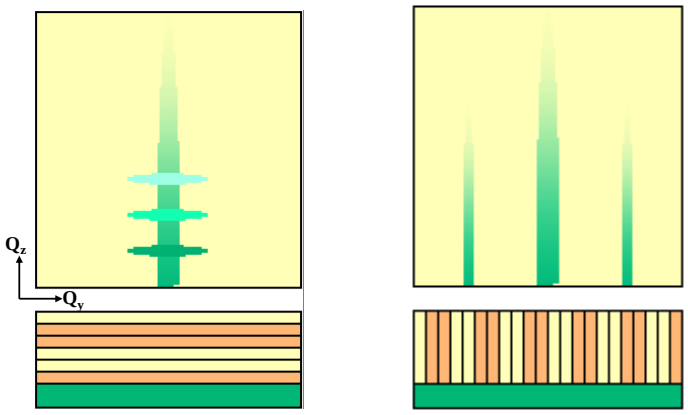

(a) Parallel lamellae

(b) Perpendicular lamellae

Figure 33: Schematics showing signature GISAXS patterns for a diblock copolymer film (Reproduced from [147])

GISAXS experiments were performed at station D1 at the Cornell High Energy Synchrotron source (CHESS) with X-ray wavelength of 1.23Å. A beam stop was installed in the position of the specular reflected beam at $Q_y = 0$. Rocking curves and height scans were performed for each sample using the ion chamber detector to determine the alignment of the sample relative to the incident beam. Once the sample was aligned, an X-ray reflectivity pattern was collected for each sample using the ion chamber detector over the incident angle range of 0.1 - 1^0. To change the incident angle, the sample was moved by using an automated goniometer. To measure GISAXS patterns, the ion chamber was removed and as for the SAXS experiments described above, a Medoptics CCD detector with 47.2 μm pixel resolution was used at a sample-to-detector distance of 1830 mm. In order to minimize any potential radiation damage, the sample was moved sideways after alignment, so that a pristine sample spot was exposed to the beam during measurements. All GISAXS images were corrected for background by measuring the dark current and the scattering patterns were analyzed using Fit2d software.

Figure 34 shows a typical 2D pattern obtained in our experiments where the ordered Bragg peaks can be seen in the Q_y direction.

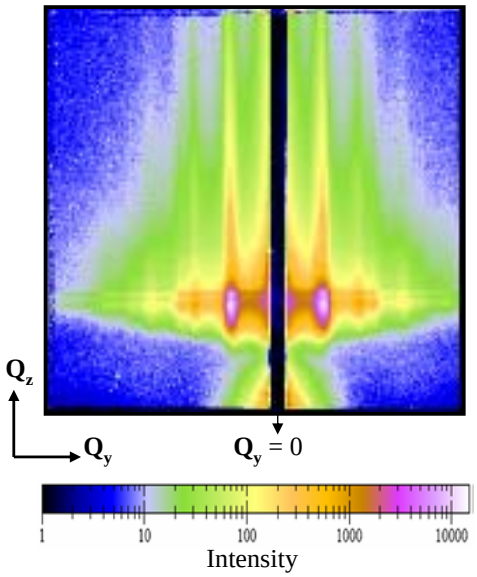

Figure 34: A characteristic 2D GISAXS pattern. The black vertical bar represents the position of the specular reflection masked by a beam stop.

In addition to the measurement of ex-situ annealed samples, preliminary in-situ experiments for solvent annealing experiments were carried out on a 50 nm SBS-I film using ethyl acetate vapors. The set up is shown schematically in Figure 35. The

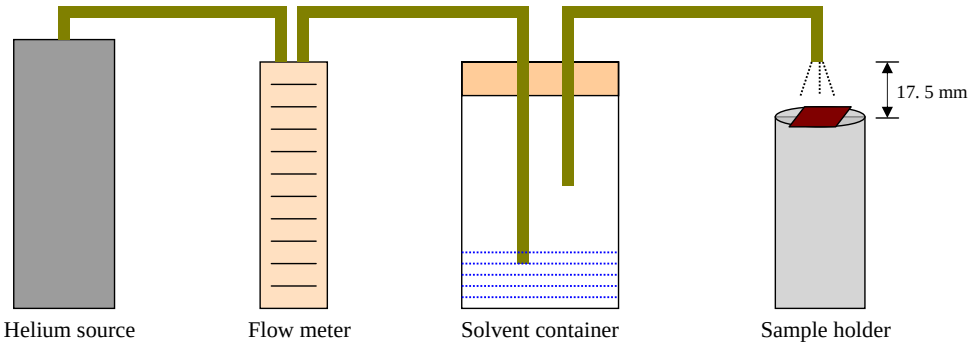

Figure 35: Sketch of the experimental set up for solvent (Ethyl acetate) annealing.

solvent flow rate was measured by using the E602 flow meter (from Matheson Trigas, Inc.). The distance between the sample and the exit point of the ethyl acetate vapors was 17.5 mm and the solvent flow rate used was 463 cc/min. In all cases, after about an hour, no GISAXS pattern was obtained from the film because the flow rate was sufficiently high enough to solvate the film and eventually dewet it from the surface.

Even though the flow rate of 463 cc/min was too high to maintain a homogeneous film, it was not possible to decrease the flow rate because it did not generate enough EAC vapors to reach the target film.

3.2.3.3 X-ray reflectivity

X-ray reflectivity is a non-contact technique for characterization of interfaces, thin films and multi-layers [148]. When the X-ray beam impinges on the surface of the film, it can either reflect from the surface when the angle of incidence is below the critical angle, or it can partially reflect and transmit into the film. The ratio of the reflected and incident beam is called reflectivity (R). When the incident and exit angles of the X-ray beam reflecting from a surface are equal, it is called specular reflectivity. The vector construction for specular reflectivity is shown in Figure 36 where $\vec{k_i}$ and $\vec{k_f}$ are the incident and the final vectors.

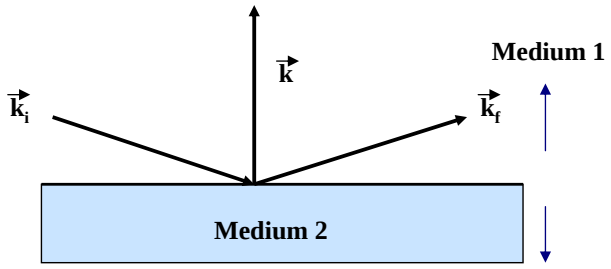

Figure 36: Vector construction of specular reflectivity from a flat surface

The specular reflectivity of the film is sensitive to changes in the electron density profile in the normal direction to the film surface, which provides detailed information about the structure variation as a function of the film thickness.

The X-ray reflectivity curves were obtained as part of the alignment procedure for the GISAXS measurements (section 3.2.3.2). The raw I_r vs. theta (θ) data (see Figure 37(a)) collected from the ion chamber were converted to Q by using $Q = (4\pi/\lambda)\sin\theta$ and corrected for geometry (see Figure 37(b)) using the relationship R

$= (I_r S)/(A_i \sin\theta)$ where I_r is the intensity of the reflected beam, S is the collimation slit gap (0.5 mm) and A_i is the sample size (25.4 mm). The corrected reflectivity was fitted by using SURFace software (freeware written by John Webster, ISIS, Rutherford Appleton Laboratory, UK) where the layer parameters were adjusted to get the best fit (using a least square fitting method) to the data. The interference fringes (often called Kiessig fringes) are a result of interference between the reflected beam and refracted beam, which is itself reflected by an underlying interface. These fringes therefore are a signature of the film thickness. Since the instrument is not optimized for XR measurements it has an inherent high background signal and low

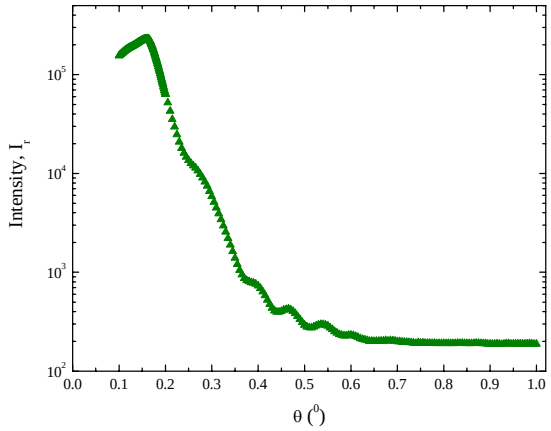

(a) R as a function of θ

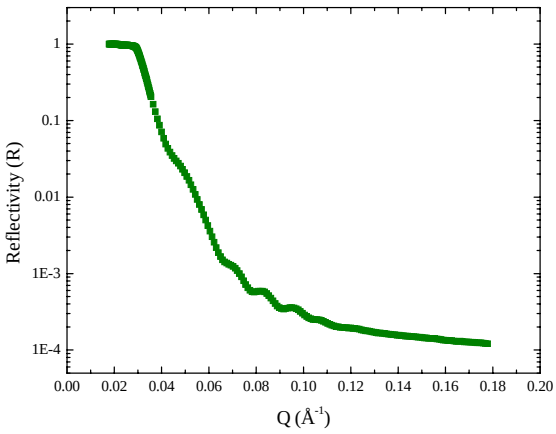

(b) R as a function of Q

Figure 37: The X-ray reflectivity curves - (a) Reflectivity (R) as a function of the incident angle (θ) collected from the ion chamber, and (b) - R as a function of momentum transfer vector, Q

resolution which masks a lot of information about the layer composition depth profile. Consequently, whilst the fits to the data are reasonably good there remains some degree of uncertainty in the parameters due to the effects of the high background and resolution.

CHAPTER IV

BULK COPOLYMER-NANOPARTICLE COMPOSITE STUDIES

The morphology of block copolymer (BCP) nanoparticle composites not only depends on the characteristics of the copolymer, but also on the characteristics (like size and shape) of the nanoparticles. The objective of this work is to study changes in block copolymer phase behavior with inclusion of nanoparticles. With the inclusion of different nanoparticles - gold (Au - 5 nm diameter) and buckminster fullerenes (C_{60} - 1 nm diameter) in the block copolymer system, changes in the bulk film phase behavior have been studied using the characterization tools of SAXS, TEM, NMR and DSC.

4.1 Gold nanoparticle inclusions

4.1.1 Structure Analysis results

4.1.1.1 SBS-I BCP-gold nanoparticle composites

Figure 38 shows the SAXS intensity patterns of SBS-I bulk samples both as a copolymer as well as pure and with gold nanoparticle inclusions added. The most intense peak at Q $\sim$ 0.18 nm^{-1} in all cases is the primary peak (Q_1). Other higher order peaks can also be observed and their positions are indicated by the arrows in Figure 38. The pure copolymer has a primary peak at $Q_1 = 0.184$ nm^{-1} which is equivalent to a domain spacing of 34.1 nm. The first order peak can be observed at Q = 0.32 nm^{-1} which is (approx.) equal to $\sqrt{3}Q_1$. Other peaks occur at Q = 0.370, 0.487, 0.552, 0.637 nm^{-1} equivalent to $\sqrt{4}Q_1$, $\sqrt{7}Q_1$, $\sqrt{9}Q_1$, $\sqrt{12}Q_1$. These peaks are characteristic of hexagonally ordered cylindrical morphology. The hexagonal morphology

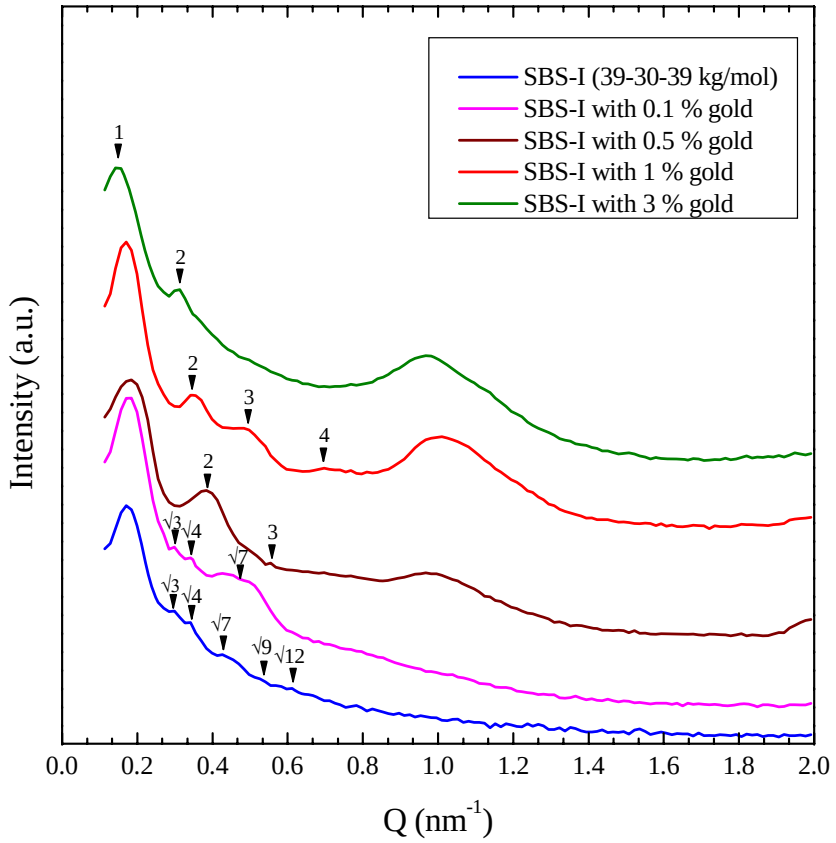

Figure 38: SAXS data - SBS-I system; SBS-I samples were measured using Bruker NanoStar instrument

is not unexpected in this case because the volume fraction of the PB minor phase is 0.32.

With 0.1% addition of gold in SBS-I, the primary peak Q_1 is observed at 0.176 nm^{-1} which is equivalent to a domain spacing of 35.6 nm. Other peaks are obtained at Q = 0.341, 0.459 and 0.465 nm^{-1} equivalent to $\sqrt{3}Q_1$, $\sqrt{4}Q_1$, $\sqrt{7}Q_1$, respectively, which is characteristic of a hexagonal morphology. There is no evident peak for gold at 0.1% inclusion. Clearly the addition of 0.1% gold nanoparticles does not change the morphology as compared to the pure polymer, but there is a slight increase in the domain spacing. This increase in domain spacing can be assumed to be due to the SBS-I increasing its volume to accommodate the gold nanoparticles within the structure. The morphology is not as ordered as the pure system as the higher order

peaks at $\sqrt{9}$, $\sqrt{12}$ are lost when gold is included.

As the gold loading increases to 0.5%, the primary peak Q_1 is observed at 0.176 nm^{-1} which is equivalent to a domain spacing of 35.6 nm. Other peaks are obtained at Q = 0.341, 0.352 and 0.528 nm^{-1} equivalent to $2Q_1$, $3Q_1$ respectively, which is characteristic of a lamellar morphology. So at a concentration of the gold nanoparticles between 0.1 and 0.5% (w/w), the hexagonal structure of the pure SBS-I transforms into a lamellar structure. For 0.1% and 0.5% gold inclusions, even though the average domain spacings obtained for 0.1% and 0.5% are the same, there is a difference in the distribution in the domain spacing which is discussed in detail in section 4.1.3. A broad peak centered at Q = 1.02 nm^{-1} characteristic of gold nanoparticles of size 6.1 nm was observed for 0.5% samples. The dimensions for gold obtained are slightly higher that the expected 5 nm, and this is likely to be due to weak aggregation rather than any increase associated with the presence of dodecanethiol around the gold nanoparticles.

With the addition of 1% gold to SBS-I, the primary peak Q_1 is observed at 0.170 nm^{-1} which is equivalent to a domain spacing of 36.9 nm. Other peaks are obtained at Q = 0.340, 0.510 and 0.679 nm^{-1} equivalent to $2Q_1$, $3Q_1$ and $4Q_1$ respectively, which as seen for the 0.5% sample is characteristic of a lamellar morphology. The gold peak in this case was centered at Q = 1 nm^{-1} which is equivalent to 6.3 nm. The size obtained for gold is slightly higher in this case as compared to the 6.1 nm obtained with the addition of 0.5% gold. This shift to larger dimensions with an increase in loading indicates an increasing degree of clustering of nanoparticles within the copolymer.

For SBS-I with 3% gold inclusions, the primary peak Q_1 is observed at 0.141 nm^{-1} which is equivalent to a domain spacing of 44.5 nm. The second peak is obtained at Q = 0.282 nm^{-1} equivalent to $2Q_1$, which is characteristic of a lamellar morphology. The broad peak at Q = 0.97 nm^{-1} characteristic of the gold nanoparticles of size

6.5 nm is clearly see for these samples indicating further weak aggregation of the nanoparticles. The higher order peaks at $3Q_1$ and $4Q_1$ visible in SBS-I with 1% gold inclusions are not observed in this case which indicates significant loss of order in the structure.

To compliment these data, TEM was carried out on these SBS-I samples. Cross-sectional morphology of these samples are shown in Figure 39. In these images, the dark regions are the osmium tetraoxide stained PB domain and the light regions are the PS domains. The observed morphologies are consistent with those obtained by SAXS measurements. The degree of order within each of the samples is clearly visible with defect density increasing from the pure to 0.1% gold nanoparticle sample. However, at 0.5% gold addition, the number of defects drops as the system switches to the lamellar morphology. The domain spacings from TEM micrographs are in agreement with the SAXS data.

4.1.1.2 SBS-II BCP-gold nanoparticle composites

The SAXS intensity patterns as a function of scattering vector for all the SBS-II bulk samples are shown in Figure 40. The most intense peak at Q $\sim$ 0.22 nm^{-1} in all cases is the primary peak (Q_1). Other higher order peaks can also be observed and their positions are indicated by the arrows in Figure 40. The pure copolymer has a primary peak at Q_1 = 0.224 nm^{-1} which is equivalent to a domain spacing of 28.1 nm. The first order peak can be observed at Q 0.376 nm^{-1} which is (approx.) equal to $\sqrt{3}Q_1$. Other peaks occur at Q = 0.437 and 0.567 nm^{-1} equivalent to $\sqrt{4}Q_1$ and $\sqrt{7}Q_1$. These peaks are characteristic of hexagonally ordered cylindrical morphology. The hexagonal morphology is not unexpected in this case as well because the volume fraction of the PB minor phase is 0.32.

With 0.1% addition of gold in SBS-II, the primary peak Q_1 is obtained at 0.222 nm^{-1} which is equivalent to a domain spacing of 28.2 nm. Other peaks are obtained

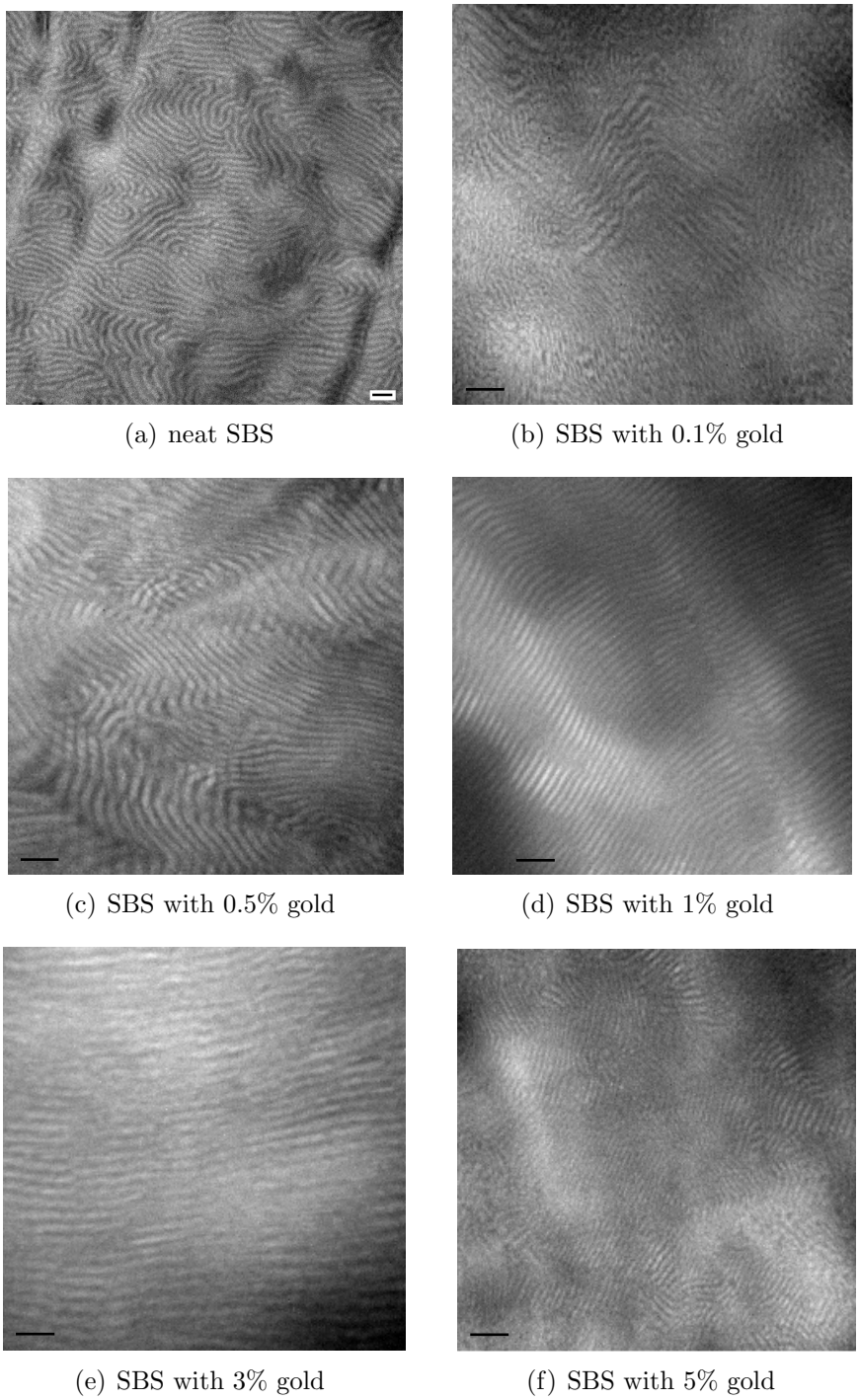

(a) neat SBS

(b) SBS with 0.1% gold

(c) SBS with 0.5% gold

(d) SBS with 1% gold

(e) SBS with 3% gold

(f) SBS with 5% gold

Figure 39: TEM micrographs of the cross section of SBS-I (pure and with gold inclusions). The phase morphology is hexagonal for pure SBS-I and SBS-I with 0.1% inclusions (a),(b); at 0.5% Au loading and higher, a lamellar morphology is observed (c-f). The scale bar in all figures is 100 nm.

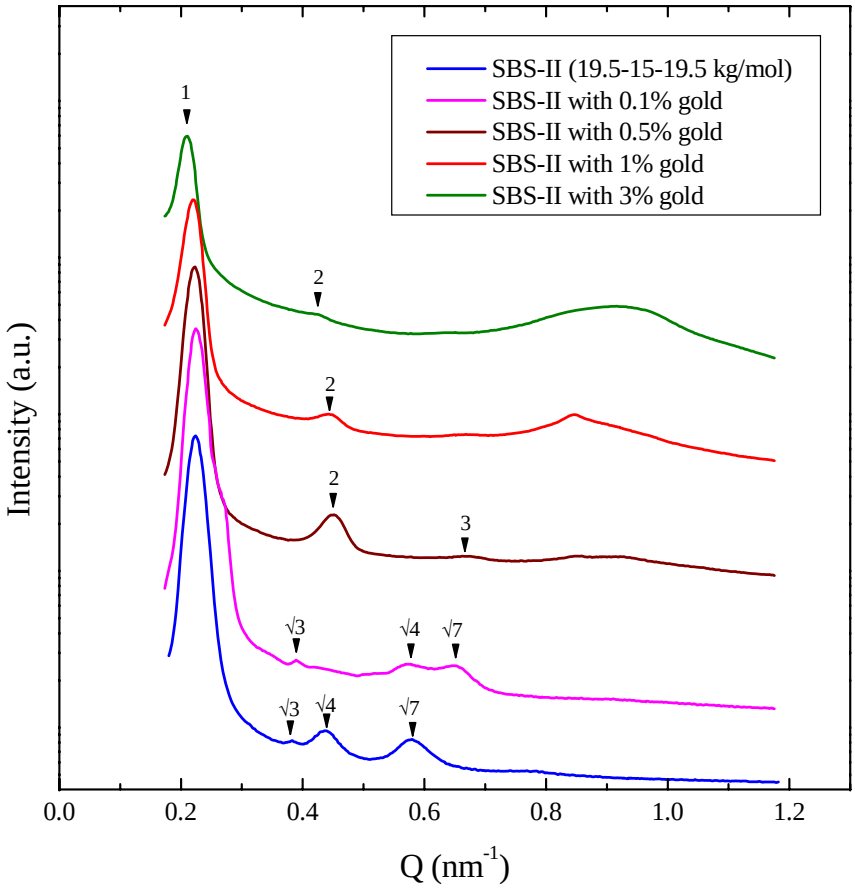

Figure 40: SAXS data - SBS II system; BCP samples were measured at CHESS

at Q = 0.386, 0.575 and 0.650 nm^{-1} equivalent to $\sqrt{3}Q_1$, $\sqrt{4}Q_1$, $\sqrt{7}Q_1$, respectively, and therefore is a hexagonal morphology[1]. There is no evident peak for gold at 0.1% inclusion. As we observed for the larger SBS-I equivalent triblock copolymer, the morphology of the pure and with 0.1% Au inclusions are the same but there is a slight increase in the domain spacing. All the higher order peaks observed in the pure polymer are also visible with 0.1% addition of gold.

As the gold loading increases to 0.5%, the primary peak Q_1 is observed at 0.221 nm^{-1} which is equivalent to a domain spacing of 28.4 nm. Other peaks are obtained at Q = 0.451, 0.673 nm^{-1} equivalent to $2Q_1$, $3Q_1$ respectively, i.e. a lamellar morphology.

[1]A peak (shoulder to the primary peak) is observed at Q = 0.27 nm^{-1} corresponding to a relative peak position of 1.2. This peak needs further investigation as it does not follow relative peak positions for the characteristic hexagonal morphology.

As before for SBS-I, at a concentration of the gold nanoparticles between 0.1 and 0.5% (w/w), the hexagonal structure of the pure SBS-II transforms into a lamellar structure. The broad peak of gold at Q $\sim$ 0.9nm^{-1} gives an Au dimension of 7.0 nm indicating some degree of aggregation.

With the addition of 1% gold to SBS-II, the primary peak Q_1 = 0.221 nm^{-1} gives a domain spacing of 28.4 nm. The only other peak is obtained at Q = 0.443 nm^{-1} equivalent to $2Q_1$, which is characteristic of a lamellar morphology. There is an indication of a higher order peak at Q = 0.673 nm^{-1} (equivalent to $3Q_1$) but it not clearly visible. The gold peak in this case was obtained at Q = 0.84 nm^{-1} which is equivalent to 7.4 nm. The peak shape of the gold is highly asymmetric which is probably due to the superposition of the Au peak with a higher order ($4Q_1$) for the lamellar structure.

For SBS-II with 3% gold inclusions, the primary peak (observed at Q_1 = 0.209 nm^{-1}) gives a domain spacing of 30.1 nm. A weak second order peak (Q = 0.422 nm^{-1}) obtained at $2Q_1$ indicates a lamellar morphology. The gold nanoparticle scattering gives the broad peak at Q = 0.94 nm^{-1} giving an average size of 6.7 nm, although the loss of peak intensity and lack of higher order peaks indicates lack of any extended ordering.

As with the SBS-I systems, the scattering from gold is more prominent as the loading levels increase. The characteristic peak for gold appears between 0.84 - 0.94 nm^{-1}, equivalent to an average gold nanoparticle size of between 6.7 nm and 7.5 nm. The distribution in the size increases as the percentage gold loading increases in SBS-II. This indicates that the gold nanoparticles are beginning to cluster since the average dimension is larger than the isolated gold nanoparticle.

4.1.1.3 SB-I BCP-gold nanoparticle composites

Figure 41 shows the SAXS intensity patterns as a function of scattering vector for all the SB-I bulk samples - pure and with gold nanoparticle inclusions. The pure

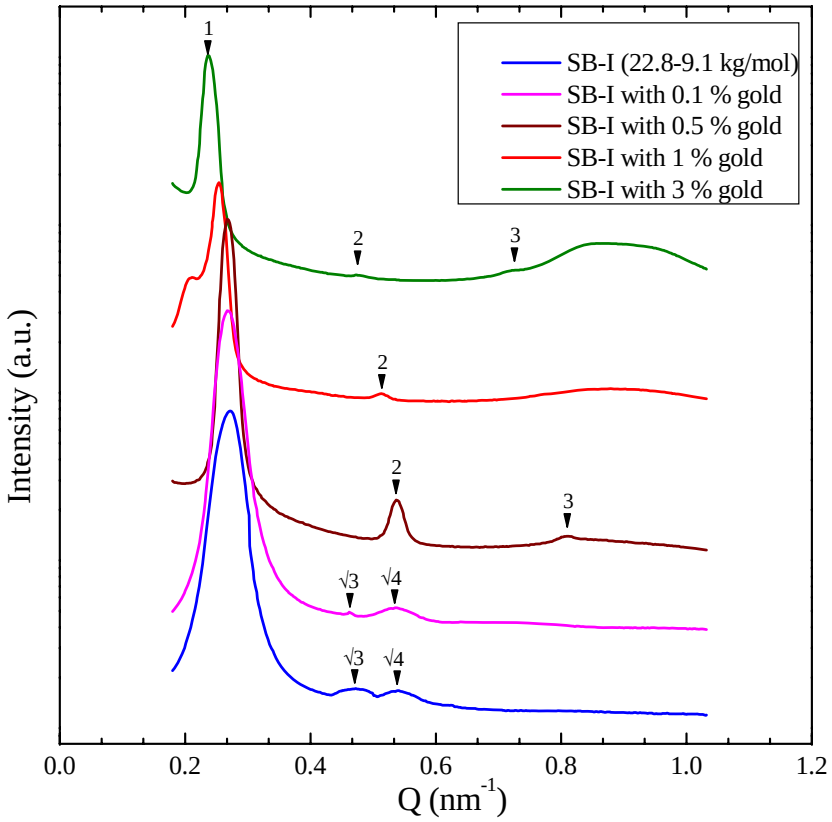

Figure 41: SAXS data - SB-I system; BCP samples were measured at CHESS

copolymer has a primary peak at $Q_1 = 0.273$ nm^{-1} which is equivalent to a domain spacing of 23.0 nm. The first order peak can be observed at $Q = 0.472$ nm^{-1} which is equal to $\sqrt{3}Q_1$. One other peak occurs at $Q = 0.541$ equivalent to $\sqrt{4}Q_1$. These peaks are characteristic of hexagonally ordered cylindrical morphology which is the expected morphology in this case since the volume fraction of the PB minor phase is 0.32.

With 0.1% addition of gold in SB-I, the primary peak Q_1 is obtained at 0.267 nm^{-1} which is equivalent to a domain spacing of 23.5 nm. Other peaks are obtained at $Q = 0.462$ nm^{-1} and 0.534 nm^{-1} equivalent to $\sqrt{3}Q_1$ and $\sqrt{4}Q_1$ which again is

characteristic of a hexagonal morphology. There is no evident peak for gold at 0.1% inclusion.

As the gold loading increases to 0.5%, the primary peak Q_1 is observed at 0.267 nm^{-1} which is equivalent to a domain spacing of 23.5 nm. Other peaks are obtained at Q = 0.542 and 0.816 nm^{-1} equivalent to $2Q_1$, and $3Q_1$, respectively, which shows that at a concentration of the gold nanoparticles between 0.1 and 0.5% (w/w), the hexagonal structure of the pure SB-I transforms into a lamellar structure.

With the addition of 1% gold to SB-I, the primary peak Q_1 is observed at 0.257 nm^{-1} which is equivalent to a domain spacing of 24.5 nm. The peak obtained at Q = 0.534 nm^{-1} ($2Q_1$) indicates a lamellar morphology, but the loss of the $3Q_1$ peak suggests that this structure is less ordered than the lamellar structure formed in SB-I with 0.5% gold inclusions.

A similar behavior is seen for SB-I with 3% gold inclusions with a primary peak Q_1 at 0.240 nm^{-1} (equivalent to a domain spacing of 26.2 nm). Only the second peak is obtained at Q = 0.498 nm^{-1} ($2Q_1$), indicating a poorly ordered lamellar morphology.

The broad peak seen in the Q range of 0.83 - 0.89 nm^{-1} for both 1% and 3% Au additions is associated with the gold. The dimension of the gold of between 7 and 7.6 nm indicate clustering of the nanoparticles.

4.1.1.4 SB-II BCP-gold nanoparticle composites

The SAXS intensity patterns as a function of scattering vector for all the SB-II bulk samples are shown in Figure 42. The most intense peak at Q $\sim$ 0.15 -0.2 nm^{-1} in all cases is the primary peak (Q_1). Other higher order peaks can also be observed and their positions are indicated by the arrows in Figure 42. The pure copolymer has a primary peak at Q_1 = 0.204 nm^{-1} which is equivalent to a domain spacing of 30.8 nm. The second order peak can be observed at Q = 0.290 nm^{-1} which is (approx.) equal to $\sqrt{2}Q_1$. Other peaks occur at Q = 0.353 and 0.408 and 0.546 nm^{-1}

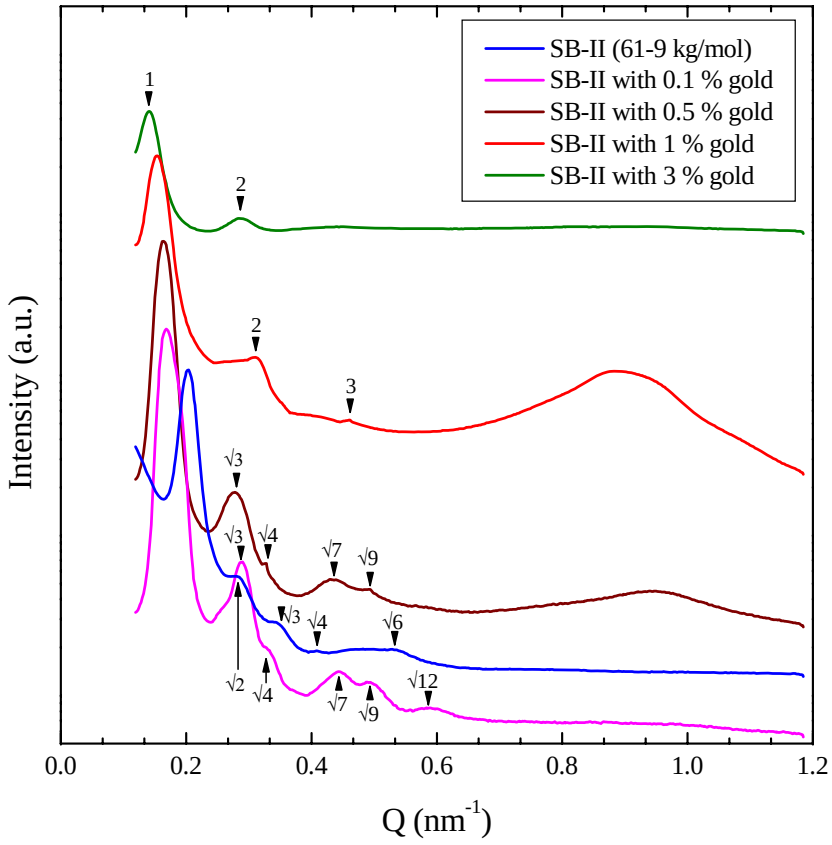

Figure 42: SAXS data - SB II system; BCP samples were measured at CHESS

equivalent to $\sqrt{3}Q_1$, $\sqrt{4}Q_1$ and $\sqrt{6}Q_1$. These peaks are characteristic of a spherical morphology where the minor component PB forms spheres in the PS matrix. The spherical morphology is not unexpected in this case as the volume fraction of the PB phase is 0.15.

With 0.1% addition of gold in SB-II, the primary peak Q_1 is obtained at 0.168 nm^{-1} which is equivalent to a domain spacing of 37.4 nm. Other peaks are obtained at Q = 0.290, 0.336, 0.443, 0.494 and 0.582 nm^{-1} equivalent to $\sqrt{3}Q_1$, $\sqrt{4}Q_1$, $\sqrt{7}Q_1$, $\sqrt{9}Q_1$ and $\sqrt{12}Q_1$ respectively, indicate a transition to hexagonal (cylindrical) morphology. At a loading of as low as 0.1%, the morphology of SB-I changes from spherical to hexagonal. For this sample, not only does the morphology change, but there are more ordered peaks in the transformed structure as compared to that of the pure polymer.

As the gold loading increases to 0.5%, the primary peak Q_1 is observed at 0.164 nm^{-1} which is equivalent to a domain spacing of 38.3 nm. Other peaks are obtained at Q = 0.283, 0.328, 0.438, 0.493 nm^{-1} equivalent to $\sqrt{3}Q_1$, $\sqrt{4}Q_1$, $\sqrt{7}Q_1$ and $\sqrt{9}Q_1$. These peaks are characteristic of a hexagonal morphology.

With the addition of 1% gold to SB-II, the primary peak Q_1 is observed at 0.154 nm^{-1} which is equivalent to a domain spacing of 40.8 nm. Other peaks are obtained at Q = 0.320 and 0.462 nm^{-1} equivalent to $2Q_1$ and $3Q_1$ which indicate that a transition to lamellar morphology has occurred. This structural transition from hexagonal to lamellar is accompanied with a significant loss in the structural order evident by the absence of the higher order peaks.

For SB-II with 3% gold inclusions, the location of the primary peak $Q_1 = 0.142$ nm^{-1} equivalent to a domain spacing of 44.3 nm and the second order peak (Q = 0.284 nm^{-1}, equivalent to $2Q_1$), indicates that this sample maintains lamellar morphology with an increase in the domain spacing.

As seen in other systems, there is no distinct gold peak for the lowest loading of Au nanoparticles of 0.1%. But for 0.5%, addition, a distinct peak is visible. In fact, the strongest scattering from gold is observed in the case of 0.5% and 1% and the corresponding nanoparticle dimensions are 6.7 nm (Q of 0.94 nm^{-1}), and 7.2 nm (Q = 0.87 nm^{-1}) respectively. It is not clear why no peak from gold was seen in case of 3% loading.

4.1.2 Location of gold

From the scattering data, we have seen that gold nanoparticle inclusions induce morphology transitions in all our BCP systems which was also confirmed by TEM images in the case of SBS-I gold nanoparticle composites (see section 4.1.1.1). However, no gold nanoparticles were observed in these TEM micrographs of stained samples (see Figure 43(a)). The most plausible reason is that these samples were stained with

osmium tetraoxide which may be obscuring the observation of the gold nanoparticles. So, TEM images for the same sample were taken but this time no staining was done. Figure 43(b) shows the unstained SBS-I with 1% inclusions where nanoparticles are clearly visible as a segregated series of aligned black dots running horizontally across the image. This is consistent with the lamellar morphology (Figure 43(a)) indicating the nanoparticles are being templated by the block copolymer. At a much higher magnification TEM image (see Figure 43(c)), the nanoparticles are clearly visible in the 1% gold sample as individually dispersed (predominantly) particles demonstrating that they are fully dispersed. The fact that the nanoparticles are clearly visible in these unstained samples indicates they must be located within the PB phase, which in the original TEM image (Figure 43(a)) is heavily stained. From these TEM images, it is not possible to fully distinguish whether the nanoparticles are present either in the bulk of PB phase, or at the PS-PB interface, or a combination of both these possibilities. To confirm which one of these possible situations is present, NMR measurements were performed.

^{1}H NMR spin-diffusion measurements were carried out by J. Leisen (Georgia Tech) on both the neat polymer and SBS-I with 1% gold inclusions. ^{1}H NMR spectra measured during the ^{1}H spin diffusion experiment is shown in Figure 44. Initially, all the components were magnetized to give a full ^{1}H NMR spectrum (Figure 44(a)). In the next step, a filter was used to dephase all the signal from the rigid components (PS in our case). The diffusion of magnetization from the mobile components (PB and thiol stabilized gold) to the rigid ones (PS) was then measured as a function of time (called the mixing time, t_m). The spin diffusion process was then analyzed by plotting the normalized intensity of the peaks from the protonated moieties as a function of the mixing time.

Results from spin diffusion experiments within the mobile phases (PB and thiol capped gold) are analyzed with respect to the different protons from PB and the thiol

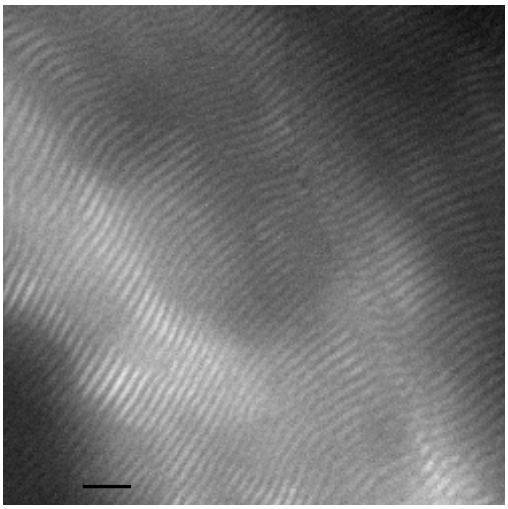

(a) SBS-I with 1% gold - stained with OsO_4. The scale bar is 100 nm

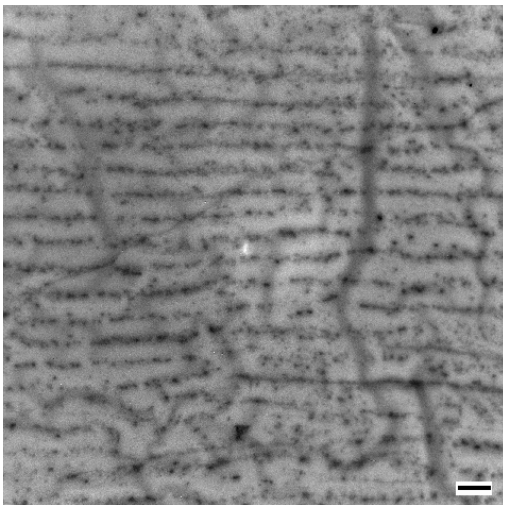

(b) SBS-I with 1% gold - no staining. The scale bar is 100 nm

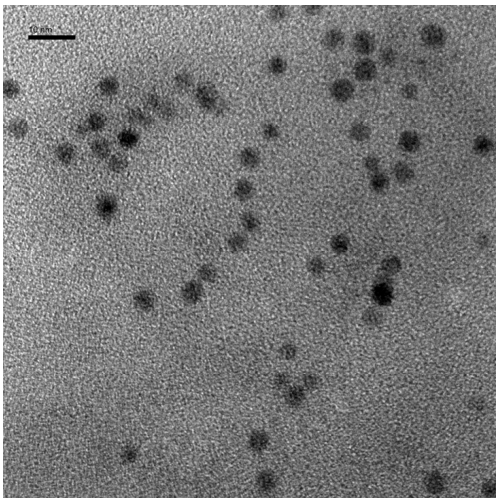

(c) TEM image of unstained SBS-I with 1 % gold at high magnification (200 kV). The scale bar on the top-left is 10 nm.

Figure 43: Representative TEM image of stained and unstained SBS-I with 1 % gold nanoparticles

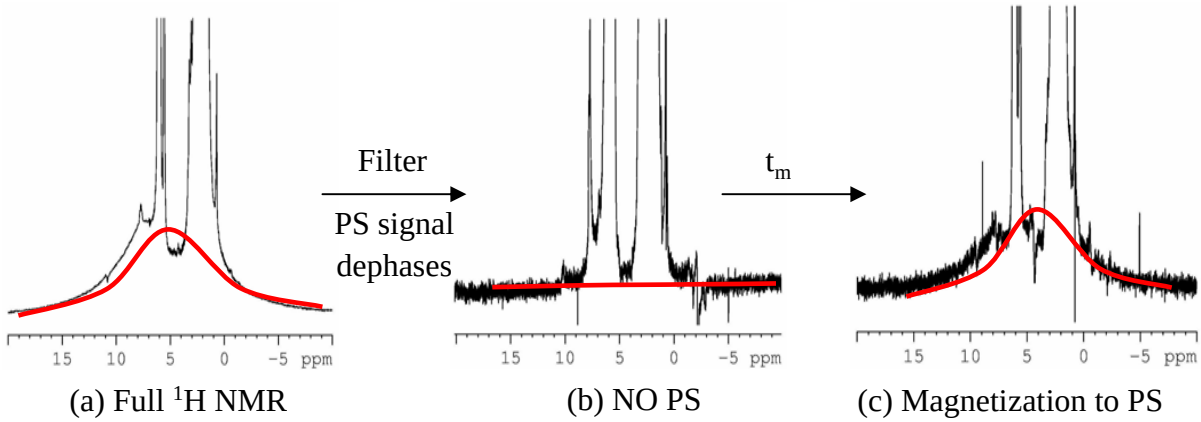

Figure 44: ^{1}H NMR spectra measured during ^{1}H spin diffusion experiment where the contributions to the NMR signal from the PS phase are highlighted with red lines on each curve. After exciting all the protons in the system, signal from the PS is dephased and a mixing time (t_m) is then allowed for spin diffusion to PS phase.

stabilizing the Au as shown in Figure 45(a). The 3 labeled peaks A and B correspond to the (-CH) and ($-CH_2$) protons in PB, respectively, and peak C corresponds to the ($-CH_2$) protons from the thiol stabilized Au (where the intensity of peak C represents $\sim$ 95% of the thiol in the system). The peak intensities are plotted with respect to the square root of the mixing time as shown in Figure 45(b). However, as can be seen in Figure 45, for SBS-I with 1% Au, spin diffusion not only occurred from the mobile phase (PB and thiol capped gold) to the rigid phase (PS) but also within the mobile phase was observed.

During the initial mixing time, there is an increase in the intensity of peak B as well as peak C whereas peak intensity of the peak A decreases. Ideally, if there is spin diffusion just to the PS components, the intensity of the mobile phase (peak A and peak C) would simply decrease. However, in this case the increase in the intensity of peaks B and C indicate a transfer of magnetization from peak A to peaks B and C both. Eventually at longer mixing times, the intensities of all peaks decrease, which indicates that spin diffusion only occurs to the rigid PS phase. This kind of spin diffusion within the mobile domain is only possible when all these protonated

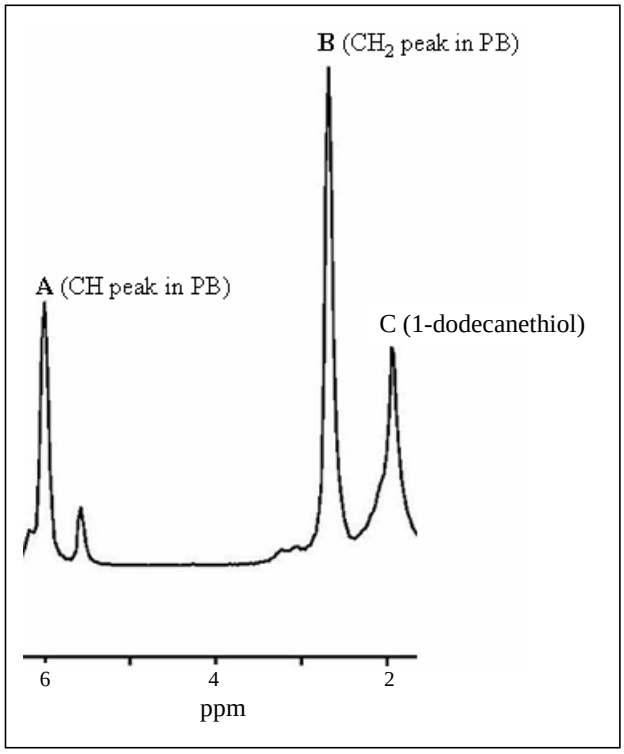

(a) 3 peaks within the mobile domain

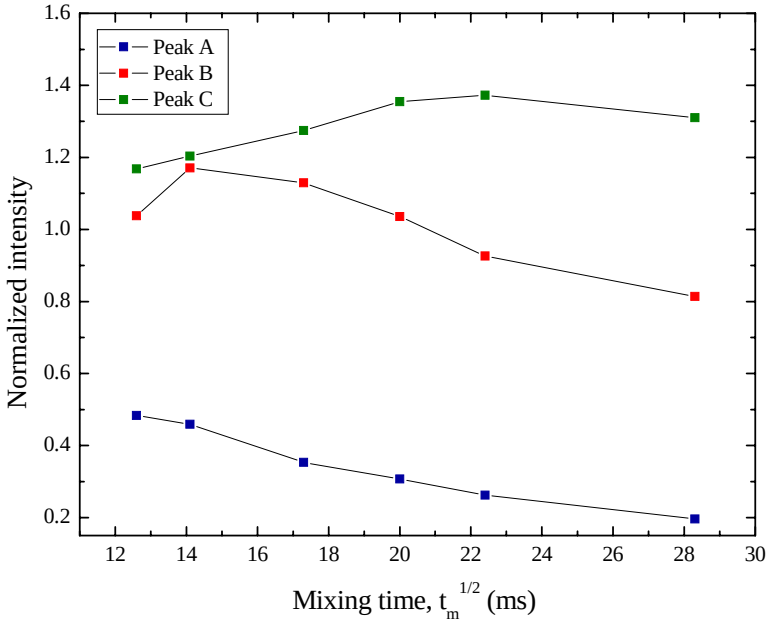

(b) Intensity as a function of mixing time

Figure 45: Spin diffusion NMR analysis within the mobile domain (PB and thiol capped gold)

moieties are in close vicinity to each other which would mean that thiol stabilized gold must be within the vicinity of the PB chains rather than PS chains. However, these data do not unambiguously determine whether the gold is solely in the the bulk of PB or whether there is any located at the PS-PB interface.

To confirm this, 2D exchange NMR experiments were carried out, and the resulting spectra (contour plots) from the SBS with 1% gold inclusions are shown in Figure 46. Figure 46(a) shows the initial data (at mixing time, $t_m = 0$ ms) for peaks A, B and C and Figure 46(b) shows the same peaks after 200 ms of mixing time.

At $t_m = 200$ ms, additional peaks called cross peaks are clearly visible (see Figure 46(b)) which indicates that transfer of magnetization within the moieties is occurring. The cross peaks appearing due to the transfer from peak A to peak B are indicated by the green lines. The red lines indicate a transfer between peak A to peak C and the blue lines indicate a transfer between peak B and C. This transfer between the moieties is possible only when they are in close proximity to each other.

To analyze these further, the rate of transfer of magnetization from peak A (CH in PB) to peak B (CH_2 in PB) and to peak C (thiol stabilized gold) were compared. The integrals of the intensities of peak B and peak C were normalized by the intensity integral of peak A and were plotted as a function of square root of the mixing time as shown in Figure 47. Since these intensities are already normalized by peak A intensity, the gradient (slope of the plot) of these plots for peak B and peak C give the rate of transfer of magnetization from A to peak B and to peak C respectively. The slope obtained for peak B is 0.300 and for peak C, the slope is 0.302. This means that the inter-molecular rate of transfer (from peak A to peak B) is the same as that of intra-molecular transfer (from peak A to peak C), which could happen only in the case where thiol-stabilized gold is located within the bulk of PB phase. Since peak C accounts for about 95% of the total thiol in the sample, it is safe to say that effectively all gold nanoparticles are within the bulk of PB phase and none at the interface or

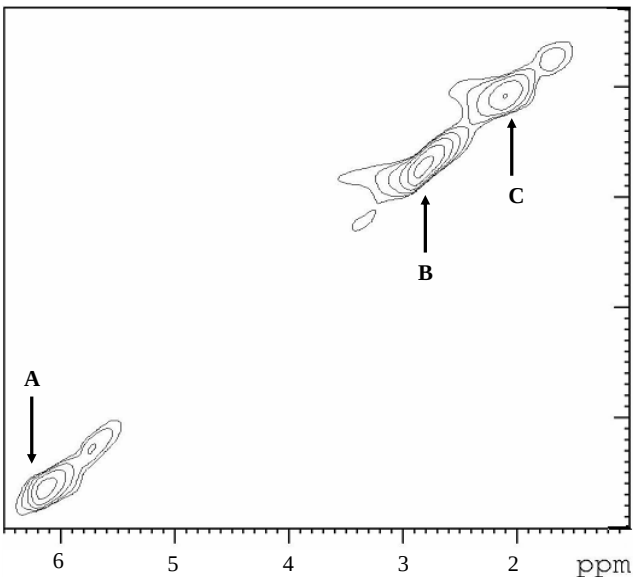

(a) Peak position at initial mixing time

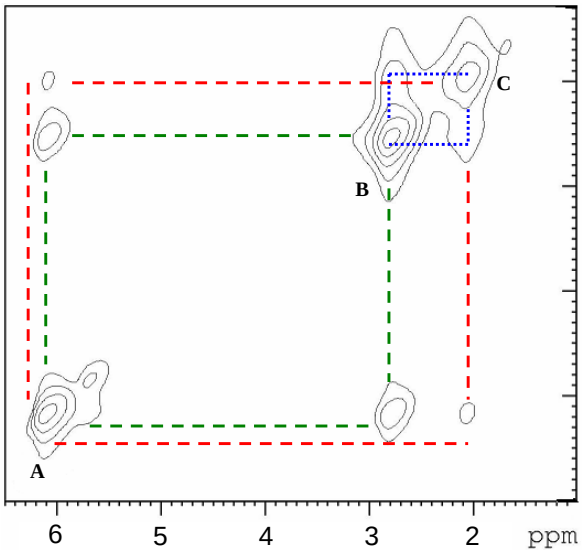

(b) Cross peaks appearing at 200 ms

Figure 46: 2D exchange spectra at (a) initial mixing time and (b) a mixing time of 200 ms (where the transfer reached saturation).

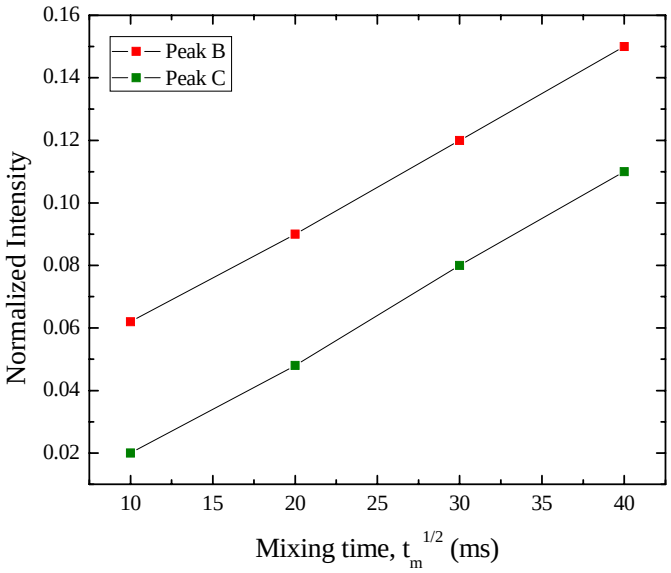

Figure 47: Normalized intensity of the ratio of peak C to peak B as a function of mixing time.

even in the PS phase.

The location of gold within the bulk of the PB domains is schematically shown in Figure 48. Location of gold in the PB phase can be rationalized by evaluating the

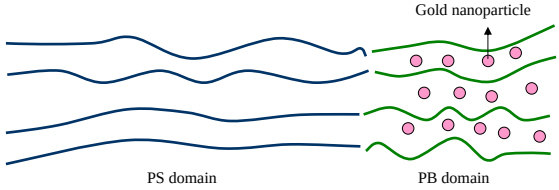

Figure 48: Schematics of location of gold nanoinclusions within the bulk of the PB phase.

surface energies of the various components. The interfacial energies between any two components A and B can be calculated using Equation 3.

$$\gamma_{AB} = \gamma_A + \gamma_B - 2\phi_{AB}(\gamma_A\gamma_B)^{1/2} \tag{3}$$

where:

$$\phi_{AB} = \frac{4(V_A V_B)^{1/3}}{(\sqrt[3]{V_A} + \sqrt[3]{V_B})^2} \tag{4}$$

γ_{AB} is the interfacial energy between A and B, γ_A and γ_B are surface energies of A and B, and V_A and V_B are the molar volume of the components. The surface energy and molar volume values in our case are [2]: for PS, γ_S = 43 mJ/m^2 and V_S = 98 cm^3/mol; for PB, γ_B = 32.5 mJ/m^2 and V_B = 60.7 cm^3/mol; and, for thiol stabilized gold, γ_{Th} = 22.2 mJ/m^2 [149] and V_{Th} = 239.53 cm^3/mol. Using these values, interfacial energies for PS and thiol, γ_{STh} = 4.8 mJ/m^2 and for PB and thiol, γ_{BTh} = 3.8 mJ/m^2. A lower value of interfacial energy in the case of γ_{BTh} implies that the thiol-stabilized gold nanoparticles will preferentially segregate to the PB phase over the PS phase of the block copolymer, as seen in the NMR experiments. .

4.1.3 Discussion

All our BCP systems undergo a morphology transition with the addition of gold. It has been theoretically predicted in case of triblock copolymers that there is a critical volume fraction of the minority block below which a system can not undergo any morphology transitions [150]. This critical volume fraction (ϕ_{crit}) is based relative ratio of the interfacial energies of the BCP components, for example in case of a ABC block copolymer, ϕ_{crit} is given by:

$$\phi_{crit} = \pi(1-f)^2/(2\pi - f)^2 \tag{5}$$

where f = $\gamma_{AC}/(\gamma_{AB} + \gamma_{BC})$; γ_{AC} is the interfacial energy between A and B components, γ_{AB} and γ_{BC} are the interfacial energies between (A, B), and (B, C) components respectively.

Using equation 5 for SBS, we found that in order for SBS to undergo a morphology transition, a PB volume fraction of 0.14 is needed. In our study, the minority block component (PB) in both SBS-I and SBS-II systems has a volume fraction of 0.32 which is well above the critical volume fraction needed to allow morphological transitions.

[2] γ_S, γ_B, V_S, V_B values were taken from reference [139]

These morphology transitions are accompanied by reduced structural order evident from the loss of higher order peaks in the SAXS data (see section 4.1.1). To compare the polydispersity of the resultant domain spacing in these structures, the primary peaks from the SAXS data are analyzed in Figure 49. The information about the degree of order can be estimated from the peak width of these peaks. For a perfectly ordered sample, a sharp and narrow peak should be obtained. However, polydispersity in the domain spacing and less order in the system due to gold addition will yield a broader peak around the same scattering vector value. To compare these

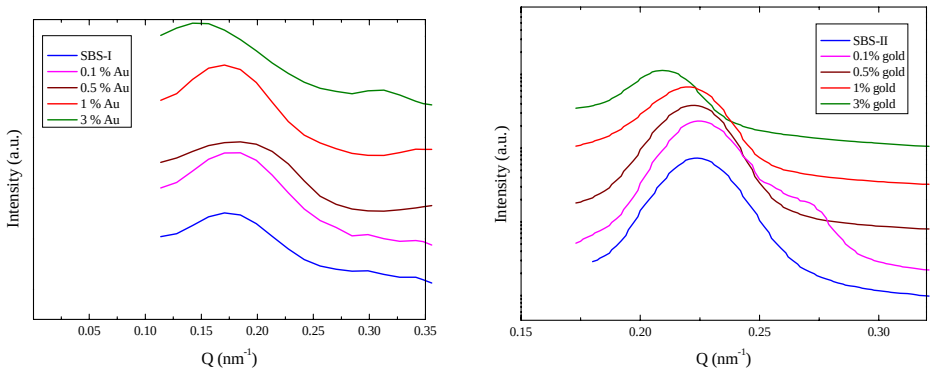

(a) SBS-I (b) SBS-II

(c) SB-I (d) SB-II

Figure 49: FWHM of the primary peaks from the scattering data of BCP-gold nanoparticle systems

peak widths, full width at half maximum (FWHM) was measured using Tablecurve 2D software (from SPSS, Inc) (see Figure 49). The Gaussian equation used to fit the

peak is given in Equation 6.

$$y = a + bexp[-0.5(\frac{x-c}{d})^2] \tag{6}$$

where c is the scattering vector value of the center of the primary peak, a and b are background and amplitude parameters and d is the Gaussian width (in nm^{-1}). The results from the FWHM analysis are summarized in Table 4. Although the error is

Table 4: Gaussian width (FWHM in nm^{-1}) of the primary SAXS peak for the BCP systems

Notation	SBS-I	SBS-II	SB-I	SB-II
0%	0.042	0.0123	0.0170	0.0091
0.1%	0.048	0.0119	0.0138	0.0123
0.5%	0.065	0.0121	0.0085	0.0110
1%	0.045	0.0149	0.0094	0.0174
3%	0.054	0.0148	0.0090	0.0176

high (approx.$\pm$10%) in these calculations, a trend of higher peak width for BCP-gold as compared to the pure BCP can still be observed (with the exception of some cases in SBS-II and SB-I). A higher peak width suggests that there is a distribution in characteristic repeat dimensions and that the BCP microstructure is less perfect. This may be because of the attempts of the BCP structure to accommodate the gold nanoparticles thereby resulting in perturbation in microstructure - be it cylinders or lamellae.

Table 5 summarizes the domain spacing and the respective morphologies for all the BCP-gold nanoparticle composites. In general, the increase in the domain spacing can be observed as higher amounts of gold are added to the BCP. The domain spacings from Table 5 are plotted in Figure 50. As Au nanoparticles are included in the system, the nanoparticles occupy a certain volume which means an increased volume for the system and thus, as more nanoparticles are added to the BCP, the characteristic spacing increases [37]. Since it has been established from TEM and NMR analysis that the gold nanoparticles are located in PB bulk, changes in the domain spacing

Table 5: SAXS data analysis - Dimensions (in nm) for BCP systems along with the corresponding morphologies

Notation	SBS-I	SBS-II	SB-I	SB-II
0%	34.1 (Hex)	28.1 (Hex)	23.0 (Hex)	30.8 (Sph)
0.1%	35.6 (Hex)	28.2 (Hex)	23.5 (Hex)	37.4 (Hex)
0.5%	35.6 (Lam)	28.4 (Lam)	23.5 (Lam)	38.3 (Hex)
1%	36.9 (Lam)	28.4 (Lam)	24.5 (Lam)	40.8 (Lam)
3%	44.5 (Lam)	30.1 (Lam)	26.2 (Lam)	44.3 (Lam)

with the addition of gold can be assumed to be affecting just the PB phase. Thus, it is possible to calculate the change in the apparent PB volume fraction with addition of different percentages of gold. This is done by assuming that with the addition of the gold, there is no change in the volume of mixing and since the gold is in the bulk of the PB phase, the increase in the domain spacing refers to an increase in the domain size of the PB phase. Figure 51 shows that change in PB volume fractions for SBS and SB BCP systems as a function of percent gold added. To analyze this further, the BCP radius of gyration (R_g) is calculated using Eq. 7 [151].

$$R_g = (1/6)^{\frac{1}{2}} a N^{\frac{1}{2}} \tag{7}$$

where a is the statistical segment length and N is the degree of polymerization. In our case, a is 0.7 nm for PS and 0.65 nm for PS and PB respectively [152]. Table 6 summarizes some of the characteristics of the BCP systems including R_g. R_p in the table refers to the radius of the nanoparticle where the thiol layer is assumed to be 0.5 nm [153] and N_{PB} refers to the number of PB repeat units in the BCP. For SBS systems, Figure 51(a) shows more apparent change in the PB volume fraction in SBS-I than that of SBS-II. Both these systems have the same volume fraction of PB but as can be seen from Table 6, the number of PB chains and the radius of gyration

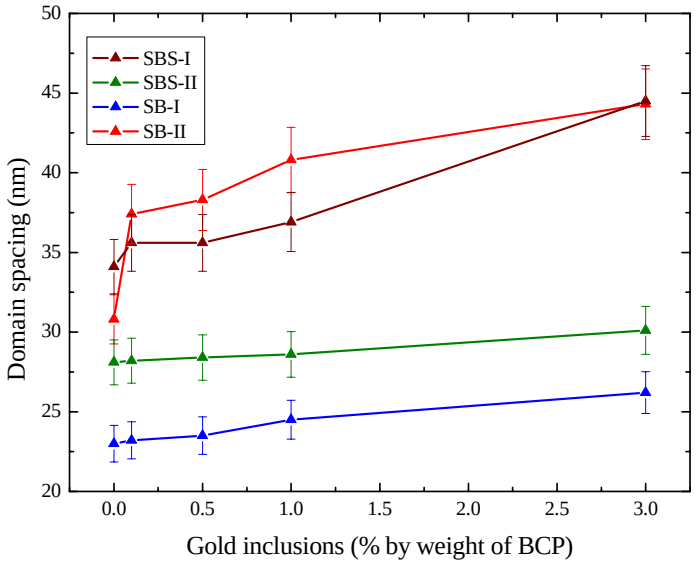

Figure 50: Change in BCP domain spacing as a function of percent gold inclusions

Table 6: Characteristics of the BCP systems

Notation	Mol. weight (kg/mol)	PB volume fraction	N_{PB}	R_g (nm)	R_p/R_g
SBS-I	108	0.323	556	14	0.21
SBS-II	54	0.323	268	9.7	0.31
SB-I	31.9	0.331	169	7.6	0.39
SB-II	70	0.151	167	10.3	0.29

is higher in SBS-I which explains the higher apparent volume change than SBS-II for the same percentage addition of gold. Comparing SB-I and SB-II diblock copolymers, (see 51(b)), it is evident that the PB volume fraction changes are higher in SB-II as compared to SB-I. This can be explained based on the starting PB volume fraction in both cases. SB-II in the pure state (no nanoparticles) has a lower PB volume than that of SB-I. The gold addition is based on the total weight of the BCP, consequently, even when the percent addition is the same in both the BCPs, the percent addition of gold relative to the PB phase is higher in SB-II than that of SB-I. Thus, a larger change is visible in the apparent PB volume in the case of SB-II.

When the nanoparticles are added to the BCP system, the system must find room for all included species. The volume occupied by the nanoparticle means increased

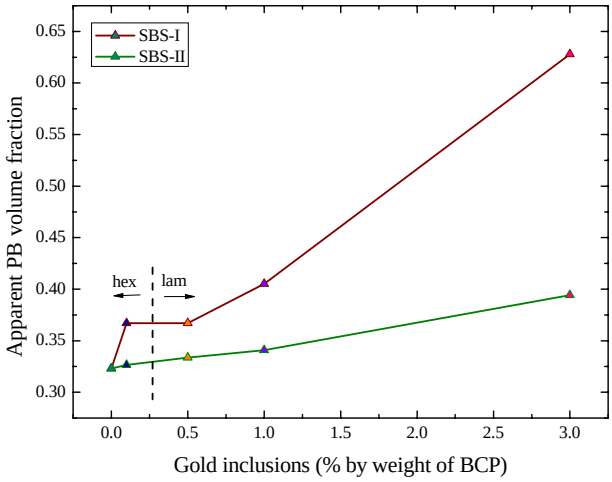

(a) SBS systems

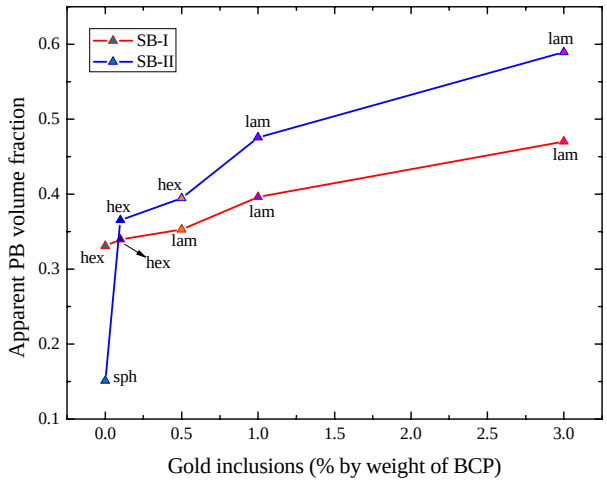

(b) SB systems

Figure 51: Apparent volume fraction change of PB in SBS-I and SBS-II BCPs as a function of percent gold inclusion

volume for polymers which would mean that to accommodate the nanoparticle, there will be rearrangement in the polymer chains, accompanied with a loss in conformational entropy and thus, a consequent increase in the domain spacing [37]. This increase in domain spacing is shown in a schematic representation of gold in the triblock copolymer in Figure 52 where the dimension (L_{PB}) of the PB phase increases to (L_{PB} + ΔL) with the addition of gold nanoparticles.

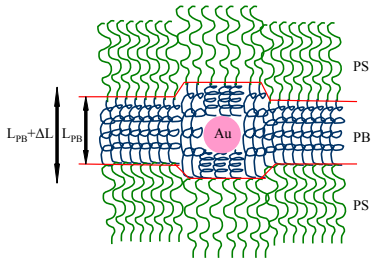

Figure 52: Schematic of nanoparticles in a triblock copolymer (concept from [37])

The evidence of the loss of mobility of PB chains associated with the predicted loss in conformational entropy that occurs due to accommodating the gold nanoparticles [154] can be seen from the analysis of the glass transition temperatures of the PB chains as shown in Figure 53. Figure 53 displays the thermograms of pure SBS-I and SBS-I with 1% gold inclusions. In both the systems, the glass transition of the PS phase remains unchanged at 93^0C (Figure 53(a)) since there is no gold present in the PS to cause any changes in the conformational entropy and thus the T_g remains unaffected even with the addition of gold. On the other hand, the glass transition (T_g) of the PB phase (Figure 53(b)) appears at -87^0C in the pure SBS-I but, in the presence of 1% gold inclusions, the T_g increases to -80^0C which indicates that the mobility of PB chains is retarded by the presence of gold inclusions.

Yeh et al. [72] have reported a morphology transition in PS-PVP diblock copolymers with the addition of CdS nanoparticles. This transition was caused by reduction in the effective interaction parameter of the BCP-nanoparticle composite due to hydrogen bonding between PVP and CdS nanoparticles. By comparison, in the SBS

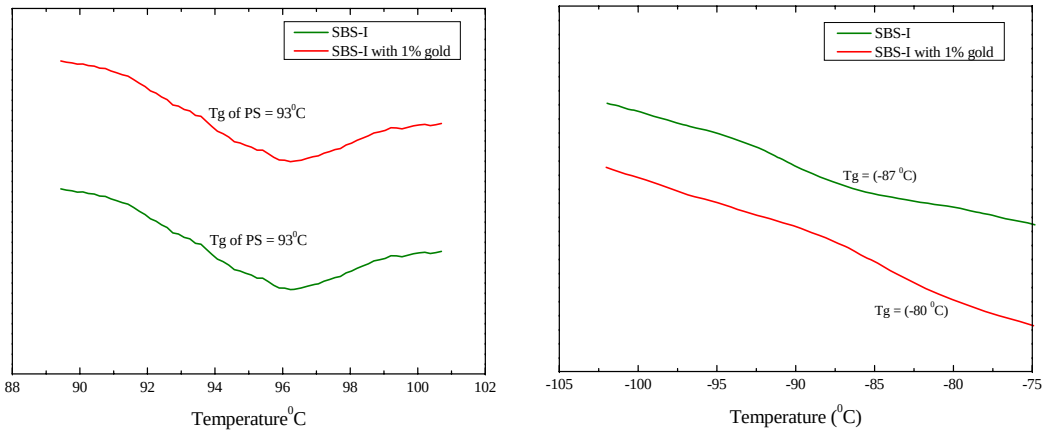

(a) T_g for PS (b) T_g for PB

Figure 53: DSC thermograms at second heating cycle for SBS-I and SBS-I with 1% gold inclusions. The glass transition temperatures of the PS and PB components are shown.

and SB systems, gold nanoparticles are located in the bulk of the PB phase and since there are no specific interactions between the stabilized gold and the PB, gold does not influence the effective interaction parameter between PS and PB phase. This being the case, the increase in the PB volume fraction must be the only reason for the morphology transition observed. This is shown schematically with reference to the theoretical phase diagram in Figure 54 where the system undergoes a morphology change maintaining the same interaction parameter, but increasing the value of f [70].

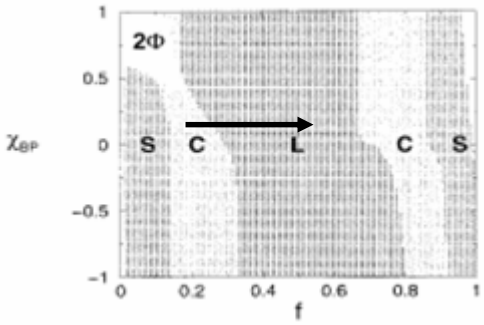

Figure 54: Theoretical phase diagram of the BCP-nanoparticle composite where S, C and L represent spherical, cylinders and lamellar morphology. The horizontal arrow indicates the morphology transition in our case upon selective segregation of gold Np in PB phase. χ used for PS-PB is 0.052 [152, 155](Modified Figure 1(a) from [70].

In case of diblock copolymers, the particles can be accommodated with ease in the bulk of PB domains because of the presence of PB chain ends which present additional free volume. For the triblock copolymers, there are no free ends in the PB domains but the particles still locate within the bulk of PB domains. This can be due to more flexibility of the PB chains in the bulk as compared to the chains at the interface.

4.2 Fullerenes (C_{60}) inclusions

Figure 55 shows characteristic SAXS scattering curves of C_{60} in the BCP systems. For SBS-I samples (see Figure 55(a)), the most intense peak at Q $\sim$ 0.170 nm^{-1} in all cases is the primary peak (Q_1). For SBS-I with 0.1% C_{60}, only the primary peak, Q_1 is observed at 0.168 nm^{-1} which is equivalent to a domain spacing of 37.4 nm. At 0.5% C_{60}, the primary peak is observed at a higher Q of 0.170 nm^{-1} corresponding to a domain spacing of 36.8 nm. Similar to 0.1% addition, no higher order peaks were observed. For SBS-I with 1 - 5% C_{60} additions, the primary peak, Q_1 is observed at 0.170 nm^{-1} equivalent to a domain spacing of 36.8 nm. For all the three (1, 3, 5%) samples, a higher order peak can be observed at Q = 0.45 nm^{-1} which is equal to $\sqrt{7}Q_1$.

In the case of SBS-II samples (see Figure 55(b)), the primary peak Q_1 is observed at 0.223 nm^{-1} for all percent C_{60} additions equivalent to a domain spacing of 28.2 nm. These samples also show a higher order peak at Q = 0.59 nm^{-1} which is equal to $\sqrt{7}Q_1$.

SB-I with 0.1% C_{60} (see Figure 55(c)) just shows a primary peak $Q_1 = 0.278$ nm^{-1} equivalent to a domain spacing of 22.6 nm. For SB-I with 0.5% - 1% C_{60} additions, the primary peak shifts to a slightly lower value of $Q_1 = 0.274$ nm^{-1} corresponding to a domain spacing of 22.9 nm.

In the case of SB-II, a primary peak, Q_1 is observed at 0.205 nm^{-1} (see Figure

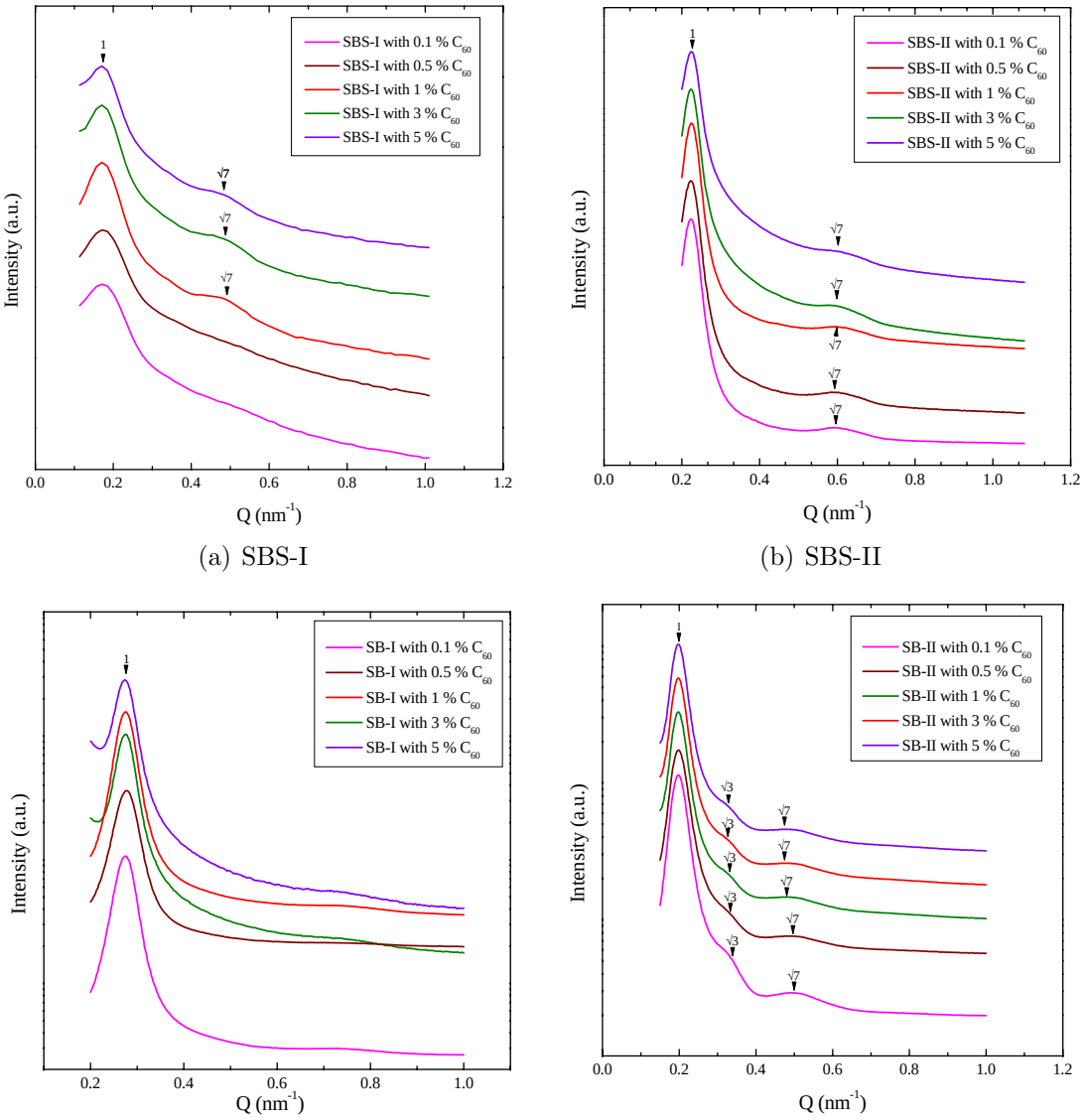

Figure 55: SAXS patterns for neat SBS and with different percent C_{60} inclusions (SBS-I samples were measured using Bruker NanoStar instrument; rest of the BCP samples were measured at CHESS)

55(d)). Two higher order peaks are seen at Q = 0.355 and 0.542 nm^{-1} equivalent to $\sqrt{3}Q_1$ and $\sqrt{7}Q_1$, respectively. The pure polymer has a spherical morphology (as discussed in section 4.1.1.4) but addition 0.1% C_{60}, causes a morphology transition from spheres to hexagonal cylinders. The reasons are not clear for this morphology transition given that C_{60} does not have any significant effect in other BCP systems.

The structures of the BCPs are not as ordered as in the case with BCP-gold composites (see section 4.1). This is most likely because of the preparation method used to create these composites which was different from that used for BCP-gold composites. While BCP-gold composites were made by solution casting, these BCP-C_{60} composites were made by the precipitation method (see section 3.1.2.3). This rapid precipitation method is unlikely to give enough time for high ordering of the BCP. In addition, even though C_{60} nanoparticles are small in size, there is a possibility that they affect the polymer chain ordering which will again result in loss of higher order peaks in the BCP. The information from the BCP - C_{60} systems is summarized in Table 7. It is clear that for each of the copolymers, there is not much change

Table 7: Dimensions (in nm) for block copolymer with C_{60} inclusions

Notation	SBS-I (R_p/R_g=0.03)	SBS-II (R_p/R_g=0.05)	SB-I (R_p/R_g=0.06)	SB-II (R_p/R_g=0.05)
0.1%	37.4	28.2	22.6	30.6
0.5%	36.8	28.2	22.9	30.6
1%	36.8	28.2	22.9	30.6
3%	36.8	28.2	22.9	30.6
5%	36.8	28.2	22.9	30.6

in the domain spacing as the C_{60} is added to the block copolymer. Since the C_{60} nanoparticles are small enough in size compared to the dimensions of the BCP (R_g) as shown by the ratio $R_p/R_g \leq 0.06$, a considerable amount of nanoparticles could in principle be accommodated with out changing the structure of the BCP.

To further characterize the morphological effect of the addition of C_{60} to the block copolymers, TEM imaging was carried out on SBS-I system, as shown in Figure 56.

From the TEM micrographs, it can be seen that the domain structure is poorly ordered and that there is no apparent change in the structure with increasing C_{60} loading which is consistent with the SAXS data for SBS-I. Since the location of the C_{60} in the BCP is not known with any certainty, two possible scenarios are suggested in Figure 57.

Figure 57(a) shows C_{60} dispersed in both the phases which could be because the small size gives the nanoparticles freedom to be located homogeneously throughout the BCP. The other possibility is that the C_{60} is located in the PS phase as shown in Figure 57(b). This latter case is more probable based on the recent work carried out on PS-PDMS block copolymer where it was experimentally shown using ^{1}H spin diffusion and ^{1}H-^{13}C cross-polarization measurements that C_{60} has a limited solubility in PS and therefore only segregates into the PS phases of this polymer [156]. Since these are small nanoparticles, the stretching required by the block phases to accommodate the particle would not be significant. Any entropic penalty that the C_{60} nanoparticles cause on the chains is overcome by the entropic gains of particle distribution. Further work needs to be done to determine the location of C_{60} in our samples using NMR experiments.

4.3 Conclusions

For two different sizes of nanoparticles, physical blends of triblock and diblock copolymer with varying concentrations of nanoparticles have been investigated.

Gold nanoparticle inclusions segregate in the PB domains of the BCP systems as shown by TEM and NMR data. The morphological transformation by the inclusion of gold nanoparticles in all the BCP systems (SBS as well as SB) was clearly observed using SAXS and TEM. The transformation can be explained based on the increase in the apparent volume fraction of PB phase with the addition of gold, which changes the effective (apparent) volume fraction of the PB phase.

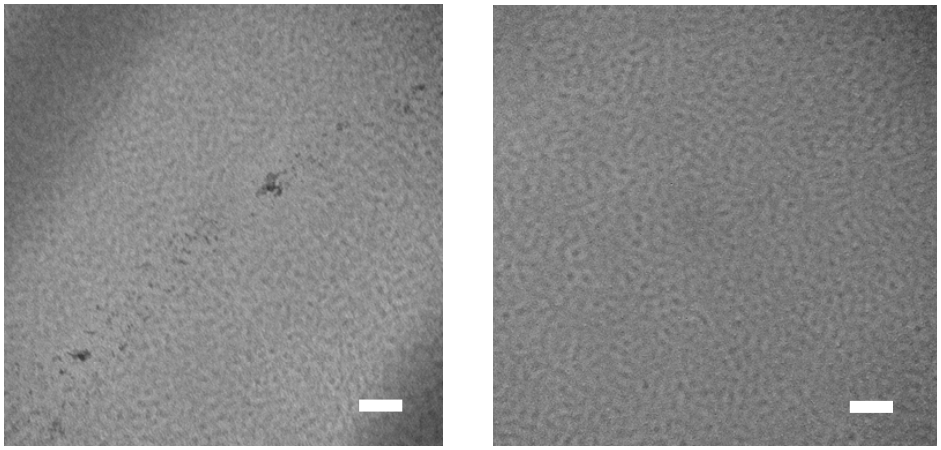

(a) 0.1% C_{60} (b) 0.5% C_{60}

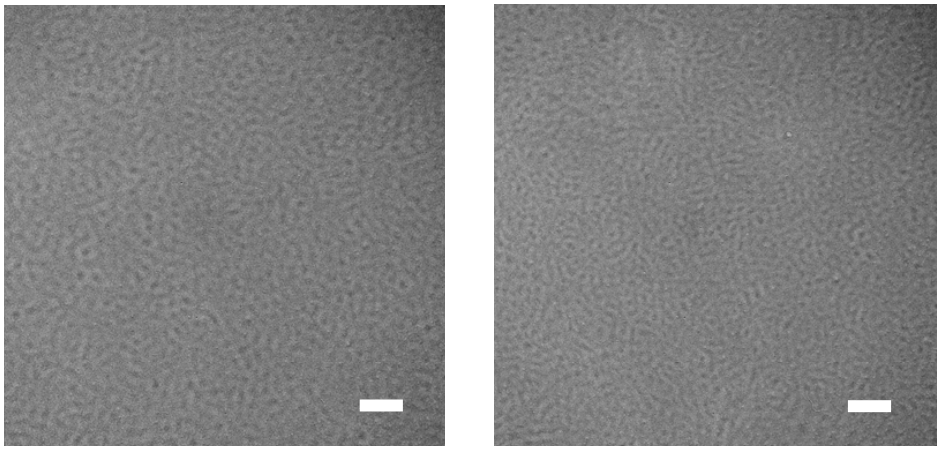

(c) 1% C_{60} (d) 3% C_{60}

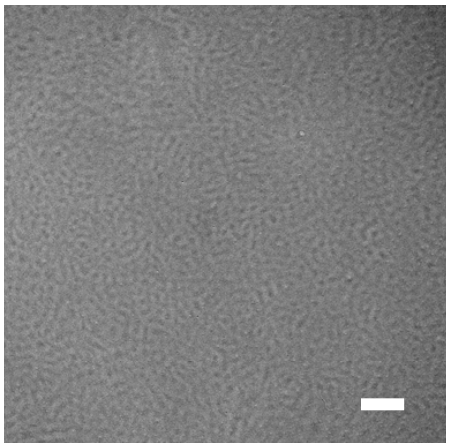

(e) 5% C_{60}

Figure 56: TEM micrographs of the cross section of SBS-I with C_{60} inclusions. The scale bar in all figures is 100 nm.

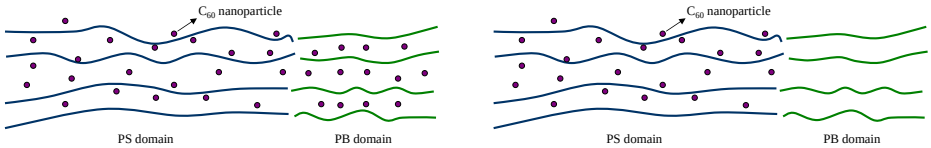

(a) C_{60} in PS and PB phase (b) C_{60} in PS phase

Figure 57: Schematic of the location of C_{60} nanoparticles in BCPs

In the case of C_{60}, only one morphology transition was observed in SB-II BCP where the structure changed from spheres to cylinders with the addition of 0.1% C_{60}. There was no significant increase in the domain spacing which is assumed to be because of the small size of the nanoparticles.

Knowledge gained from these studies will be helpful in tailoring the properties of BCP-nanoparticle composites.

CHAPTER V

LONG RANGE ORDERING (SOLVENT ANNEALING) STUDIES

In the absence of external fields, equilibrium morphologies of BCP's display grain-like structure with no long-range order. One effective mechanism of achieving this long-range order is the use of solvent vapor annealing - exposure of the polymer to solvent vapor for differing times. The solvent imparts mobility to the system, screens the segmental interactions, thus enabling alignment of the microdomains without any thermal treatment [84, 95]. On exposing spun cast thin films (50 nm and 260 nm) of styrene-butadiene-styrene (SBS-I of molecular weight 39-30-39 kg/mol) triblock copolymers to different saturated solvent vapors, the changes in the morphology of the film and the long-range order have been studied with respect to the solvent vapor quality and selectivity, solvent exposure time and the substrate surface energy. AFM imaging was performed to visualize the surface morphology of the solvent annealed SBS-I films. GISAXS measurements were also performed on these films to provide complementary information about the internal structure of the film.

Building on the work already done by others in the area of solvent annealing (see Section 2.3.1), studies were undertaken in two distinct categories - films that were spun cast and annealed in the same solvent, and films spun cast in one solvent and annealed in another. Figure 58 shows AFM micrographs of 260 nm thick films of SBS-I, which were spun cast and annealed in the same solvent. For all the micrographs, the FFT image is shown as the inset in the top right hand corner. Starting with the toluene series shown in Figures 58(a) - 58(c), it can be seen that the as-made film has no distinct features in the surface morphology which is also evident in the diffuse

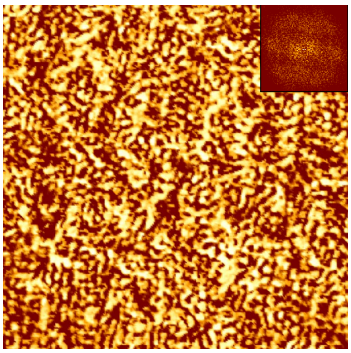

(a) SBS (as-made) in toluene

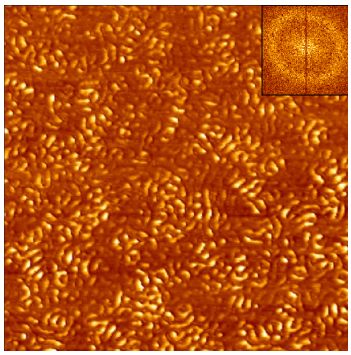

(b) Toluene vapors - 48 hours

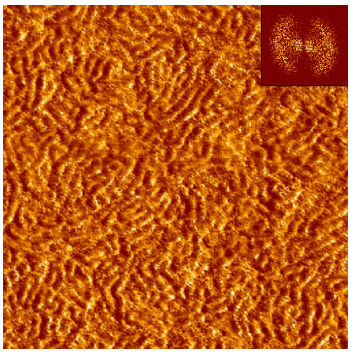

(c) Toluene vapors - 7 days

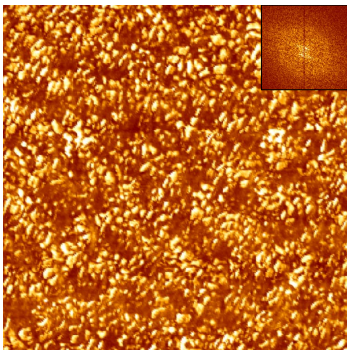

(d) SBS (as-made) in cyclohexanone

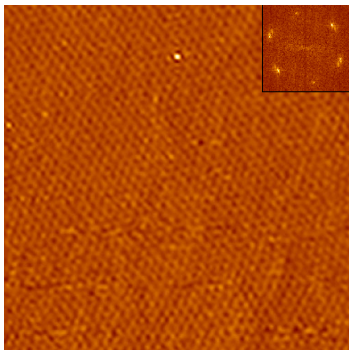

(e) Cyclohexanone vapors - 48 hours

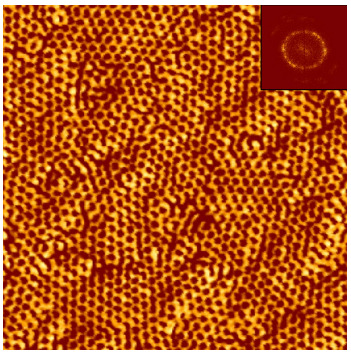

(f) Cyclohexanone vapors - 7 days

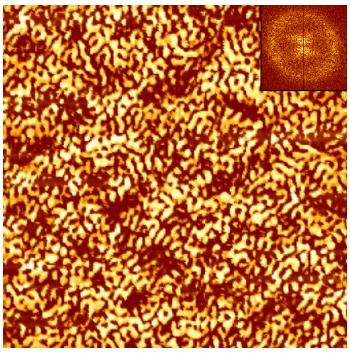

(g) SBS (as-made) in chloroform

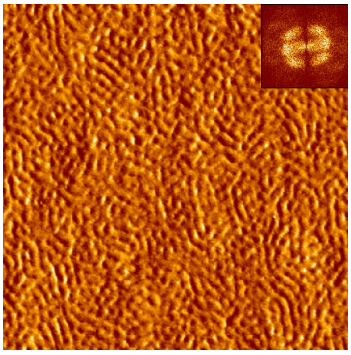

(h) Chloroform vapors - 48 hours

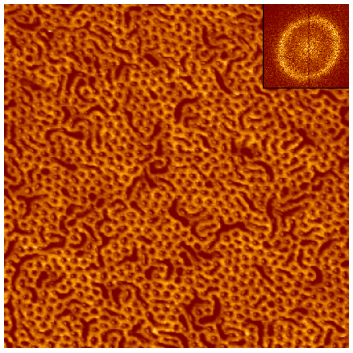

(i) Chloroform vapors - 7 days

Figure 58: AFM phase images (1.5μ x 1.5μ) showing the effect of solvent annealing in the vapors of the spin casting solvent on 260 nm thick SBS-I (4%) film. The bright phase is PS and the dark regions represent the PB phase.

scattering without any apparent structure in the FFT image. After solvent annealing in the same solvent for 48 hours (see Figure 58(b)) and 7 days (see Figure 58(c)), the film surface develops a more defined structure which is seen in the FFT inset as the clearly defined halo. A similar type of ordering behavior is observed for films spun cast and annealed in chloroform as shown in Figures 58(g) - 58(i). The film clearly becomes more ordered after annealing for 48 hours and 7 days as compared to the as-made film. In this case the domains appear to be largely spherical. But, given the worm like structures that are observed and the results from SAXS measurements, the domains are more likely to be cylinders aligned perpendicular to the surface. In this case, the PB seems to form the minor component and therefore the core of the cylinder. The most promising system, in terms of long-range order is the SBS-I film spun cast and annealed using cyclohexanone. As before, the as-made film is mostly disordered (see Figure 58(d)), but when annealed for 48 hours in cyclohexanone, a well defined structure is formed with a hexagonal morphology with a remarkable degree of ordering, which is evident from the 6 spots observed in the FFT image. This structure is most likely due to alignment of cylinders with PB cores perpendicular to the surface. As the film is annealed for a further 7 days (see Figure 58(f)), the structure starts to disorder as is apparent from the FFT image where the ordered 6 spot pattern is lost. From this study, cyclohexanone was found to be a promising solvent for annealing.

These data can be compared to 260 nm thick films of SBS-I which were spun cast and solvent annealed using two different solvents (see Figure 59). In Figures 59(a) - 59(c), SBS-I spun cast in toluene was exposed to both cyclohexanone and chloroform vapors for 48 hours. After exposure to cyclohexanone vapors, a well ordered hexagonal structure is observed which is consistent with the previous results. Although chloroform does create sufficient ordered structure to give a diffuse halo in the FFT, no long-range order is observed (see Figure 59(c)). For the films spun cast

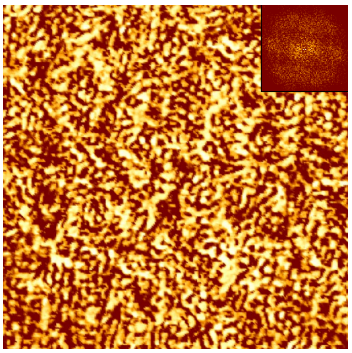

(a) SBS (as-spun) in toluene

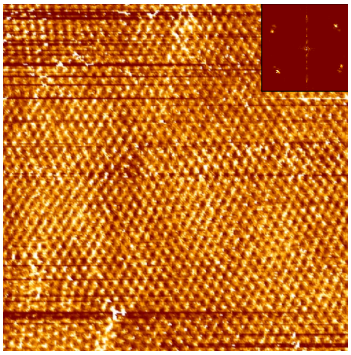

(b) Cyclohexanone vapors - 48 hours

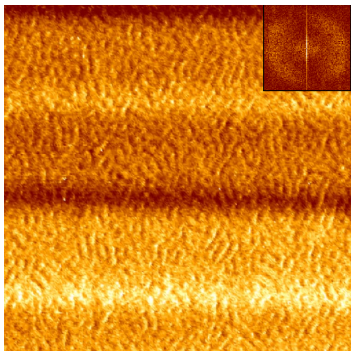

(c) Chloroform vapors - 48 hours

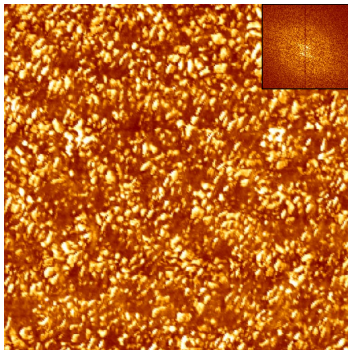

(d) SBS (as-spun) in cyclohexanone

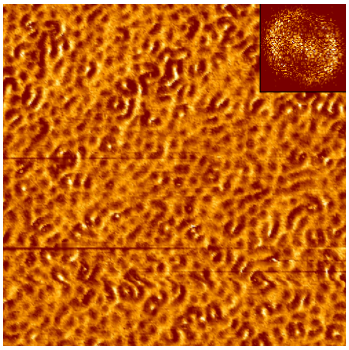

(e) Toluene vapors - 48 hours

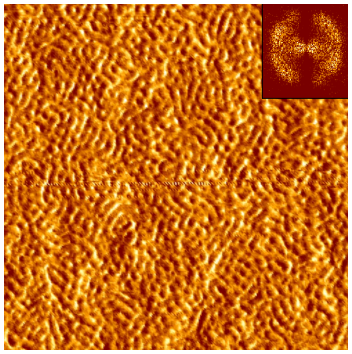

(f) Chloroform vapors - 48 hours

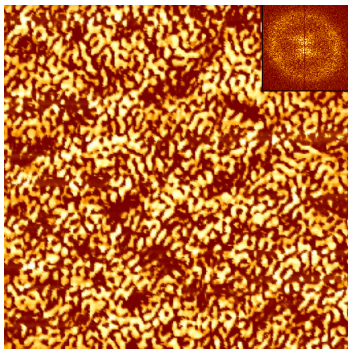

(g) SBS (as-spun) in chloroform

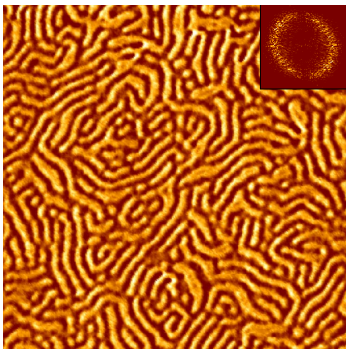

(h) Toluene vapors - 48 hours

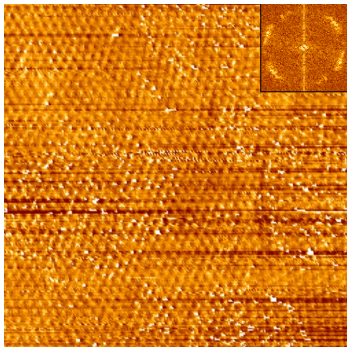

(i) Cyclohexanone vapors - 48 hours

Figure 59: AFM phase images (1.5μ x 1.5μ) showing the effect of different solvent vapors on 260 nm thick SBS-I (4%) film spun cast from toluene

from cyclohexanone (see Figures 59(d) - 59(f)), neither toluene nor chloroform were able to create a long-range order. However, for films spun cast from chloroform (shown in Figures 59(g) - 59(i)), whilst hexagonal ordering in cyclohexanone is consistent with our other results, films annealed in toluene are very different from that seen in other toluene annealed films. In this case, a characteristic cylindrical domain morphology lying parallel to the surface is observed. The difference in this case may in part be due to the slight degree of ordered structure observed in the as-made sample, however the exact mechanism is not clear.

Given these results, we wanted to understand the behavior observed as a function of the solvent quality. Based on the selectivity and the match with the solubility parameter of the PS and PB polymers, eight solvents consisting of toluene, cyclohexanone, dimethoxyethane (DME), ethyl acetate (EAC), chloroform, heptane, diethyl phthalate and cyclohexanol were used to solvent anneal 50 nm thick films[1] spun cast from toluene onto mica substrates. DME is known to be a selective solvent for PB and EAC is a selective solvent for PS [141, 142], whereas toluene and cyclohexanone are relatively good solvents for both PS and PB (see Table 3 in Section 3.2.1 for solvent properties). A representative set of AFM images of the film surfaces after 6 hours of solvent exposure using these solvents is shown in Figure 60.

The as-made film (see Figure 60(a)) as expected shows no defined structure. After annealing in toluene for 6 hours, no improvement in the structure is observed (see Figure 60(b)) as perhaps can be expected based on the results from the thick films. Structurally, the best ordered film surfaces were obtained when solvent annealed in DME (Figure 60(c)), EAC (Figure 60(d)) and chloroform (Figure 60(f)). Films annealed in cyclohexanol and heptane (Figure 60(i) and 60(g)) look even less ordered

[1]Although we got promising results in 260 nm thick film, it was very difficult to image these films using AFM. So, subsequent experiments were performed on 50 nm thick films formed by spin coating substrates with 1% solution of SBS-I in toluene.

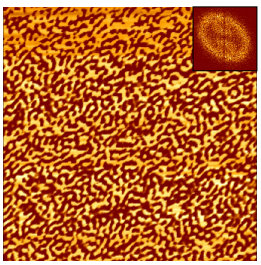

(a) 50 nm thick film - as spun from toluene

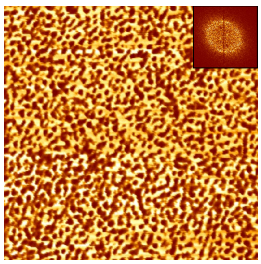

(b) Toluene

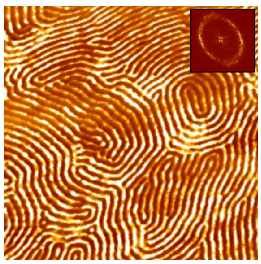

(c) Dimethoxyethane

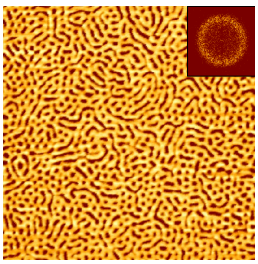

(d) Ethyl acetate

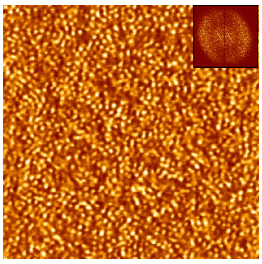

(e) Cyclohexanone

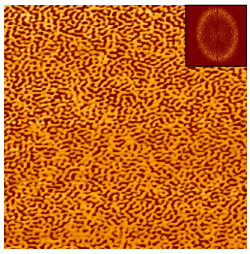

(f) Chloroform

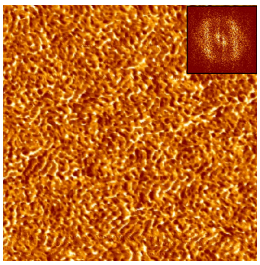

(g) Heptane

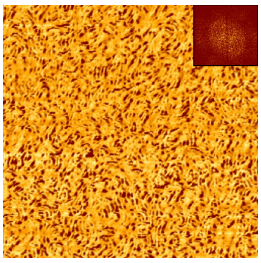

(h) Diethyl phthalate

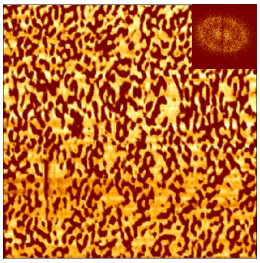

(i) Cyclohexanol

Figure 60: AFM phase images (1.5μ x 1.5μ) of 50 nm thick SBS-I films spun cast from toluene (on mica) after 6 hours of solvent exposure

than the as-made film. For cyclohexanone (Figure 60(e)) and diethyl phthalate (Figure 60(h)), the film surface is more ordered than the as-made film but the film is not as ordered as in the case of DME and EAC.

From Figures 58, 59 and 60, it is evident that there were a lot of conditions and solvents that could be taken up for further studies. Since these represent a very wide range of variables, selective experiments were chosen for a detailed study. 50 nm thick SBS-I films spun cast from toluene were selected for further studies with the most promising solvents - dimethoxyethane, ethyl acetate and cyclohexanone. For surface studies using AFM, DME and EAC were used to determine the effect of these

solvents as a function of annealing time. These solvents were chosen because they are selective to the two different polymers of the SBS-I. For GISAXS experiments, SBS-I films spun cast in toluene onto silicon and solvent annealed in toluene, cyclohexanone, DME and EAC were chosen.

5.1 Solvent annealing effects on mica

Of the eight solvents initially investigated, dimethoxyethane (DME) and ethyl acetate (EAC) were selected for further investigation because they are selective solvents for PB and PS, respectively [141, 142].

The effect of DME vapors on a 50 nm thick SBS-I film is shown as a function of annealing time in Figure 61. The as-made film surface (spun from toluene) had no distinct features, but with just one hour of annealing time, the film showed predominantly hexagonally packed cylinders normal to the substrate as shown in Figure 61(b). These cylinders comprise PS cores surrounded by a PB matrix. In the melt state, based on configuration and molecular weight, we would expect the cylinders to have a PB core and a PS matrix. However, since DME is a selective solvent for PB, the volume of this phase must be swollen compared to PS to give an apparent inverted cylindrical morphology. This kind of inverted morphology has been observed for SBS films with 30% PS weight fraction by Huang and coworkers [91, 92], where the selective solvent for the minority PS block preferentially swells PS domains more than PB to change the effective volume fraction of each domain and hence alter the curvature of the interface. The improvement in the order is also evident by comparison of the respective FFT images where 1 hour annealed sample image shows a distinct halo which is not clearly obvious in the as-made film. With an exposure of 3 hours (see Figure 61(c)), the degree of order improves but the orientation of the cylinders remains normal to the surface. However, whilst locally the cylinders have a high degree of packing, many crystal grains exist, so there is no long-range crystallographic order.

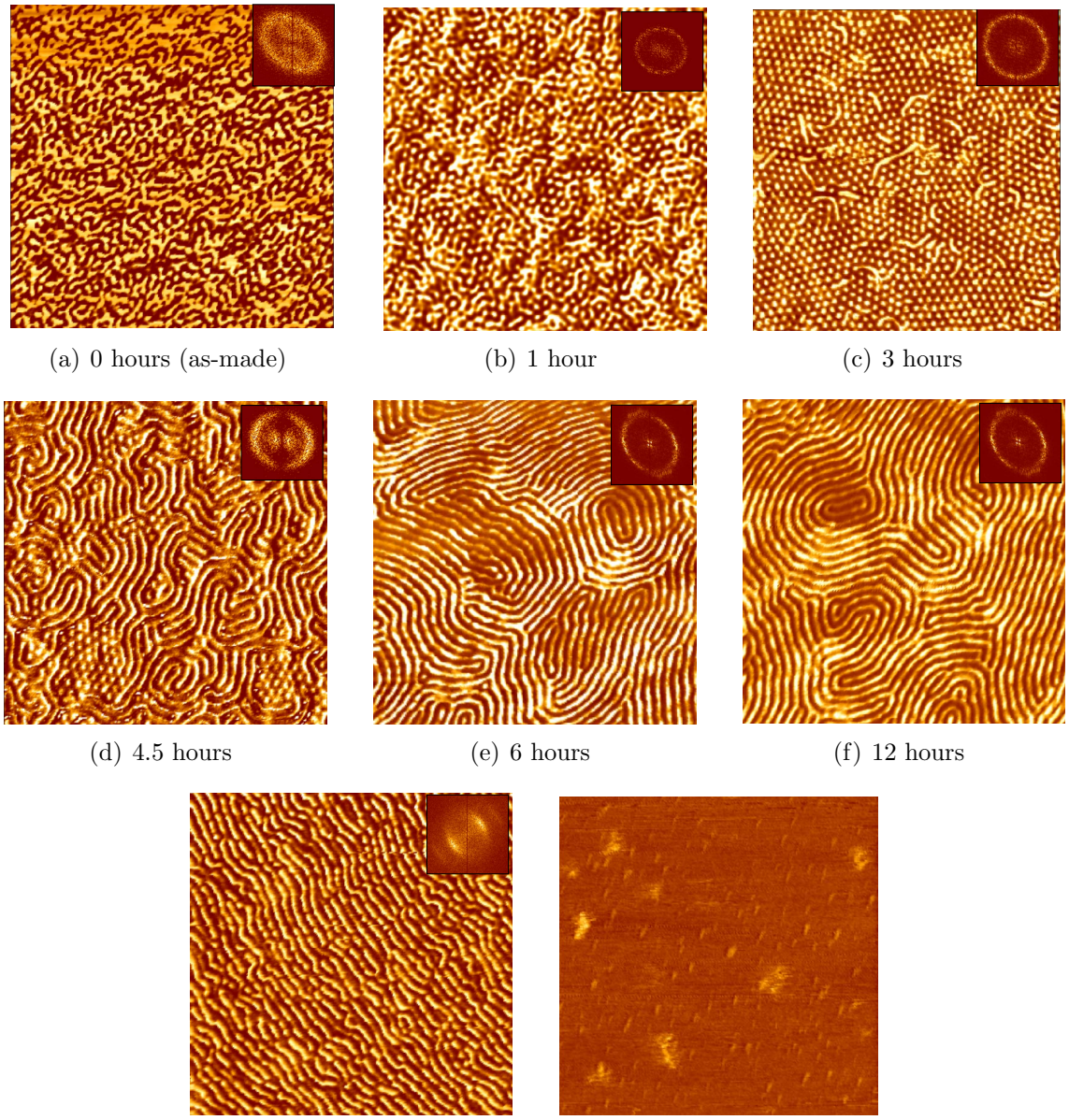

(a) 0 hours (as-made) (b) 1 hour (c) 3 hours

(d) 4.5 hours (e) 6 hours (f) 12 hours

(g) 24 hours (h) 48 hours

Figure 61: AFM phase images (1.5μ x 1.5μ) of 50 nm thick SBS-I films annealed using dimethoxyethane - effect of annealing time

Consequently the FFT is a halo and not a series of 6 spots as seen for the highly ordered system in Figure 58(e). A mixed morphology containing both in-plane and normal aligned cylinders is observed after solvent exposure of 4.5 hours (see Figure 61(d)). With an increase in the solvent exposure time, only ordering parallel to the substrate i.e. in-plane cylinders were observed. These images are characteristic of 'fingerprint' images reported for many cylindrical BCP domains in thin films. After a solvent exposure time of 6 hours (Figure 61(e)), in-plane cylinders do not have a uniform domain spacing throughout the sample. This is not immediately apparent from the FFT due to the distortion of the halo caused by the small sampling size. However in the upper part of the AFM image (Figure 61(e)), the domain spacing is 41 nm compared to an average value of 47 nm in the remainder of the image. After 12 hour annealing time (Figure 61(f)), there is no significant morphological difference compared to the film annealed for 6 hours although the domain spacing of 47 nm is much more uniform than that after 6 hour annealing. Despite extended annealing, there is not much change in the structure, which differs from other systems such as PS-PEO films where extended annealing creates better ordered surfaces [85]. In the current systems, films start to lose their order at prolonged exposure of 24 hours and greater which may be the results of the dewetting of the film surface (see Figure 61(g) and 61(h)).

When annealed in EAC, the development of the surface morphology of SBS-I films as a function of exposure time is shown in Figure 62. Superficially, the same general behavior is observed here as for DME annealed films. The as-made disordered film surface evolved into a morphology with normal alignment of cylinders as shown in Figure 62(b) and 62(c) but with just one hour of annealing time. The cylinders locally show hexagonal packing normal to the substrate, but in this case, the cores of the cylinders are PB in a matrix of PS. This is perhaps not surprising since EAC is a selective solvent for PS, so it swells this phase of the BCP. A hybrid morphology

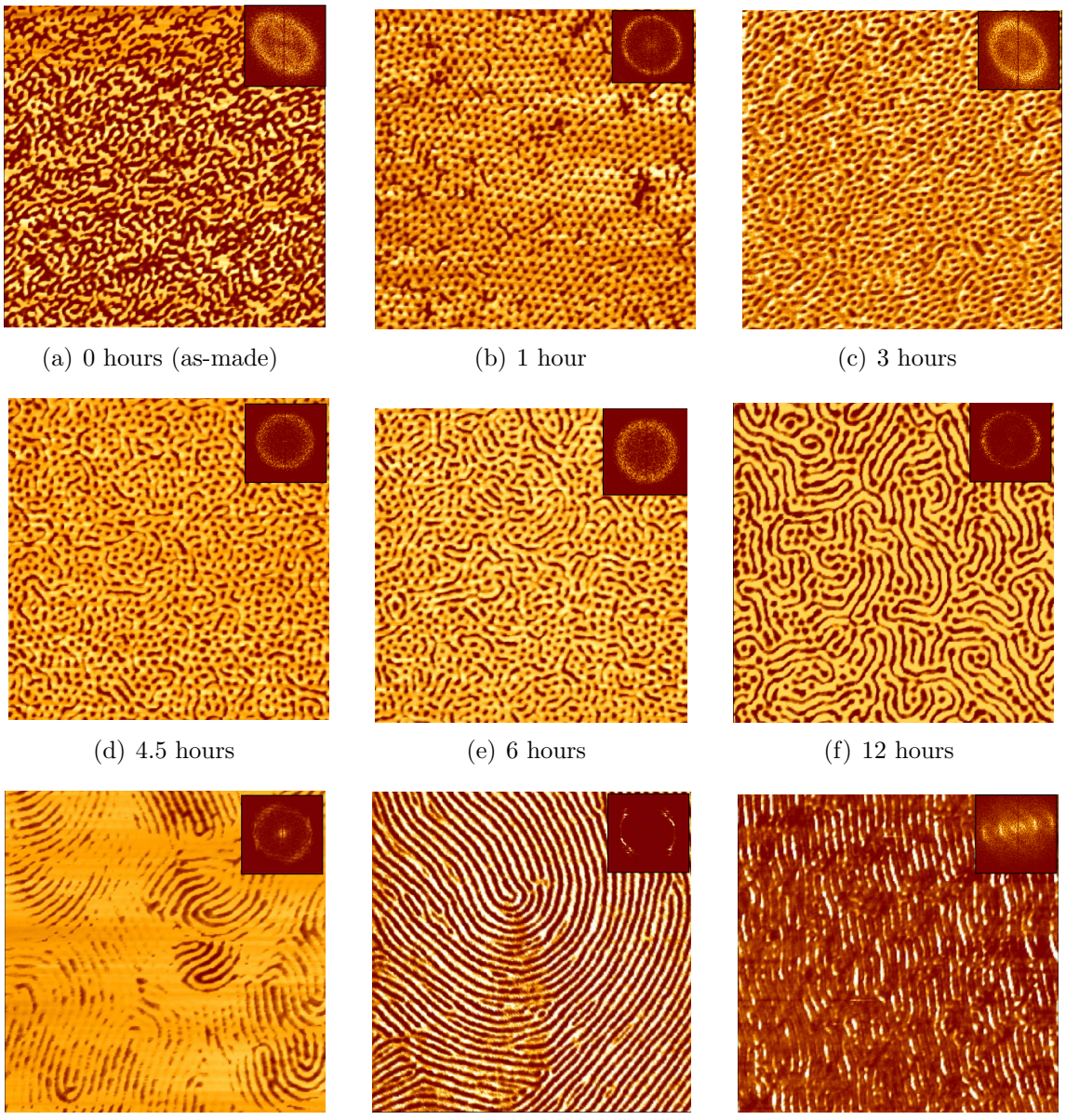

(a) 0 hours (as-made) (b) 1 hour (c) 3 hours

(d) 4.5 hours (e) 6 hours (f) 12 hours

(g) 24 hours (h) 48 hours (i) 7 days

Figure 62: AFM phase micrographs (1.5μ x 1.5μ) of 50 nm thick SBS-I films annealed using ethyl acetate - effect of annealing time

of in-plane and normal cylinders starts appearing after 4.5 hours annealing (Figure 62(d)). This result is very different from the results observed by others [95, 85] where extended annealing caused a greater degree of perpendicular alignment, defect annihilation and consequently long-range order. This structure continues to evolve so that there are more in-plane cylinders than cylinders aligned perpendicularly with increasing annealing times as shown after 6 hours (Figure 60(d)) and 12 hours (Figure 62(f)). With an increase in the solvent exposure time up to 24 hours (Figure 62(g)), all evidence of perpendicular alignment is lost and only ordering parallel to the substrate, i.e. in-plane cylinders, is observed. The contrast between the PS and PB of the underlying cylindrical morphology is not clear in the sample at 12 hours annealing, due to a seemingly large fraction of PS near the surface. However the structure consists of entirely in-plane cylinders. After 48 hours annealing (see Figure 62(h)), the characteristic fingerprint pattern of in-plane cylinders is observed with relatively few defects compared to the structure observed in 12 hours DME annealing (see Figure 61(f)). The average domain spacing in both the 12 hour and 24 hour annealing is 43 nm in both the cases. As with the sample annealed in DME, extended annealing (7 days in this case), leads to dewetting of the film.

Clearly, both DME and EAC undergo similar structural transitions where normal cylinders are observed at smaller solvent exposure times and in-plane cylinders at longer exposure times. This transition takes place with intermediate exposure times where a hybrid morphology is observed. The time scales for these transitions are however very different in the two solvents and this difference in kinetics will be discussed in Section 5.1.1.

To try to understand the ordering mechanism, we have looked at the surface energies of the system. Based on the surface energies of the BCP components, the lower surface energy component should occupy the free surface of the film [157]. Comparing the surface energies of PS ($\gamma_S = 43$ mJ/m^2) and PB ($\gamma_B = 32.5$ mJ/m^2), PB has a

lower surface energy than PS. Thus, the structure should have an equilibrium morphology of in-plane cylinders. However, in the case of annealing in both the DME and EAC, the films initially form non-equilibrium morphology of cylinders normal to the substrate. The formation of normal aligned cylinders is consistent with the results of other groups which also show perpendicular alignment [93]. The thickness of the film (50 nm) is incommensurate with the unperturbed domain sizes equal to 34 nm. The coexistence of parallel and perpendicular morphologies has been experimentally seen in the case of cylinder-forming SBS block copolymers of incommensurate thickness where regions of perpendicular cylinders in a film with predominant in-plane cylinders were seen [87]. For films of incommensurate thickness, these regions were formed in between the terraces exhibiting cylinders with in-plane orientation. Given enough solvent exposure time, the films adopted their thermodynamically stable state of in-plane cylinders.

The variation in alignment direction is clearly dependent on the solvent exposure time. At the shortest solvent exposure times, the microdomain structure is in a metastable state of cylinders normal to the substrate. As annealing continues, solvent content increases giving conditions of relatively high diffusivity of the polymer chains enabling them to adopt their thermodynamically stable state of in-plane cylinders.

5.1.1 Ordering kinetics

From the AFM micrographs, it is clear that whilst the ordering phenomena for DME and EAC are superficially the same, the ordering kinetics are very different, with annealing in EAC much slower than in DME to reach a similar degree of lateral order (which in this case is characterized by in-plane cylinders). In these solvent annealing studies, we did not control the vapor pressure of the solvents within the annealing vessels. Therefore it may be thought that the kinetic effects were a consequence of the inherent differences in vapor pressures between DME and EAC. However the vapor

pressure of DME of 48 mm Hg is considerably lower than that of EAC at 78 mm Hg. Purely based on vapor pressures, we would therefore reasonably expect the BCP ordering kinetics in EAC to be considerably faster than in DME due to the increased solvation at any given time. As observed in Figure 61 and Figure 62, the opposite effect is observed, indicating that the kinetics are not dominated by vapor pressure differences.

An alternative mechanism which does qualitatively explain the kinetics is based on an effective interaction parameter, 'χ_ϵ'. χ_ϵ is used to define the measure of incompatibility between the swollen and unsolvated blocks, which is clearly dependent on the solvent volume fraction in the BCP. χ_ϵ is a function of two parameters: the temperature and the solvent concentration. Since all the films were processed at room temperature, only the solvent volume fraction dependence is considered. The effective interaction parameter can be estimated using Equation 8 [139]:

$$\chi_\epsilon = V_s(\delta_1 - \delta_2)^2/RT \tag{8}$$

where T is the temperature (298 K), V_s is the molar volume of the solvent, and δ_1 is the effective solubility parameter for the polymer solvated with selective solvent. For example in case of DME, δ_1 will represent the effective solubility parameter for PB solvated with DME. δ_2 is the solubility parameter of the other polymer which in the case of DME will be PS. To calculate δ_1 at a given solvation, the following equation is used to determine the effective solubility parameter when polymer and solvent are mixed:

$$\delta_1 = (x)(\delta_{solvent}) + (1-x)(\delta_{polymer}) \tag{9}$$

where x is the solvent volume fraction inside the polymer at a fixed time. The solubility parameter used for PS is 18.6 $(MPa)^{1/2}$, and for PB is 17 $(MPa)^{1/2}$ [139]. For DME, V_s used for DME is 103 cc/mol and for EAC, is 98 cc/mol. Figure 63 shows the interaction parameter as a function of solvent volume fraction (which is

directly related to the annealing time). As can be seen, for DME, the value of χ_ϵ in-

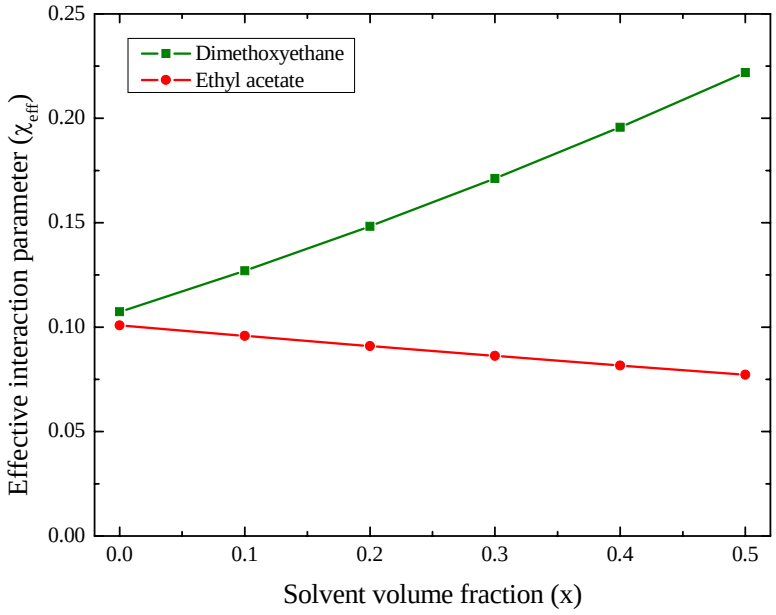

Figure 63: Effective interaction parameter as a function of percent solvent volume

creases with increasing solvent volume fraction, which means that there is an increase incompatibility between the two blocks segregation and consequently a decrease in time to reach an equilibrium state [158]. In the case of EAC, the χ_ϵ decreases with increase in EAC volume fraction and thus there is a slower drive towards equilibrium. Whilst this calculation is rather crude, it does qualitatively explain the observations where the equilibrium state is achieved faster in DME than in EAC.

5.1.2 Degree of order

In order to quantify degree of order in the annealed films, the AFM phase images for the SBS-I were analyzed using a software package specifically designed to determine orientation vectors. This software, called "Orientational Angle Analysis Package" (OAAP), was written and compiled in Igor Pro-6 by Brian Berry at National Institute of Standards and Technology. An appropriate image is loaded in the software, and the contrast improved by a variety of built-in Gaussian filters provided in the software which ultimately reduces the noise in the final output. The filter width (i.e., the

width of the Gaussian function) is set at approximately 1.5 - 4 times the number of pixels in 1 domain spacing (L_o) where 1 pixel = 4.9 nm. An example of the AFM phase image of a SBS-I film annealed in EAC for 1 hour is shown together with the enhanced image after applying the filters in Figure 64. From these filtered

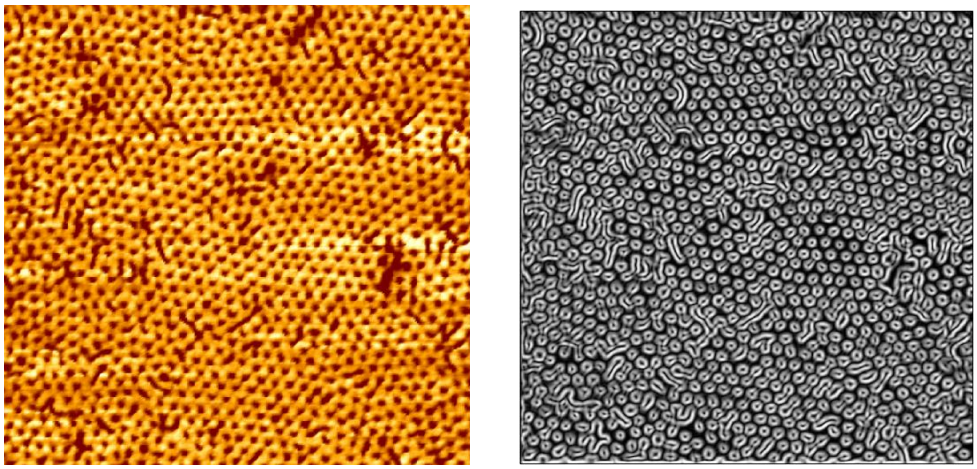

(a) Ethyl acetate - 1 hour AFM image (b) Image after contrast enhancement

Figure 64: Filtering process of a 1.5μ x 1.5μ AFM image used for the degree of order analysis

images, the program generates a false color image of the director angle at each pixel i.e. the local domain orientation within the image. The resulting image is a color map which uses isochromatic shading to show domains which are either oriented in the same direction, or crystallographically in the same plane. A sample with grains having random distribution of directions will appear multi-colored whereas a film with better order will appear with larger areas of the same color. In addition, an increase in the grain size is an indication of the reduction in the defect density. A representative set of images showing the degree of order in the films as a function of annealing times are shown in Figure 65. These data are taken from the AFM images in Figures 61 and 62. As expected, the film annealed in EAC for 48 hours (Figure 65(a)) shows large grains with few defects compared to similar in-plane structures formed by DME (Figure 65(b)). This shows the effectiveness of the solvent annealing

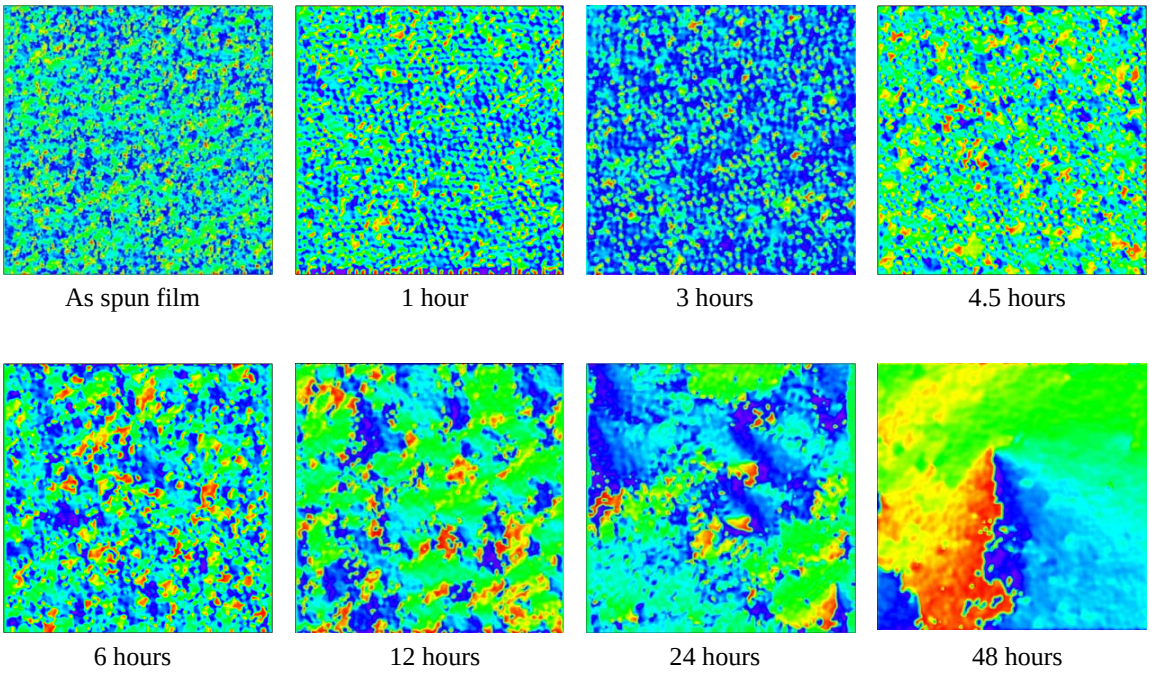

(a) Ethyl acetate

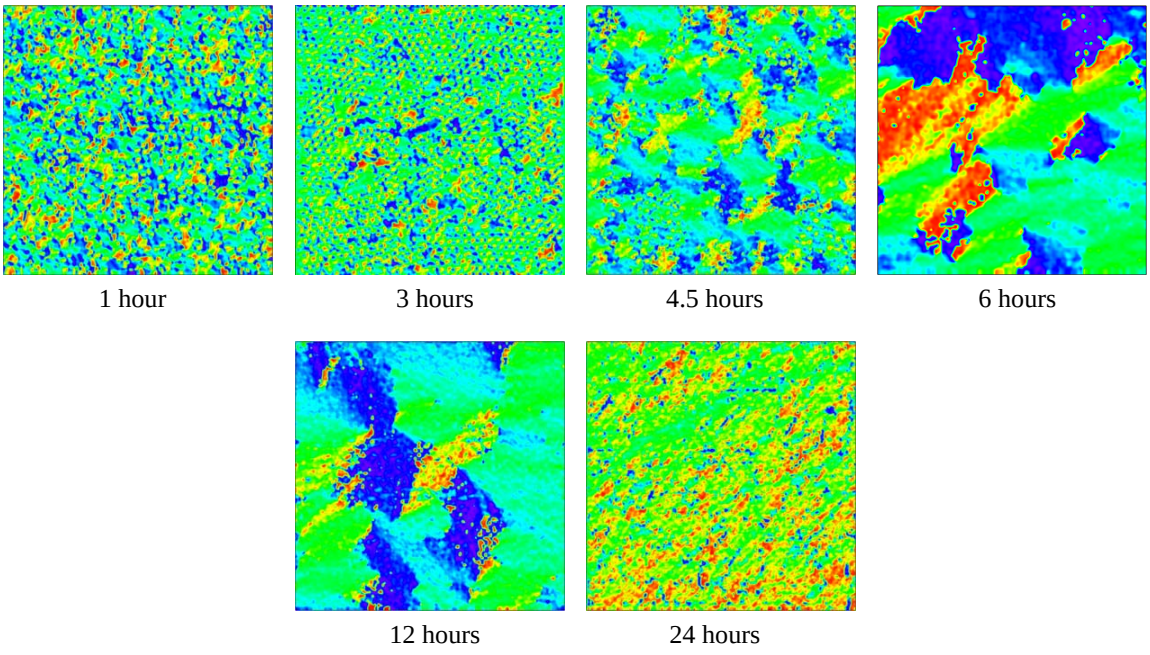

(b) Dimethoxyethane

Figure 65: False color maps calculated using OAAP software of the degree of lateral order in 50 nm thick SBS-I films annealed using EAC and DME solvent vapors. The AFM images used for the analysis are all 1.5μ x 1.5μ

process in developing order in the SBS-I films.

The OAAP program not only generates qualitative visual determination of degree of order, it also generates an order parameter, ξ, which varies between 1 (for perfect alignment) to 0 (for no net orientation of the structure). This value, ξ is determined by the following equation:

$$\xi = \sum_{n} \frac{\text{number of pixels with angle (n)}}{\text{total number of pixels}} \tag{10}$$

The order parameter values for the time dependent solvent annealing in 50 nm thick SBS-I films are given in Table 8.

Table 8: Order parameter determined from the orientation analysis of the AFM images of SBS-I 50 nm thick films annealed in DME and EAC vapors

Exposure time (hrs)	DME	EAC
0	0.40	0.40
1	0.70	0.77
3	0.81	0.66
4.5	0.68	0.69
6	0.72	0.64
12	0.82	0.68
24	0.89	0.74
48	N/A[2]	0.75

From these values, the effectiveness of the solvent annealing process is evident from the significantly higher ξ values in solvent annealed system as compared to the as-made film which has ξ of 0.40. It can be seen that the best ordered state for DME annealing occurs after 12 hours with an order parameter value, $\xi = 0.82$ although the film annealed for 24 hours shows a higher value, it is not a representative AFM image since most of the regions in the film were starting to dewet. This image was just chosen to show the structure in the film portions which were still intact. The best ordered system for EAC is a film exposed for 48 hours with a $\xi = 0.75$. For films with a coexistence of parallel and perpendicular cylinders (4.5 hours for DME

[2]At 48 hours annealing in DME, the sample has dewetted. So, no value of ξ can be obtained.

and 4.5 - 12 hours for EAC), the structure is transitioning from a perpendicular to in-plane cylinders and thus, the values ξ obtained in these cases are lower than when ordering occurs solely in the in-plane and perpendicular directions. By comparing ξ values for these films, solvent annealing using DME seems to be more effective than EAC annealing although a more extensive set of images covering much larger areas needs to be analyzed fully to qualify this statement.

5.2 Solvent annealing effects on Silicon wafer

Following the AFM studies on mica, the effect of changing the substrate surface energy was studied using silicon (Si) as the substrate. To provide valuable through film thickness information, GISAXS measurements were performed on 50 nm and 260 nm thick SBS-I films spun cast from toluene and solvent annealed in toluene, cyclohexanone, DME and EAC. It should be noted that we have yet to be able to perform similar GISAXS experiments on mica substrates due to the inherent long-range 'roughness' of mica compared to Si which greatly affects the scattering behavior. However, using Si substrates, GISAXS measurements were performed on 50 nm thick films annealed for 1, 2, 3, 4, 6, 12, 24, 48 and 168 (7 days) hours. Due to the constraint in beamtime available for the GISAXS experiments at CHESS, exposure times chosen for 260 nm thick films were limited to 6, 12, 24, 48 and 168 hours annealing. The GISAXS data was measured with incidence angles ranging from 0.05 to 0.25^0. The results from these experiments are be discussed in the following sections.

5.2.1 GISAXS Data Analysis

GISAXS measurements yield 2D scattering plots, a typical example of which is shown in Figure 66 for a 50 nm thick SBS-I film annealed in EAC for 18 hours. Figure 66(a) shows the 2D GISAXS scattering pattern which has information in both the Q_y and Q_z directions, where Q_y and Q_z represent the in-plane and normal components of the scattering vector, respectively. The data from the specular reflected beam is not

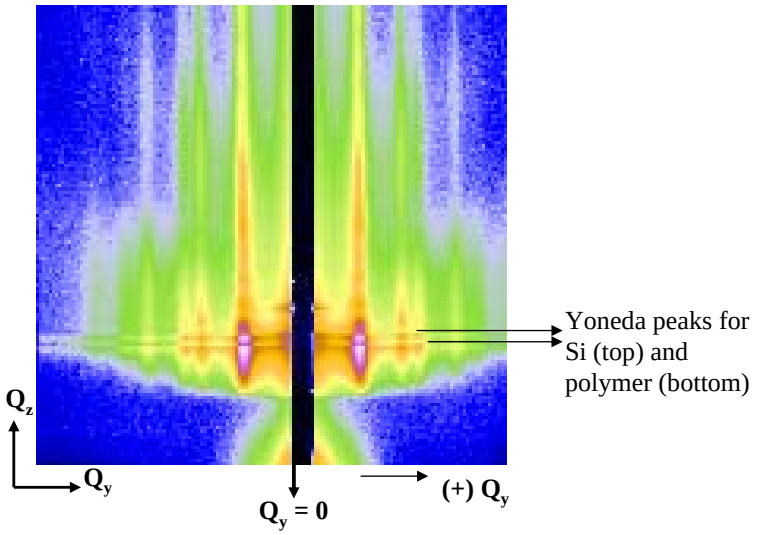

(a) 2D GISAXS pattern

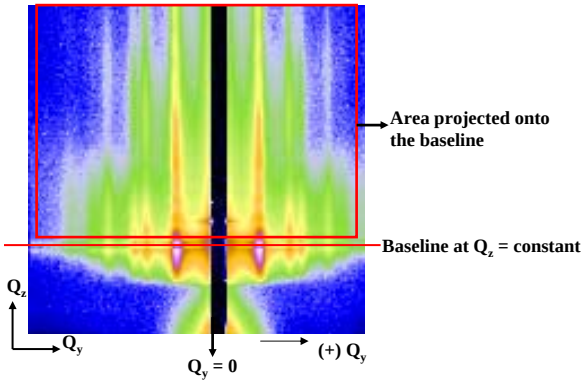

(b) 2D GISAXS for horizontal profile

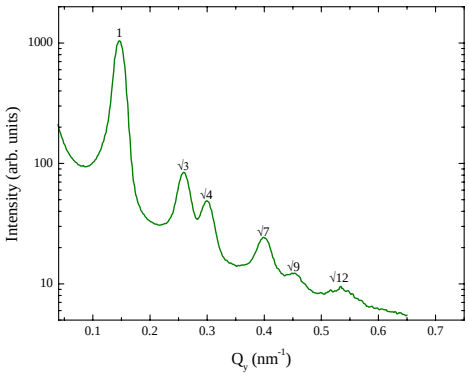

(c) Horizontal profile

Figure 66: 2D GISAXS scattering profiles for SBS-I (50 nm) films annealed in EAC for 18 hours

collected in the GISAXS pattern, since it is too intense for the detector and had to be blocked with a rodlike beamstop (which shows up as a black vertical region centered around $Q_y = 0$). A characteristic pattern of correlation peaks (vertical rods) perpendicular to the substrate can be clearly seen. These are a signature of perpendicular alignment in the film.

To analyze the lateral structure of the film, an integrated intensity projection is made along the Q_y axis. Figure 66(b) displays the 1D horizontal profile which is obtained by projecting the intensity of the peaks in Q_y to a constant Q_z value. This plot is symmetric about $Q_y = 0$, but we only plot for $Q_y \geq 0$. A typical plot of the intensity as a function of Q_y is shown in Figure 66(c). The multiple orders of Bragg peaks are clearly observed (which are labeled 1,2 and so on). In this particular case, the first or primary peak (labeled 1) is obtained at $Q_{y(1)} = 0.146$ nm^{-1} which gives a domain spacing of 43 nm (calculated from domain spacing $= 2\pi/Q_y$) which is greater than the bulk value of 34 nm. The second order peak can be observed at $Q_y = 0.253$ nm^{-1} which is (approximately) equal to $\sqrt{3}Q_{y(1)}$. Other peaks are also clearly observed at relative positions of $\sqrt{4}$, $\sqrt{7}$, $\sqrt{9}$, $\sqrt{12}$ times $Q_{y(1)}$. These peak positions are characteristic of hexagonally ordered morphology. Thus, from the horizontal profile we can obtain information about the morphology and domain spacing of the film structure.

5.2.2 Morphology of SBS-I films

In stark contrast to the behavior on mica substrates, it will become clear from the next few sections that the SBS-I films on silicon wafers always form cylinders perpendicular to the substrate regardless of the film thickness, solvent used for annealing or annealing time. An example of this orientation for a 50 nm thick SBS-I film is shown in the AFM phase image (Figure 67) which has been annealed in DME for 6 hours. This particular area on the film has large number of defects that are clearly visible.

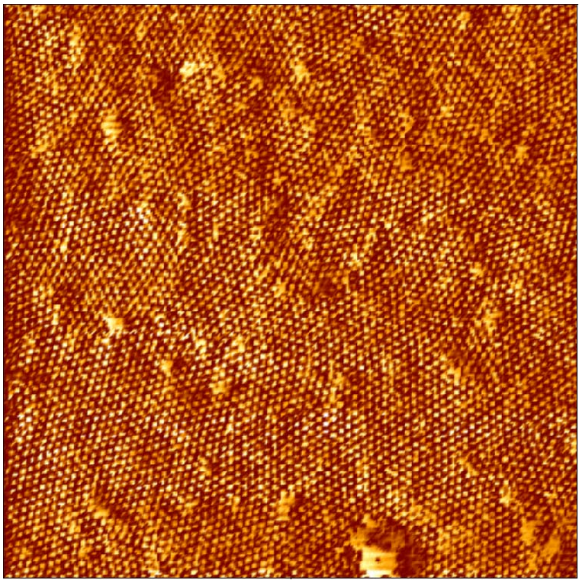

Figure 67: 3μ x 3 μ AFM phase micrographs of SBS-I (50 nm) film after DME-6 hour annealing on silicon substrate

The degree of order of this film is measured using the OAAP program described in Section (5.1.2). Figure 68 shows the false color map obtained for this film. The order parameter, ξ calculated using this image is found to be 0.61 which is low when compared to the films formed on mica which were annealed in DME for the same time (6 hours).

To explain this morphology of cylinders aligned normal to the surface, we compare to the surface energies (γ) between the substrate and the polymer blocks. Since we treated the silicon wafers, the relevant surface energies for the system are , γ_{SiOx} = 68 mJ/m^2 for piranha treated Si wafer, $\gamma_S = 43$ mJ/m^2 for PS, and $\gamma_B = 32.5$ mJ/m^2 for PB. Since the surface energy of the PB is the lowest, there would normally be a driving force for the PB phases to preferentially segregate to the air. However, in all cases, the film contains cylinders which are aligned normal to the surface with no evidence of a PB surface segregated layer. Comparing the surface energies, there is only a slight preference of Si to PS but both the polymers will wet the surface. The slight preference for PS may not be providing enough driving force for the cylinders to

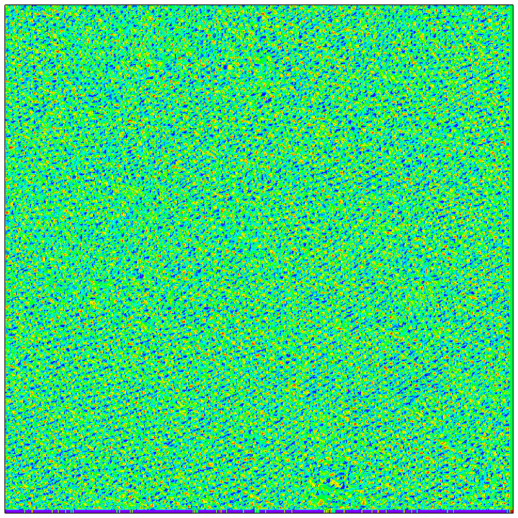

Figure 68: False color map for a 3μ x 3 μ AFM phase micrographs of 50 nm thick film on silicon substrate.

orient in-plane and thus, the Si wafer may be acting effectively as a neutral substrate for both PS and PB.

In addition, it should be remembered that the film thickness (50 nm) is incommensurate with respect to the unperturbed domain spacing. In work by Lambooy et al. [159], this incommensurate thickness has been proposed as the driving force for perpendicular alignment, and thus, could partly be the reason for the orientation observed here. However, the incommensurate thickness effects can not be solely responsible given the reorientation observed in films on mica.

5.2.3 Effect of solvent exposure time

The effect of solvent exposure time are discussed separately for each solvent. Not all but representative 2D patterns are shown in the following sections and all GISAXS results discussed are obtained at an incident angle of 0.25^0 unless otherwise stated. This angle is used since the penetration depth of the X-ray beam at this angle provides a near full depth characterization of the film surface.

5.2.3.1 Films annealed in toluene

GISAXS scattering profiles of SBS-I (50 nm and 260 nm) films when annealed in toluene are shown in Figures 69 and 70. Figure 69(a) shows the 2D GISAXS patterns of the 50 nm thick film as the annealing time is increased with the corresponding Q_y integrated plots shown in Figure 69(b). For the as-made film, there is no order in the film as no distinct pattern or features are seen in the 2D pattern. On annealing in toluene for 3 hours, the GISAXS pattern shows ridges of intensity at $Q_{y(1)} = \pm 0.142$ nm^{-1} giving a domain spacing of $2\pi/Q_y = 44$ nm which extend vertically in Q_z. These scattering patterns are consistent with the structural alignment perpendicular to the surface. Although a weak maxima at $Q_y = \pm 0.275$ nm^{-1} exists, the lack of high order clearly demonstrates the lack of long-range order in the sample. Some improvement in order occurs after 6 hours annealing as shown by the reduction in the FWHM of the $Q_y = \pm 0.15$ nm^{-1} peak although higher order peaks are absent indicating a lack of crystallographic ordering.

In the case of the 260 nm thick film, the best order was achieved after 6 hours of annealing giving the 2D pattern shown in Figure 70(a). This structure is more ordered than the best ordered 50 nm thick films which is obvious from the definition in Bragg peaks seen in the GISAXS patterns. This is confirmed by analyzing the 1D horizontal profiles, some of which are shown in Figure 70(b) because in addition to the primary peak at $Q_{y(1)} = 0.138$, there are 2 higher order peaks at $Q_y = 0.276$, 0.421 nm^{-1} equivalent to $2Q_{y(1)}$, $3Q_{y(1)}$, which are characteristic of a lamellar morphology. This is an unexpected result since a hexagonal morphology of SBS-I observed in the bulk state (see 4.1.1.1). In addition, there is a broad peak (shoulder) in the vicinity of the primary peak at $Q_y = 0.162$ nm^{-1} equivalent to $1.17Q_{y(1)}$. These relative positions of (1.17, 2 and 3)$Q_{y(1)}$ of these higher order peaks does not seem to follow the series of diffraction patterns for commonly observed morphologies.

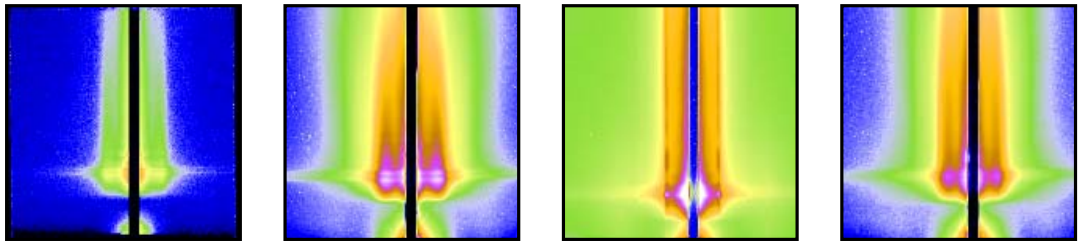

(a) 2D GISAXS patterns - The best ordering is achieved after 6 hours annealing

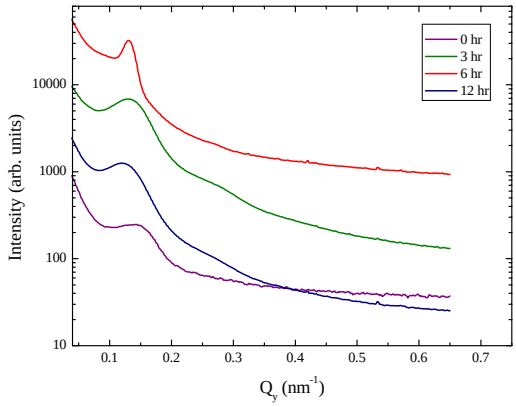

(b) 1D horizontal profile (along Q_y) of different exposure times on 50 nm thick film.

Figure 69: GISAXS scattering profiles for 50 nm thick SBS-I films annealed in toluene - effect of solvent exposure time

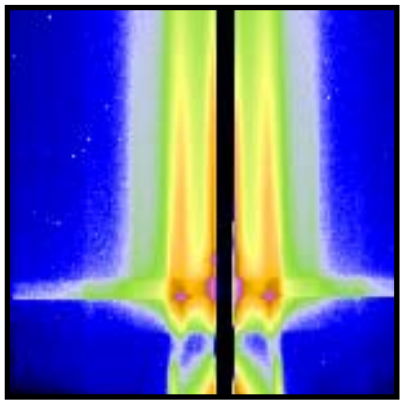

(a) 2D GISAXS pattern for the best ordered state (6 hours).

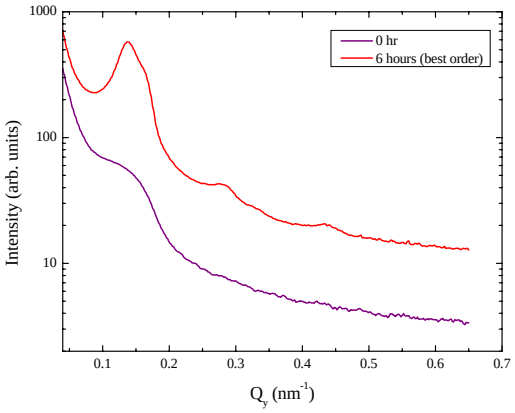

(b) 1D horizontal profile of the best ordered state (6 hours - shown in Fig70(a)).

Figure 70: GISAXS scattering profiles for 260 nm thick SBS-I films annealed in toluene - effect of solvent exposure time

5.2.3.2 Films annealed in dimethoxyethane (DME)

GISAXS data and their analysis for SBS-I films annealed in DME are presented in Figures 71 and 72. The 2D GISAXS scattering profiles obtained for a 50 nm thick SBS-I film annealed in DME are shown in Figure 69(a) as a function of annealing time.

Even after just 1 hour annealing, well defined Bragg peaks running vertically on either side of the specular ridge are clearly visible. This scattering is consistent with the alignment of the structure perpendicular to the surface. As the annealing time in DME increases, the structure improves as shown by the increasing number of Bragg peaks visible in the 2D patterns. The most ordered state is obtained at 6 hours after which the intensity of the peaks starts decreasing, as seen in the sample annealed for 18 hours. The integrated intensity of these GISAXS patterns is analyzed for 1D Q_y profiles as shown in Figure 71(b). The as-made film (see Section 5.2.3.2) just shows a single peak at $Q_y = 0.142$ nm^{-1}. By exposing the film to DME vapors, higher order peaks are also obtained where the number and the intensity of these peaks increases as the annealing time increases, indicating improvement in both local and long-range order. For 6 hours exposure time, the primary peak ($Q_{y(1)}$) is observed at 0.158 nm^{-1} which is equivalent to a domain spacing of 39.7 nm. The second order peak can be seen at $Q_y = 0.276$ nm^{-1} which is approximately equal to $\sqrt{3}Q_{y(1)}$. Other peaks occur at $Q_y = 0.321$, 0.426, 0.471 and 0.547 nm^{-1} equivalent to $\sqrt{4}Q_{y(1)}$, $\sqrt{7}Q_{y(1)}$, $\sqrt{9}Q_{y(1)}$, $\sqrt{12}Q_{y(1)}$. These peaks are characteristic of hexagonal morphology consistent with cylindrical BCP domain microphase structures, which in this case are aligned perpendicular to the substrate. There results therefore confirm the AFM measurements shown in Figure 67.

The reduction in order after 6 hours of annealing is clearly seen in the case of 18 hour annealing where the sharpness and the intensity of the Bragg peaks is reduced compared to 6 hour annealed samples. The domain spacings determined from the

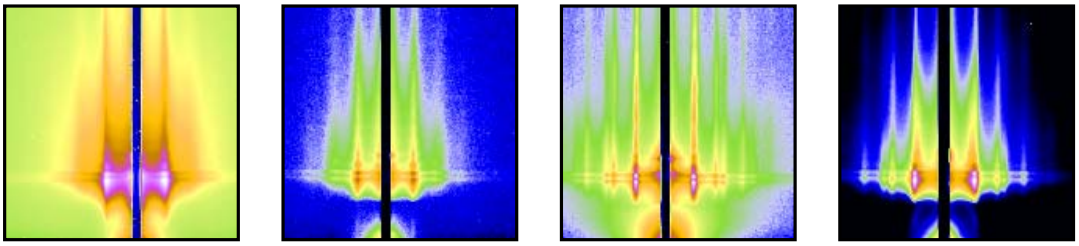

(a) 2D GISAXS patterns - the best ordering is observed after 6 hours annealing

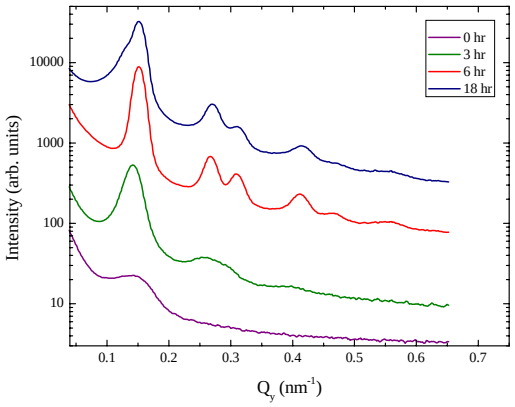

(b) 1D horizontal profile (along Q_y) of different exposure times

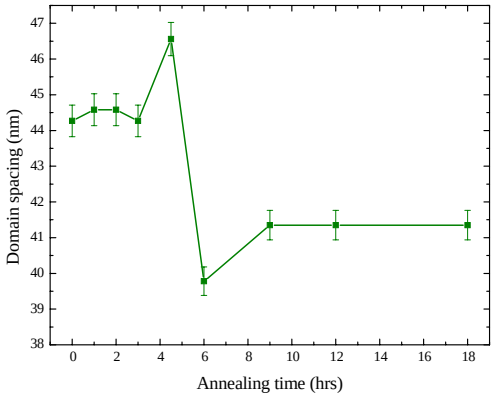

(c) Domain spacing as a function of annealing time for SBS-I (50 nm) film

Figure 71: GISAXS scattering profiles for 50 nm thick SBS-I films annealed in DME - effect of solvent exposure time

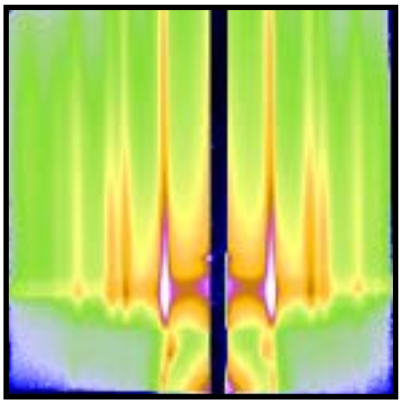

(a) 2D GISAXS pattern for the best ordered state (24 hours)

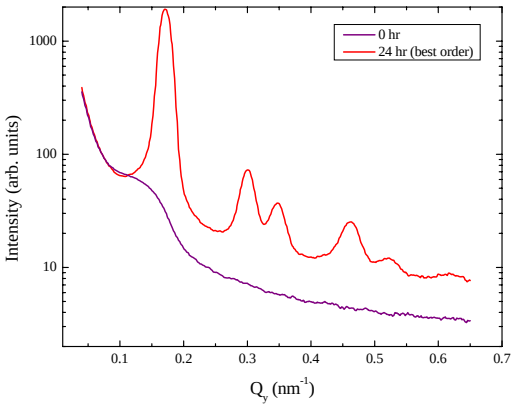

(b) 1D horizontal profile of the best ordered state (24 hours - shown in Fig72(a))

Figure 72: GISAXS scattering profiles for 260 nm thick SBS-I films annealed in DME - effect of solvent exposure time

$Q_{y(1)}$ peak positions as a function of annealing time are shown in Figure 71(c). Interestingly, the sample with the best ordered state (6 hours) has the smallest domain size. For annealing times above and below 6 hours, the domain spacing is larger. This minimum domain spacing that occurs at 6 hours indicates that the structure has attained its best ordered state.

For 260 nm thick films, the ordering behavior of the system is superficially the same as that for the 50 nm thick films although the ordering kinetics are slower. A representative 2D GISAXS pattern for the most ordered sample, which occurs after 24 hour annealing is shown in Figure 72(a). The 1D Q_y plot from the sample annealed for 24 hours is compared to the as-made film in Figure 72(b) which shows a significantly greater degree of order in the structure in the annealed film. For the 24 hour annealed sample, the primary peak was obtained at $Q_{y(1)} = 0.171$ nm^{-1} giving a domain spacing of 36.7 nm, which is smaller than the lower value attained by the 60 nm thick film . Other higher order peaks were observed at $Q_y = 0.301$, 0.347, 0.463 and 0.522 nm^{-1} which are approximately equal to $\sqrt{3}Q_{y(1)}$, $\sqrt{4}Q_{y(1)}$, $\sqrt{7}Q_{y(1)}$, $\sqrt{9}Q_{y(1)}$ and $\sqrt{12}Q_{y(1)}$ respectively, consistent with a hexagonal morphology.

The 24 hours of annealing to achieve the best ordered structure in the 260 nm thick film is much longer time than the 6 hours of annealing needed for the 50 nm thick film to attain the same degree of order. Assuming a constant vapor diffusion rate, through the film, the ratio in film thickness would mean that the 260 nm thick film should take approximately 5 times longer to reach its lowest energy morphology. Compared to the 50 nm film, in this case the annealing time is 30 hours for 260 nm thick films, which is consistent with our experimental results.

5.2.3.3 Films annealed in ethyl acetate (EAC)

GISAXS patterns and their analysis for 50 nm and 260 nm thick SBS-I films annealed in EAC are presented in Figures 73 and 74.

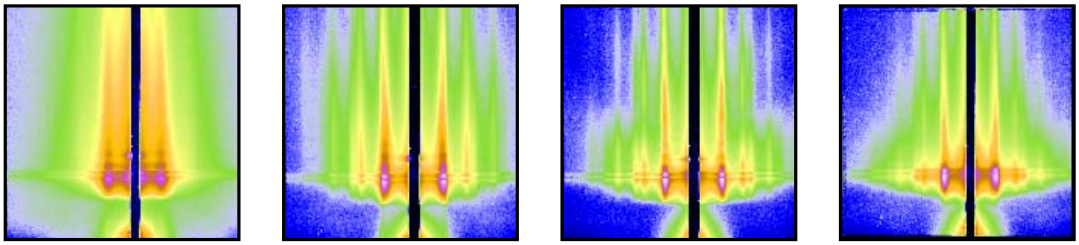

(a) 2D GISAXS patterns for a 50 nm thick film - The best ordered system occurs after 18 hours

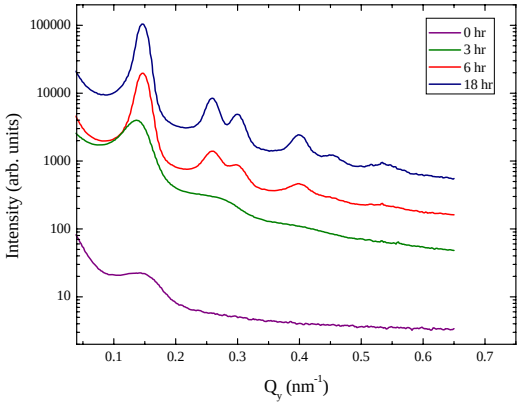

(b) 1D horizontal profile (along Q_y) of different exposure times on 50 nm thick film

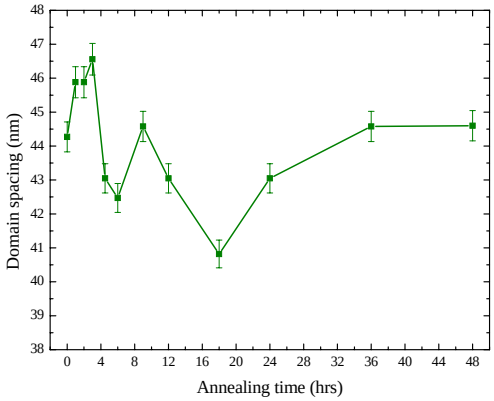

(c) Domain spacing as a function of annealing time for SBS-I (50 nm) film

Figure 73: GISAXS scattering profiles for 50 nm thick SBS-I films annealed in EAC - effect of solvent exposure time

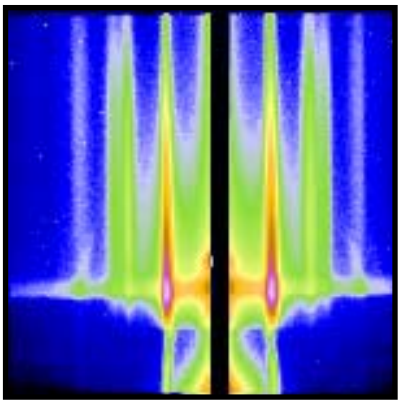

(a) 2D GISAXS pattern for the best ordered state (24 hours) for 260 nm thick film

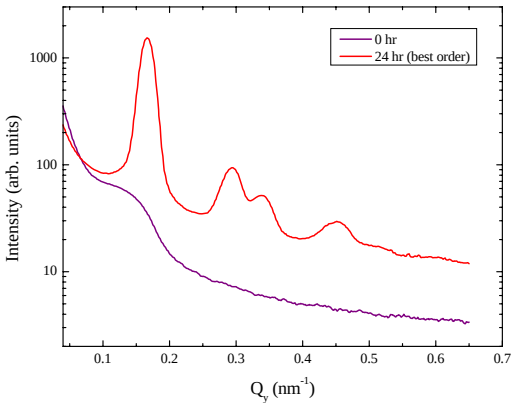

(b) 1D horizontal profile of the best ordered state (24 hours - shown in Fig74(a))

Figure 74: GISAXS scattering profiles for 260 nm thick SBS-I films annealed in EAC - effect of solvent exposure time

From the 2D plots for the 50 nm thick film shown in Figure 73(a), it can be seen from the vertical Bragg peaks that film is ordering normal to the substrate and that the order is improving as the annealing time increases. However, after 18 hours, the film starts to lose this high degree of order (see 24 hour annealed sample). 1D integrated Q_y plots of these 2D patterns are shown in Figure 73(b). The improvement in the order of the films is evident from the increase in the number of higher order peaks as the annealing time increases. The most number of peaks are observed for 18 hour annealing time for which the primary peak is seen at $Q_y = 0.154$ nm^{-1} equivalent to a domain spacing of 40.8 nm. This is followed by the second order peak at $Q_y = 0.267$ nm^{-1} which is approximately equal to $\sqrt{3}Q_{y(1)}$. Other peaks occur at $Q_y = 0.309$, 0.407, 0.462 and 0.525 nm^{-1} equivalent to $\sqrt{4}Q_{y(1)}$, $\sqrt{7}Q_{y(1)}$, $\sqrt{9}Q_{y(1)}$, $\sqrt{12}Q_{y(1)}$. These peaks are again characteristic of a hexagonal morphology. The domain spacing as a function of the annealing time is shown in Figure 73(c), and as before follows the pattern of ordering disordering that leads to a decrease and then increase in the domain spacing. At the minimum domain spacing of 40.8 nm after 18 hour annealing, the system has attained its best ordered state.

For the 260 nm thick films, it takes longer to reach the most ordered state as revealed by the 1D $Q_{y(1)}$ plots (Figure 74(b)) and 2D GISAXS patterns (Figure 74(a)) with the most ordered state occurring after 24 hours annealing. Significant improvement in the order of the film is observed up to 24 hours annealing as the higher order peaks are become more visible. For the 24 hour annealed samples (see Figure 74), the primary peak is observed at $Q_{y(1)} = 0.166$ nm^{-1} which corresponds to a domain spacing of 36.9 nm. All the higher order peaks are observed at equivalent positions of $\sqrt{3}Q_{y(1)}$, $\sqrt{4}Q_{y(1)}$, $\sqrt{7}Q_{y(1)}$ which are characteristic of a hexagonal morphology.

This observation of the most ordered state for the 260 nm thick film occurring after 24 hours is perhaps a little surprising. Based purely on thickness arguments we would perhaps expect the most ordered state to occur after about 94 hours[3].

Clearly ordering occurs much faster in this case although the extra driving force for this solvent is not clear. Part of this may be associated with EAC being a selective solvent for PS which makes up the majority of the BCP volume fraction. In this case, it is easier for EAC to penetrate through the thickness of the film compared to DME since PS would in this case be expected to form the continuous matrix.

5.2.3.4 Films annealed in Cyclohexanone

GISAXS patterns and their analysis for SBS-I films annealed in cyclohexanone are presented in Figures 75 for 50 nm thick films and Figure 75 for 260 nm thick films.

A representative series of 2D GISAXS scattering profiles for a 50 nm thick SBS-I film annealed in cyclohexanone are shown in Figure 75(a). As the film is annealed in cyclohexanone vapors, the perpendicularly aligned order in the film improves which is evident from the increasing number of Bragg peaks visible in the 2D patterns.The most ordered state is obtained at 24 hours which shows remarkable order normal to the substrate. For annealing times larger than 24 hours, the intensity of the peaks decrease as shown for the film annealed for 48 hours indicating a reduction in the degree of order.

The intensity distribution of these GISAXS patterns is analyzed along the Q_y direction for 1D horizontal profiles as shown in Figure 75(b). The as-made film only shows the primary peak at $Q_y = 0.142$ nm^{-1}. On exposure of the film to the cyclohexanone vapors, the development of multiple higher order peaks as seen in the 2D patterns are clearly observed. For the film with maximum order (24 hours), the primary peak ($Q_{y(1)}$) is observed at 0.158 nm^{-1} which is equivalent to a domain spacing of 39.7 nm. The second order peak can be seen at $Q_y = 0.278$ nm^{-1} which is approximately equal to $\sqrt{3}Q_{y(1)}$. Other peaks occur at $Q_y = 0.321$, 0.425, 0.480 and 0.552 nm^{-1} equivalent to $\sqrt{4}Q_{y(1)}$, $\sqrt{7}Q_{y(1)}$, $\sqrt{9}Q_{y(1)}$, $\sqrt{12}Q_{y(1)}$. These peaks, as

[3]The best ordered state for 50 nm is achieved after 18 hours of annealing. So, for the 260 nm thick film, the time taken to obtain the best ordered state is (260/50) x 18 $\sim$ 94 hours.

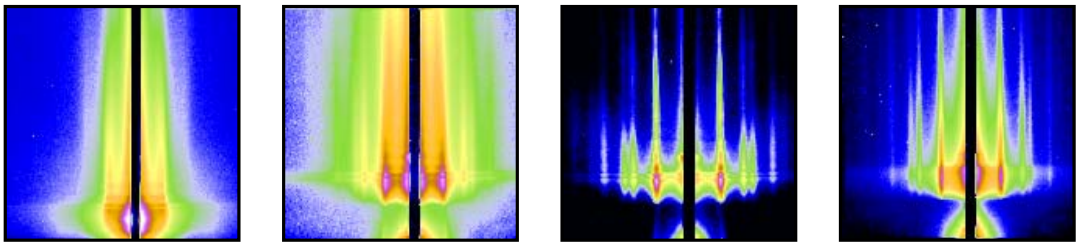

(a) 2D GISAXS patterns for a 50 nm thick film - best ordered state achieved after 24 hours annealing

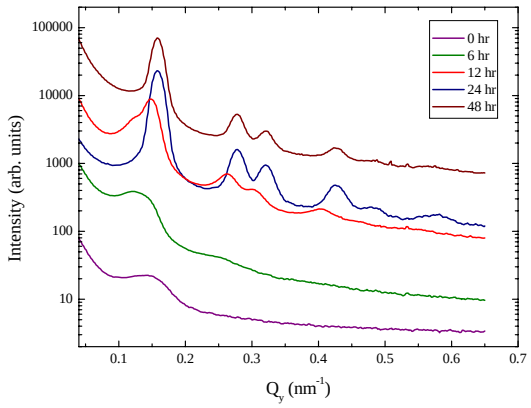

(b) 1D horizontal profile (along Q_y) of different exposure times

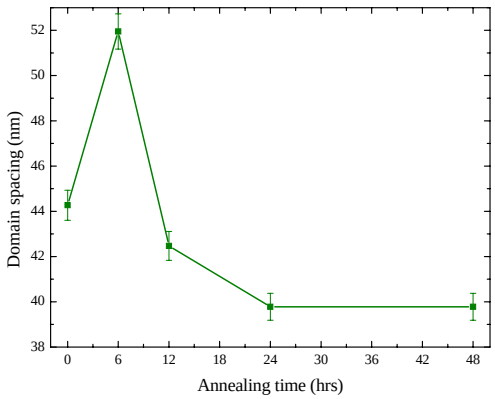

(c) Domain spacing as a function of annealing time

Figure 75: GISAXS scattering profiles for 50 nm thick SBS-I films annealed in cyclohexanone - effect of solvent exposure time

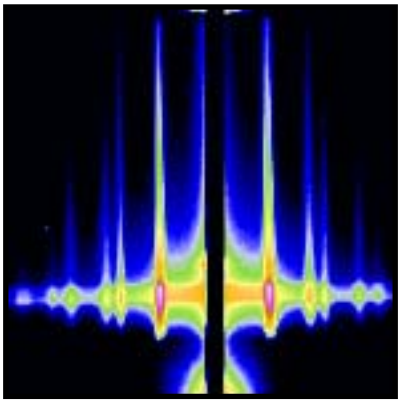

(a) 2D GISAXS pattern for the best ordered state (168 hours)

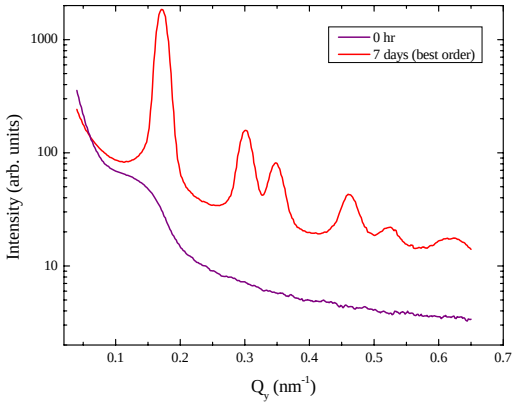

(b) 1D horizontal profile of the best ordered state (168 hours - shown in Fig76(a))

Figure 76: GISAXS scattering profiles for 260 nm thick SBS-I films annealed in cyclohexanone - effect of solvent exposure time

seen for other samples, are characteristic of a hexagonal morphology. The domain spacing as a function of the annealing time is shown in Figure 75(c). As seen for other systems, the best ordered state (24 hours) has the smallest domain spacing, and for annealing times larger and smaller than 24 hours, the domain spacing is larger.

For the 260 nm thick film, by evaluation of the 2D GISAXS patterns (Figure 76(a)) and 1D integrated $Q_{y)}$ plots (Figure 76(b)), it is obvious that perpendicular alignment to the surface occurs. As before, ordering improves with the annealing time with the best ordered state achieved after 168 hours (7 days) of annealing. For sample annealed for 168 hours, the primary peak is obtained at $Q_{y(1)} = 0.170$ nm^{-1}. Other higher order peaks were observed at $Q_y = 0.297$, 0.321, 0.456, 0.514 and 0.629 nm^{-1} which are approximately equal to $\sqrt{3}Q_{y(1)}$, $\sqrt{4}Q_{y(1)}$, $\sqrt{7}Q_{y(1)}$, $\sqrt{9}Q_{y(1)}$ and $\sqrt{12}Q_{y(1)}$, respectively, and therefore characteristic of a hexagonal morphology.

The annealing time required to achieve the best ordered structure in 260 nm thick film was much longer time than that needed for the 50 nm film to attain the same degree of order. If the annealing time is calculated just based on thickness, 260 nm should take about (260/50) x 24 = 125 hours assuming a constant vapor diffusion rate, which is consistent with our experimental results (168 hours).

5.2.3.5 Comparison of different solvents

The 1D integrated Q_y plots for the best ordered system for SBS-I when annealed in different solvents are compared in Figure 77. For both the thicknesses, in any given solvent, well ordered hexagonally packed cylinders normal to the substrate were obtained. The information from Figure 77 is summarized in Table 9 where the effectiveness of the different solvents are compared. The annealing time in Table 9 refers to the solvent exposure time that produced the most ordered system in each film.

From Table 9, it can be seen that for 50 nm thick films annealed in toluene vapors,

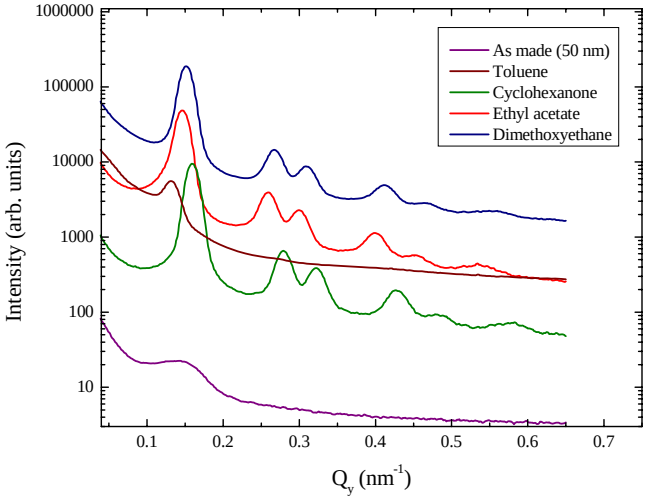

(a) 50 nm

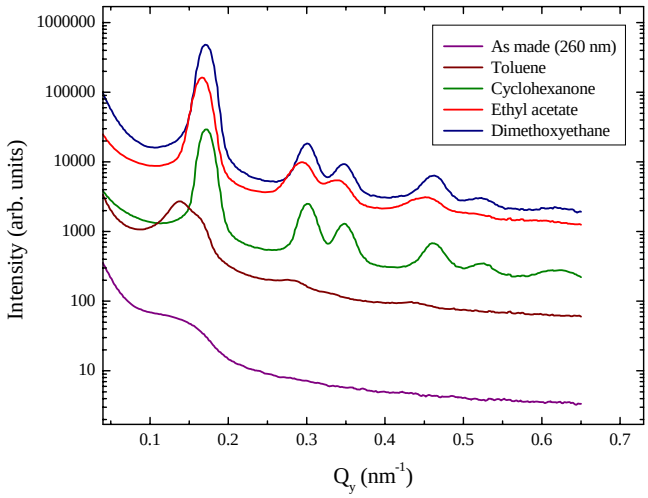

(b) 260 nm

Figure 77: 1D GISAXS horizontal profiles for 50 nm and 260 nm thick SBS-I films when annealed in different solvent vapors.

Table 9: Characteristics of the 1D GISAXS integral plots of the solvent annealed SBS-I films

Notation	**50 nm**	**260 nm**
Toluene		
No. of bragg peaks	1	3
Annealing time (hours)	6	6
Domain spacing (nm)	47.9	45.5
Dimethoxyethane		
No. of bragg peaks	6	6
Annealing time (hours)	6	24
Domain spacing (nm)	41.3	36.9
Ethyl acetate		
No. of bragg peaks	6	4
Annealing time (hours)	18	24
Domain spacing (nm)	43.0	37.8
Cyclohexanone		
No. of bragg peaks	5	6
Annealing time (hours)	24	168
Domain spacing (nm)	39.7	36.9

even in the most ordered state, no higher order peaks are observed. This means that toluene vapors are not at all effective in annealing these SBS-I films. Comparing the rest of the solvent vapors for 50 nm thick SBS-I films, DME, EAC and cyclohexanone are equally effective in creating order when comparing in terms of the higher orders of Bragg peaks.

The different solvents take different lengths of time to induce the most ordered state. For example, in the case of the 50 nm thick films, the annealing times are - 6 hours for DME annealing, 18 hours for EAC annealing, 24 hours for cyclohexanone. The difference in times taken by DME and EAC to create the most ordered structure can be explained based on χ_ϵ arguments discussed in section 5.1. Figure 78 shows the effective interaction parameter as a function of the solvent volume fraction.

As previously discussed, EAC decreases the χ_ϵ value making the PS and PB slightly less incompatible thereby reducing the kinetics of phase separation. Conversely, DME increases χ_ϵ making the polymers more incompatible and hence having

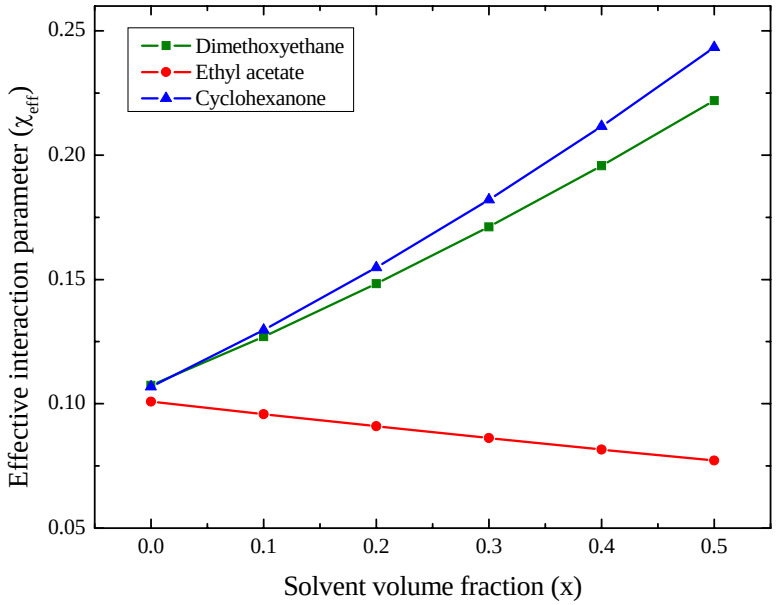

Figure 78: Effective interaction parameter calculated from Equation 8 as a function of the solvent volume fraction

the tendency to increase kinetics. In the case of cyclohexanone, the calculated χ_ϵ indicates that the incompatibility between the PS and the PB phase increases with the increase in the solvent volume fraction. This increase was rather unexpected given that the films annealed in cyclohexanone take the longest time to reach similar ordered state as achieved in DME and EAC annealing. The longer annealing time in cyclohexanone can be explained on the basis of the extremely low vapor pressure (2 mm Hg) of the cyclohexanone which may now be the dominating factor in the slow kinetics observed to attain the best ordered state.

In case of 260 nm thick films, the most ordered films (based on the number of Bragg peaks observed) are obtained when annealed in DME and cyclohexanone followed by EAC. Similar to the 50 nm thick films, cyclohexanone takes longer time to reach the most ordered state as compared to DME and EAC. These states give the least domain size. The domain size starts increasing once the film starts to loose order and eventually start dewetting.

5.2.4 Effect of incidence angle

The X-ray penetration depth in thin films can be controlled by varying the incident angle, providing details on the depth dependence of the thin film morphology. With increasing incident angle, X-rays penetrate deeper into the film. GISAXS measurements were taken at a series of incident angles ranging from 0.05^0 to 0.25^0 to achieve depth dependent information from the thin films. At an incident angle of 0.05^0 the GISAXS scattering is predominantly from the surface of the film whilst at 0.25^0 the scattering is dominated by the bulk of the film thickness.

2D GISAXS patterns at different incident angles for the most ordered state of a 50 nm thick film when annealed in DME are shown in Figure 79. As the incidence angle

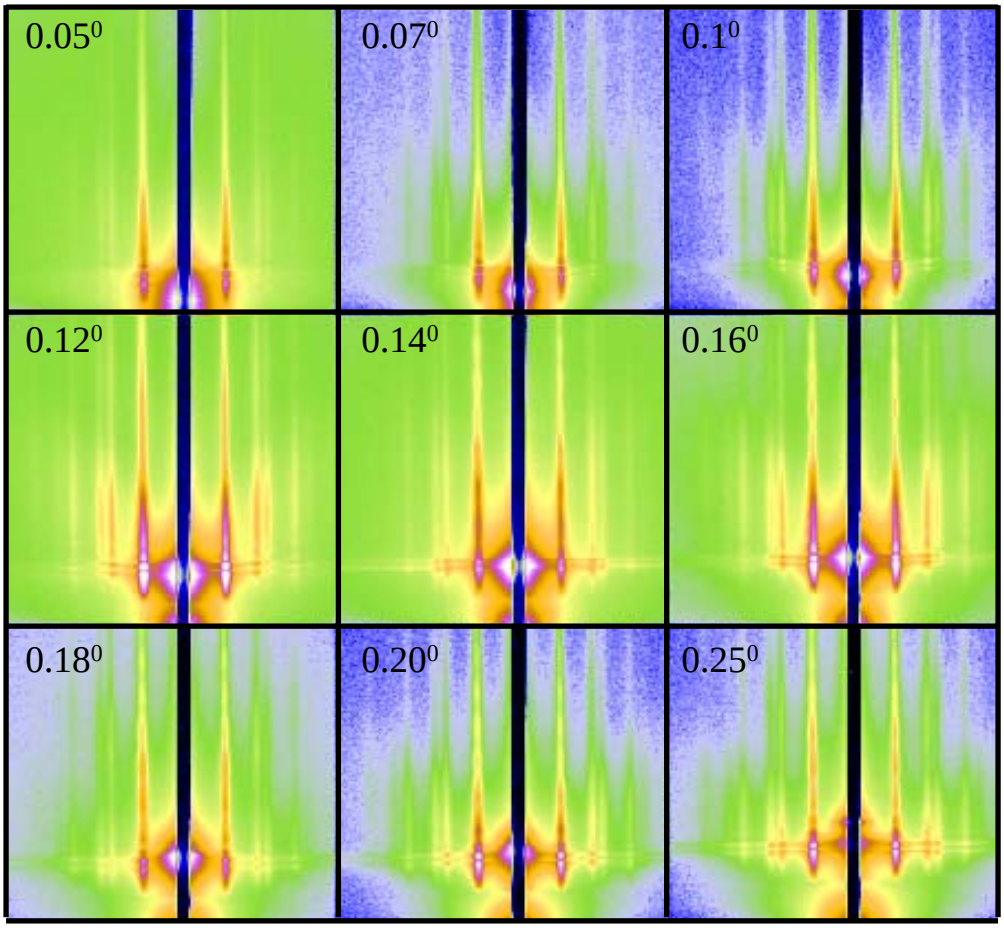

Figure 79: 2D GISAXS patterns at different incident angles for 50 nm SBS-I film annealed in DME for 6 hours

increases, the higher order peaks become more visible, as shown by the integrated Q_y plots in Figure 80.

It is evident from this plot that the intensity of the Bragg peaks increases with increasing incident angle. The absolute intensity of the 4^{th} order peak (indicated by arrow) is plotted as a function of the angle of incidence in Figure 80(b) where the increase in the peak intensity can be seen. This indicates that the structure within the bulk of the film is more ordered than the structure at the surface. This can be partly explained by noting that when the film dries, the rate of evaporation of the solvent is highest at the top surface. Clearly the ordering of the BCP is affected by the rate of evaporation [89]. However, by comparison, the further away from the surface, the slower is the rate of evaporation and consequently providing a longer time for the BCPs to attain a lower energy morphology.

To quantify the depth dependent structure of the film, we have analyzed the samples using X-ray reflectivity measurements. The raw intensity data versus incident angle were all corrected for sample geometry and converted to a Q scale.

A summary of the reflectivity data for the DME and EAC annealed films are shown in Figures 83 and 82, respectively. The value of the critical Q below which the X-rays are totally reflected in all cases is 0.029 ± 0.002 $\mathring{A}^{-1}$ which is consistent with the theoretical value of Si. Above the critical Q, the reflectivity is seen to fall off rapidly following the Fresnel power law dependence (Q^{-4}) and then levels off due to the growing contributions from the background at higher Qs. X-rays reflected from the top and bottom surface of the film, result in well defined oscillations (called Kiessig fringes) observed in the reflectivity. These fringes have a period in Q which is inversely proportional to the thickness of the film. Thus, a smaller period means a higher film thickness and a longer period means small thicknesses.

The reflectivity data were fitted using both Paratt 32 (C. Brown, HMI, Berlin) as well SURFace software (J. Webster, ISIS, UK) using a 3 layer fitting model. Apart

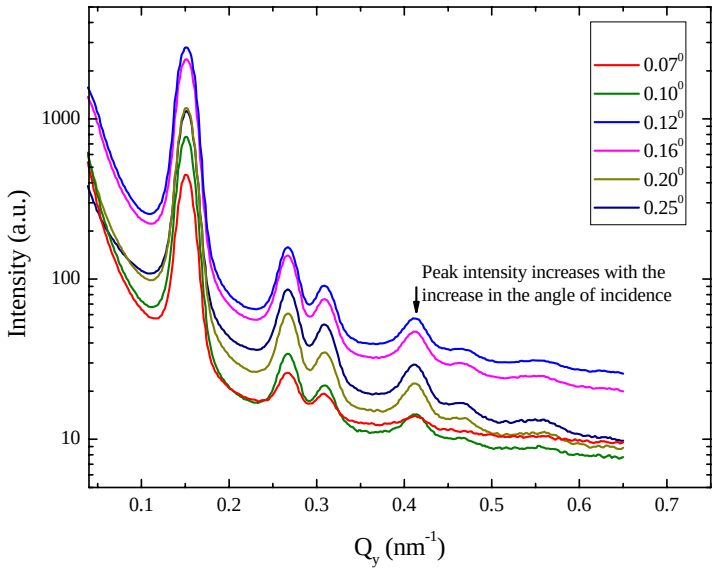

(a) 1D plots of Q_y as a function of incident angle

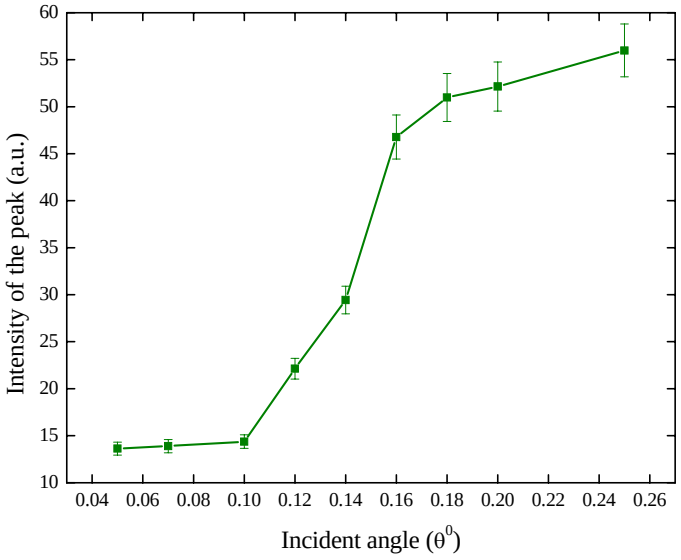

(b) Peak intensity of the 4^{th} order peak as a function of incident angle

Figure 80: Intensity of the peak as a function of the incident angle for SBS-I 50 nm film annealed in DME for 6 hours

from the known SiOx layer, the fitting model in all cases demonstrated that the polymer could not be fitted by a homogeneous single layer but that the film consists of two layers composing bulk and the surface layers, which have different scattering length densities. This is consistent with the GISAXS results (varying incident angle measurements) which found that the degrees order on the surface and in the bulk film are different.

An example of the model used to fit the reflectivity data for all the 50 nm EAC film annealed for 18 hours is shown in Figure 81 where the total thickness of the film was shown to be 50±10 nm in all samples.

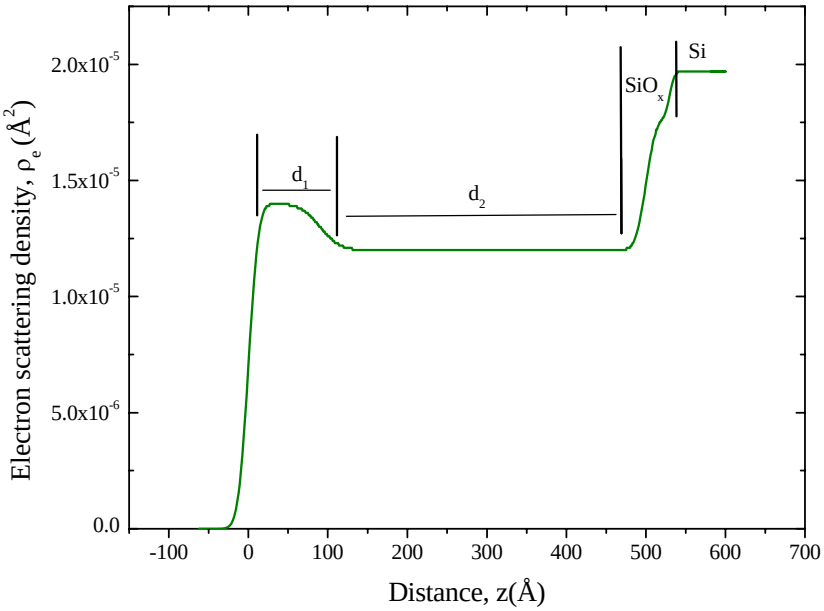

Figure 81: Electron density as a function of the vertical distance for a 50 nm film

Figures 82 and 82 show the X-ray reflectivity data together with the model fits for 50 nm SBS-I at different DME and EAC annealing times. For films annealed with EAC, data at 3 hours could not be fitted using the model. The rest of the data at different annealing times show similar behavior. For films annealed in DME shown in Figure 83, ordering within the film is also effectively similar except in the case of 3 hour annealing, the reasons for which are not clear.

So here we report only the data for the free surface layer thickness. The change

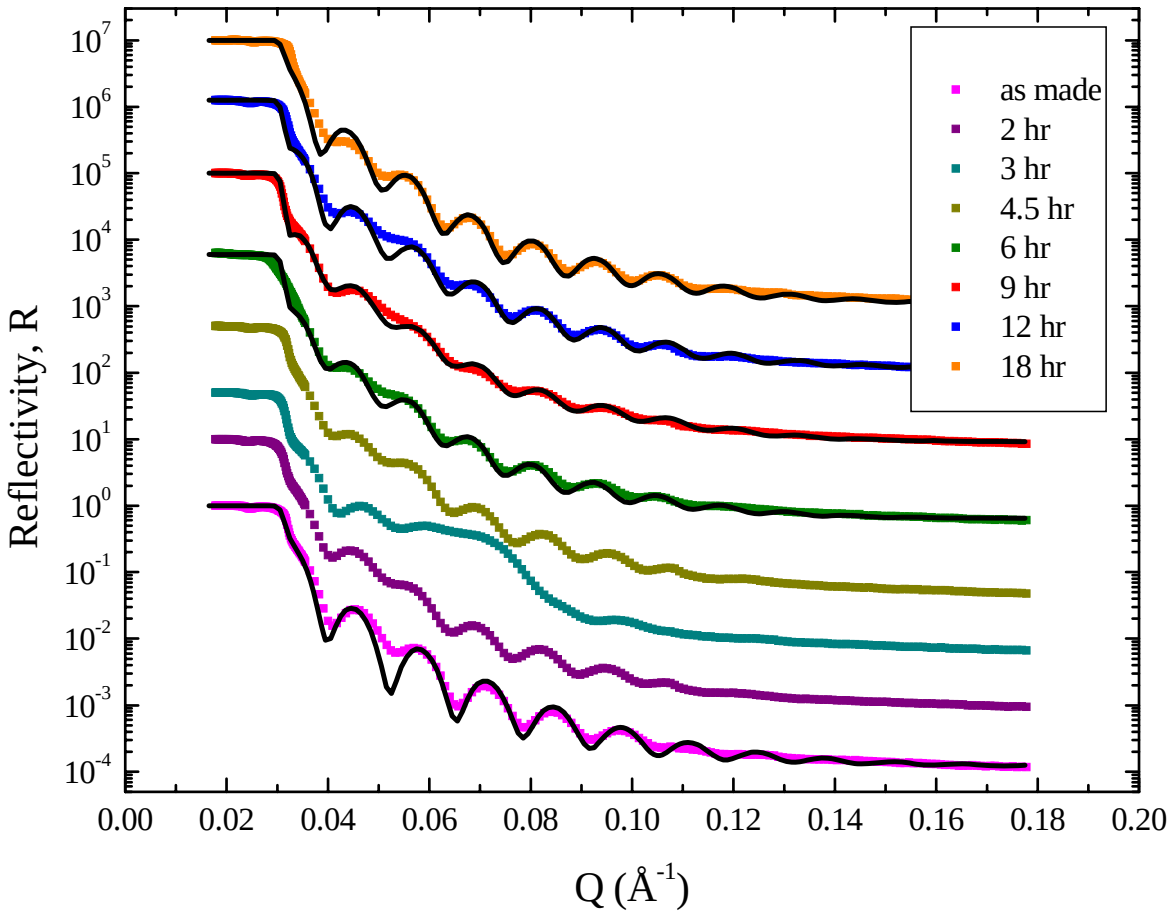

Figure 82: X-ray reflectivity data (dots) displayed together with model fits (solid lines) for 50 nm SBS-I films solvent annealed in EAC.

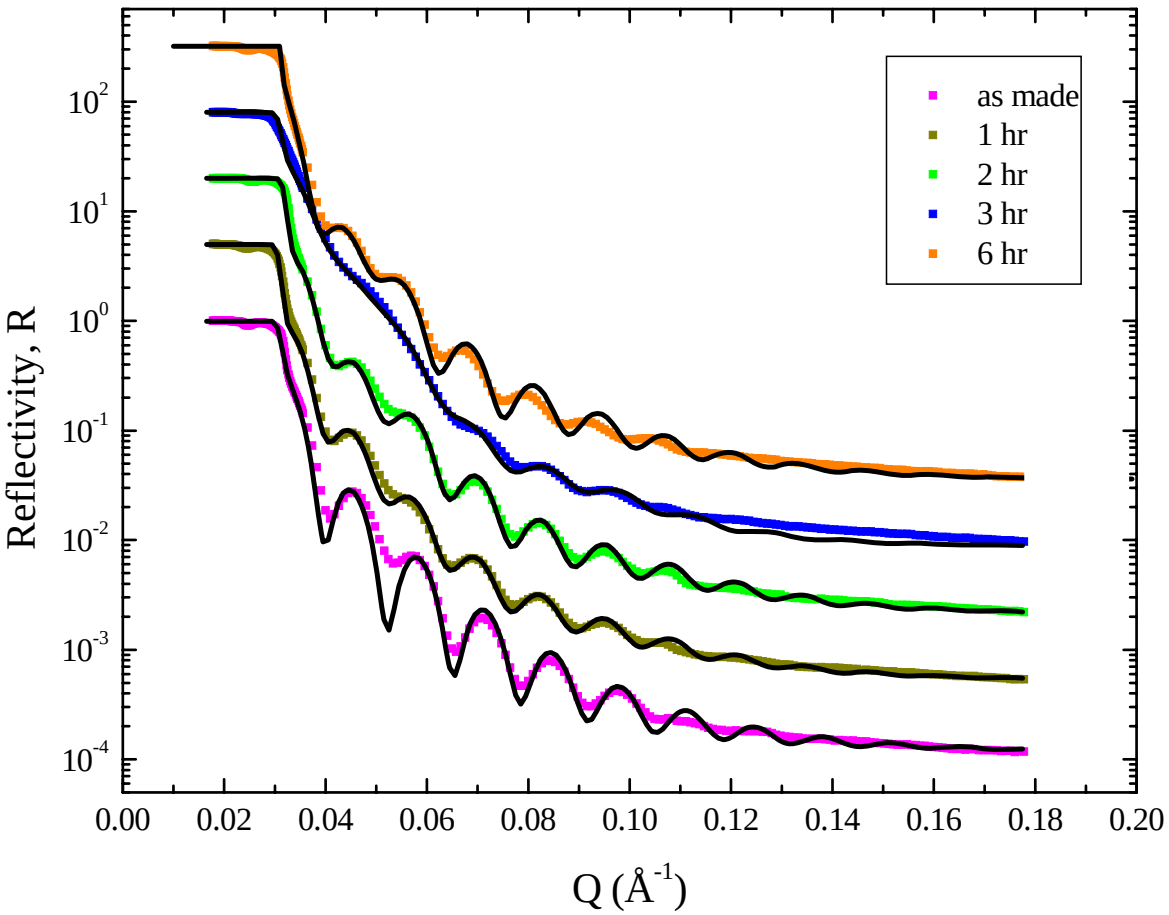

Figure 83: X-ray reflectivity data (dots) displayed together with model fits (solid lines) for 50 nm SBS-I films solvent annealed in DME.

in the thickness of the top layer d_1 as a function of annealing time for films annealed in EAC and DME is shown in Figure 84. From these plots, it can be seen that as soon as annealing begins, the layer thickness (d_1) of this surface layer decreases and as annealing time increases, the layer attains a constant value. These results indicate that the density of the free surface is different from the bulk of the film, because of solvent evaporation effects.

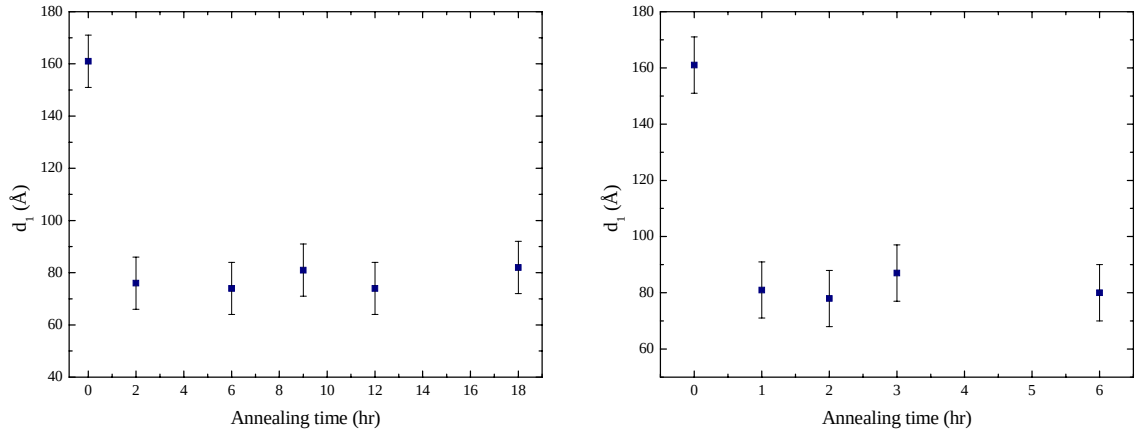

(a) Ethyl acetate (EAC) (b) Dimethoxyethane (DME)

Figure 84: Variation in the thickness of the top layer of the 50 nm film as as function of annealing time of EAC and DME.

5.2.5 In-situ studies

To evaluate the differences in behavior between films annealed ex-situ and in-situ, i.e. film structures resulting from solvent vapor evaporation versus the structures formed whilst saturated by vapor, we undertook in-situ vapor annealing during GISAXS measurements. The experimental set up is given in Section 3.2.3.2. These preliminary measurements were performed on 50 nm films SBS-I films annealed using ethyl acetate vapors. The data were collected every minute for this sample. A set of representative GISAXS patterns as a function of time is presented in Figure 85.

The as-made structure of the film (Figure 85(b)) shows a weak Bragg peak at $Q_y \sim 0.15$ nm^{-1}. This peak does not run parallel to the specular ridge but instead

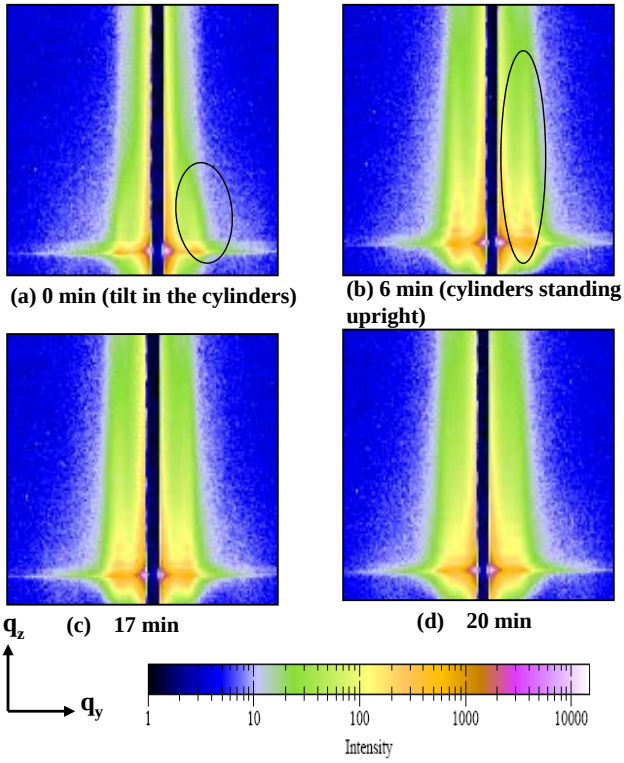

Figure 85: 2D GISAXS scattering profiles from SBS-I (50 nm) film during in-situ solvent annealing using ethyl acetate at different exposure times.

is tilted towards the specular ridge. This indicates that the structures are not fully aligned normal to the surface but are inclined on average 25^0 away from normal. This incline in the cylinders is observed up to 5 minutes. However, somewhere between 5 and 6 minutes (see Figure 85(b)) of solvent exposure, the tilted structure becomes fully perpendicular to the surface. The ordering of the structure did not show much improvement from 6 minutes to 20 minutes. Unfortunately, the flow rate of the solvent was sufficient enough to solvate the film and dewet it from the surface after 20 minutes.

Figure 86 shows the 1D integrated Q_y plots as a function of the annealing time. Clearly only the primary peak is observed, the intensity of which increases and becomes more defined for times up to 6 minutes which indicates improvement in the order. For longer annealing times, the primary peak broadens which could be due to the fact that the homogeneity of the film worsens because of the high flow rate of

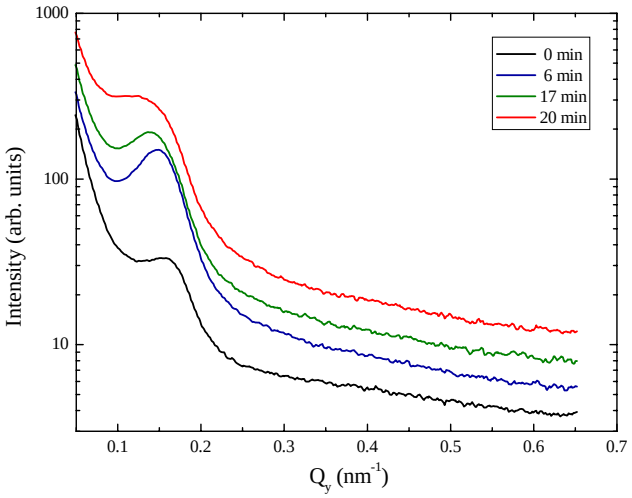

(a) In-plane scattering measured at an angle 0.25^0

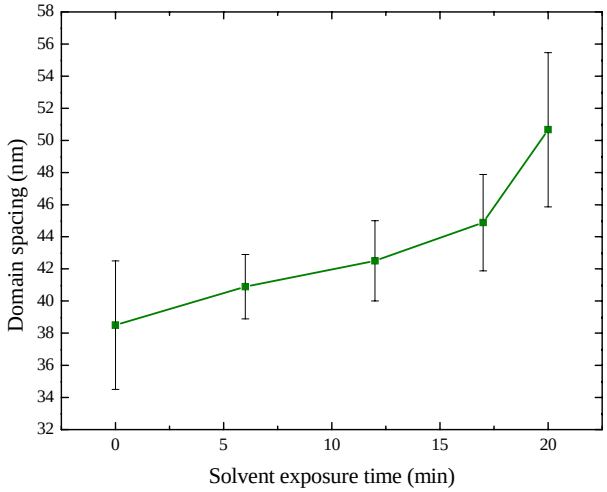

(b) Domain spacing as a function of time

Figure 86: In-plane scattering profiles and corresponding domain spacings for 50 nm SBS-I film as it undergoes in-situ annealing using ethyl acetate

the solvent. The domain size of the BCP film (see Figure 86(b)) as determined from the primary peak position keeps increasing with annealing time as the film is exposed to more solvent. Even with this limited set of in-situ results, the effectiveness of an annealing solvent like ethyl acetate can still be seen.

The striking feature of these data are the stark contrast to the results from the equivalent ex-situ EAC annealed films shown in Figure 73 which formed highly ordered structures after solvent removal. One difference in these films is the rate at which the solvent evaporates. In the in-situ annealed films, due to the high flow rate, there is a high flux of the solvent in and out of the film which does not give the solvent enough residence time in the film to improve its structural order. This argument fits in with findings for ex-situ EAC annealed samples, where high orders are achieved after 18 hours of annealing time. Although the effect of the rate of solvent evaporation on the morphology and orientation of cylinder forming thin films have been reported [89], they can not be directly compared to our system. In our work, the flow rate was 463 cc/min (or, 7.7 ml/s) during the in-situ annealing of the films which is 3 orders of magnitude higher than the highest flow rate of 5 nL/s in their case used by other authors. It will however be of great interest to perform a series of in-situ measurements using GISAXS in a controlled solvent environment. This will enable us to compare the ex-situ films directly and also, give a better understanding of the structural evolution of the films especially in case of films spun cast on mica where the orientation changes as a function of annealing time from perpendicularly aligned cylinders to in-plane alignment.

5.3 Conclusions

Solvent vapor annealing is an effective technique for creating long-range order in block copolymer thin films. The ability to control the structure by influencing phase transitions through the use of different solvents adds a degree of control unavailable

to thermally annealed systems. SBS-I films behaved differently in terms of their orientation when annealed on different surface energy substrates with the same solvent annealing conditions. On mica, the films initially ordered normal to the substrate but after several hours of extended annealing, ordering only occurred parallel to the substrate. By contrast on silicon substrates, the film surface always showed cylinders normal to the substrate. On both substrates, extended annealing does however lead to dewetting of the film.

The effect of solvent exposure time was studied for toluene, DME, EAC and cyclohexanone. Considerable improvement was observed in the hexagonal order for the solvent annealed films (50 nm and 260 nm) which was proven by multiple order reflections observed in GISAXS. All solvents except toluene (spin casting solvent) were effective in imparting order in SBS-I morphology with the most ordered states obtained when annealed in DME and cyclohexanone. The solvent exposure time needed to achieve the most ordered state increased as the thickness of the films increased from 50 nm to 260 nm. The kinetics of the annealing processes for a constant film thickness for selective solvents can be understood by means of a change in the effective interaction parameter (χ_ϵ) as a function of solvent volume fraction. It was found that the higher the value of χ_ϵ (which characterizes the incompatibility between the PS and PB phases), the less time it takes for the film to reach its best ordered state. For a relatively neutral solvent like cyclohexanone, the lower vapor pressure is the determining factor for the kinetics of the annealing process.

From GISAXS measurements done at different incident angles, it was found that the order in the film structure is highest close to the substrate, with less order at the free surface. These data are supported from fits to the X-ray reflectivity data which show that there was a difference in the structure as a function of the film thickness.

CHAPTER VI

CONCLUSIONS AND FUTURE DIRECTIONS

6.1 Conclusions

The goal of this work was to contribute to the better understanding of BCP and nanoparticle interactions and long range order of BCPs. The major findings of this work are summarized below:

6.1.1 BCP-nanoparticle composite studies

- The gold nanoparticles were successfully transferred from aqueous solutions into an organic solvent (toluene) and individually dispersed when added to the SB and SBS block copolymers to form stable bulk samples of block copolymer-nanoparticle composites.

- The gold nanoparticles were successfully templated using the BCPs. This was achieved by selective segregation of the gold nanoparticles in the PB domains.

- It was found that the gold nanoparticles are located within the bulk of the PB domains for R_p/R_g ratio = 0.21 - 0.39. This location was confirmed by TEM, NMR and DSC measurements.

- With the addition of gold, there was an increase in the apparent volume fraction of the PB domains in order to accommodate gold in the PB domains. This led to a morphology transition in the BCP system. There was a general trend of reduced order in the BCP structure with an increase in the gold loading.

- C_{60} nanoparticles were successfully incorporated into the BCP systems. However, the structure of the BCP with C_{60} inclusions was not as ordered as compared to the BCP with gold inclusions. This can be explained based on the difference in the sample preparation methods in both cases. The precipitation method used for C_{60} may not be giving enough time for the high ordering of the BCP.

6.1.2 Solvent annealing studies

- Annealing in a solvent atmosphere of dimethoxyethane, ethyl acetate and cyclohexanone was shown to be highly effective in enhancing the degree of lateral order of the microdomains in thin films.

- Toluene was found to be the worst solvent for annealing as there was no significant improvement in the order of the films especially for 50 nm thickness.

- The kinetics of annealing for selective solvents was understood in terms of the change in the effective interaction parameter of the system which characterizes the incompatibility between the block components. When solvent annealed, the introduction of the solvent modifies the effective interaction parameter changes between the components. The more incompatible the blocks become, the faster the drive is towards an ordered structure.

- The most effective annealing solvents for 50 nm films were DME and ethyl acetate and for 260 nm films, dimethoxyethane and cyclohexanone were the most effective. The time taken to achieve the most ordered state increases as the film thickness increases.

- For each sample made on the piranha-treated silicon wafers, alignment of the cylinders perpendicular to the substrate was obtained consistently irrespective of the film thickness. This is an interesting result because we obtained stable

perpendicular cylinders without the use of any external field or neutralizing the substrate. This is encouraging for potential usage of these films in applications like magnetic storage media.

- It was shown that by the appropriate choice of the substrate, orientation of the cylinder structure surfaces were be tuned to align either perpendicular (on silicon wafers) or parallel (on mica substrate) to the substrate interface.

- The films (both 50 and 260 nm) are more ordered close to the substrate than that of the top surface which was observed by careful analysis of GISAXS measurements performed at different incident angles. This was further supported by electron density profiles calculated from X-ray reflectivity measurements.

6.2 Future directions

6.2.1 BCP-nanoparticle composite studies

- In BCP-gold inclusion studies, more concentrations should be made and studied to find out the exact concentration at which the morphology transition occurs. Given enough data points, a phase map for the polymer can be constructed.

- For BCP-C_{60} systems, NMR spin diffusion experiments need to be performed to locate the C_{60} nanoparticles in the BCP systems and to find out if they selectively segregate in one phase.

- The nanoparticle inclusions study can be extended to a wider range of nanoparticles differing in their type, size and shape for a greater understanding of the BCP behavior. Incorporation of magnetic particles like iron oxide will be useful for potential applications in magnetic storage devices.

- Work done on the nanoparticle inclusions in BCP thin films (see Appendix A) suggests that the gold nanoparticles accelerate the dewetting in thin films. It

will be interesting to study the dewetting kinetics as a function of temperature, annealing time, concentration and type of nanoparticles for a complete analysis.

6.2.2 Solvent annealing studies

- For the same annealing conditions, the solvent annealed films showed different film surfaces on mica and piranha cleaned silicon wafers. To understand the interactions between the film and the surface, it will be interesting to analyze the surface of the substrates further by using surface techniques like XPS.

- There was limited work carried out on films spun cast from solvents other than toluene, for example, for films spun cast and solvent annealed in cyclohexanone showed remarkable order. A detailed analysis of these different BCP-solvent systems (ex-situ and in-situ measurements) can be carried out to gain a better understanding about the kinetics and evolution of the order in the structure.

- Using the GISAXS data, characterization of the long range order in films made on piranha-treated silicon wafers can be done by finding a correlation length in the structure. This will involve fitting the data with a paracrystalline model. In addition, AFM phase measurements can be performed and the film surfaces can be analyzed using software such as that developed at Princeton University [94] where the degree of lateral order is quantified based on the number of defects.

- For the solvent annealed films, an in-depth analysis has been presented about the lateral structure of the film by analyzing the horizontal plots along Q_y. GISAXS data also gives information in the Q_z direction which can be analyzed for all the solvent annealed SBS-I films to provide information through the thickness of the film. Combining this information with the Kiesseg fringes from reflectivity measurements can establish if the cylinders (perpendicular cylinders) extend from the interface all the way up to the surface.

APPENDIX A

THIN FILM STUDIES - (DEWETTING)

One of the initial objectives of our work was to template nanoparticles in 1-2 layers thick BCP films and then produce long range alignment of the system [104, 105]. In our work, it was found that addition of small percent of nanoparticles (gold - 5 nm) led to an accelerated dewetting[1] of the otherwise stable 50 nm SBS-I films (the stable film refers to film without nanoparticles which does not dewet for the lengths of time discussed here).

Fig 87 shows the AFM micrographs of 50 nm (1%) SBS-I films with 1 (wt%) addition of gold nanoparticles (5 nm) where Fig 87(a) and 87(b) represent phase and height images of the as-spun film and Fig 87(c) and 87(d) are phase and height images of the same films after 10 days at room temperature. Holes and fingering instabilities characteristic of the dewetting pattern can be observed. It was observed that the feature size characteristic of the dewetting in these films increases as the percent addition of gold increases. This is confirmed by the optical micrographs of these thin films shown in Figure 89. Figure 90 shows the same dewetted films (shown in Figure 89) after annealing at 80^0C overnight. By annealing these films, the circular holes and the fingering structures formed at the early stages of annealing grow in size eventually form a surface pattern characteristic of a fully dewet sample. The most probable mechanism seems to be that the nanoparticles were acting as nucleation sites and promoting dewetting [160, 161].

[1]The process by which an initially uniform film of liquid on a non wetting substrate breaks up into droplets is known as dewetting.

Our results contradict the recent reports where low concentrations of nanoparticles in the polymer have been shown to suppress dewetting [162, 163]. These groups utilized fullerene (C_{60}) and poly(benzyl ether) dendrimers as nanoparticle additives respectively. Both groups found that the addition of even a small amount of particles to the spin-casting solution led to a strong inhibition of dewetting. It will be interesting to study the dewetting kinetics as a function of temperature, annealing time, concentration and type of nanoparticles for a complete analysis.

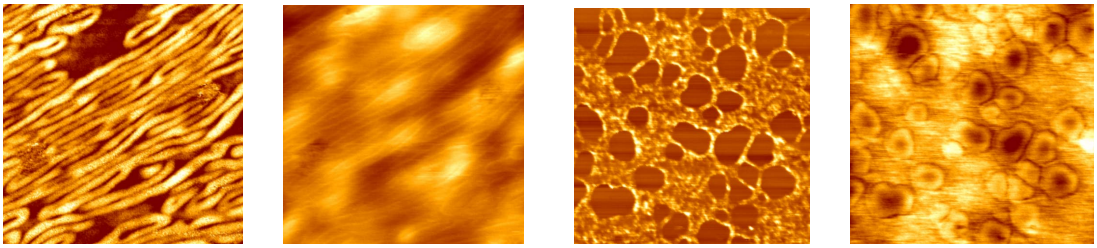

(a) 1% film (as spun) phase image (b) 1% film (as spun) height image (c) Dewetted 1% film phase image (d) Dewetted 1% film height image

Figure 87: AFM micrographs (1.5μm X 1.5μm) of 50 nm SBS-I film with 1 (wt%) addition of gold (5 nm) particles.

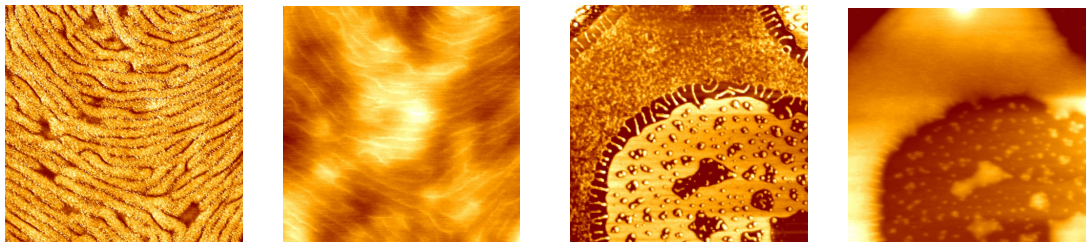

(a) 3% film (as spun) phase image (b) 3% film (as spun) height image (c) Dewetted 3% film phase image (d) Dewetted 3% film height image

Figure 88: AFM micrographs (1.5μm X 1.5μm) of 50 nm SBS-I film with 3 (wt%) addition of gold (5 nm) particles.

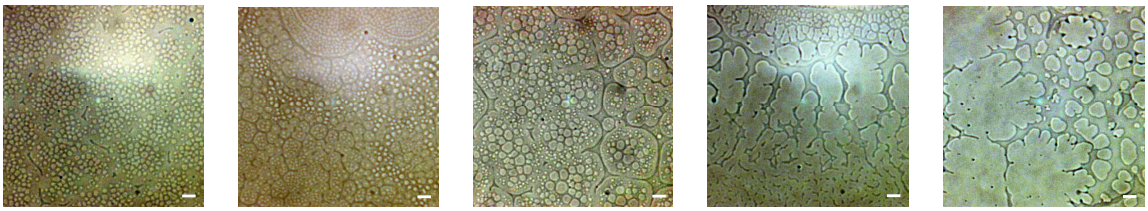

(a) 0.1% gold (b) 0.5% gold (c) 1% gold (d) 3% gold (e) 5% gold

Figure 89: Optical micrographs of dewetted (after 10 days) 50 nm SBS-I film with different weight % addition of gold (5 nm) particles. (scale bar = 100μm)

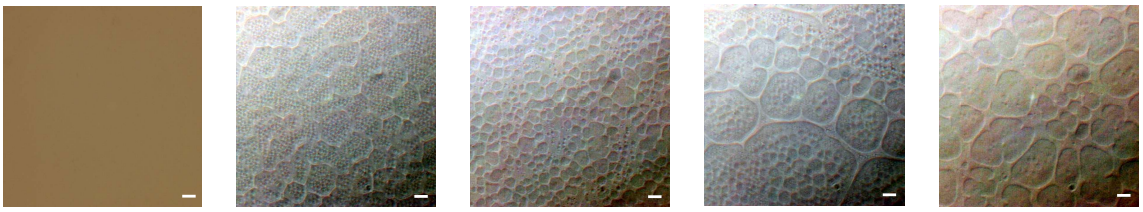

(a) 0.1% gold (b) 0.5% gold (c) 1% gold (d) 3% gold (e) 5% gold

Figure 90: Optical micrographs of annealed 50 nm SBS-I film with different weight % addition of gold (5 nm) particles. (scale bar = 100μm)

REFERENCES

[1] Park, M. *Science*, vol. 276, p. 1401, 1997.

[2] Cheng, J. *Applied Physics Letters*, vol. 81, no. 19, p. 3657, 2002.

[3] Chen, Z.-R. *Science*, vol. 277, p. 1248, 1997.

[4] Bates, F. and Fredrickson, G. *Physics Today*, vol. 52, p. 32, 1999.

[5] Frerickson, G. and Bates, F. *Annu. Rev. Mater. Sci.*, vol. 26, p. 501, 1996.

[6] Flory, P., *Principles of Polymer Chemistry*. Cornell University Press, Ithaca, 1966.

[7] Hamley, I. *Journal of Physics: Condensed Matter*, vol. 13, p. R643, 2001.

[8] Bates, F. *Science*, vol. 251, p. 898, 1991.

[9] Bendejacq, D., Posinet, V., and Joanicot, M. *Macromolecules*, vol. 35, p. 6645, 2002.

[10] "Block copolymer morphologies." Course website, June 2003. Chemistry 384 Lecture Notes.

[11] khandpur, A., Forster, S., Bates, F.S. anf Hamley, I., Ryan, A., Bras, W., Almdal, K., and Mortensen, K. *Macromolecules*, vol. 28, p. 8796, 1995.

[12] Hajduk, D., Takenouchi, H., Hillmyer, M., Bates, F., Vigild, M., and Almdal, K. *Macromolecules*, vol. 30, p. 3788, 1997.

[13] Zheng, W. and Zhen-Gang, W. *Macromolecules*, vol. 28, p. 7215, 1995.

[14] Park, C., Yoon, J., and Thomas, E. L. *Polymer*, vol. 44, p. 6725, 2003.

[15] Stadler, R., Auschra, C., B. J., Krappe, U., Voigt-Martin, I., and Leibler, L. *Macromolecules*, vol. 28, p. 3080, 1995.

[16] Bates, F. *MRS Bulletin*, vol. 30, p. 525, 2005.

[17] Chatterjee, J., Jain, S., and Bates, F. *Macromolecules*, vol. 40, p. 2882, 2007.

[18] Gido, S., Gunther, J., Thomas, E., and Hoffman, D. *Macromolecules*, vol. 26, p. 4506, 1993.

[19] Gido, S. and Thomas, E. *Macromolecules*, vol. 27, p. 849, 1994.

[20] Frerickson, G. *Macromolecules*, vol. 20, p. 2535, 1987.

[21] Russell, T., Coulon, G., Deline, V., and Miler, D. *Macromolecules*, vol. 22, p. 4600, 1989.

[22] Hamley, I. *Angewandte Chemie-International Edition*, vol. 42, no. 15, p. 1692, 2003.

[23] Fasolka, M. and Mayes, A. *Annu. Rev. Mater. Res.*, vol. 31, p. 323, 2001.

[24] Fukunaga, K., Hashimoto, T., Elbs, H., and Krausch, G. *Macromolecules*, vol. 35, no. 11, p. 4406, 2002.

[25] Pickett, G. and Balazs, A. *Macromolecules*, vol. 30, p. 3097, 1997.

[26] Matsen, M. *J. Chem. Phys.*, vol. 106, p. 7781, 1997.

[27] Huinink, H., Brokken-Zijp, J., and van Dijk, M. *J. Chem. Phys.*, vol. 112, p. 2452, 2000.

[28] Geisinger, T., Müller, M., and Binder, K. *J. Chem. Phys.*, vol. 111, p. 5241, 1999.

[29] Wang, Q., Nealey, P., and de Pablo, J. *Macromolecules*, vol. 34, p. 3458, 2001.

[30] Kim, H. and Russell, T. *J. Polym. Sci.*, vol. 39, p. 663, 2001.

[31] Morkved, T. and Jaeger, H. *Europhys. Lett.*, vol. 40, p. 643, 1997.

[32] Mansky, P., Liu, Y., Huang, E., Russell, T., and Hawker, C. *Science*, vol. 275, p. 1458, 1997.

[33] Huang, E., Russell, T., Harrison, C., Chaikin, P., Register, R., Hawker, C., and Mays, J. *Macromolecules*, vol. 31, p. 7641, 1998.

[34] Kellogg, G., Walton, D., Mayes, A., Lambooy, P., Russell, T., Gallagher, P., and Satja, S. *Phys. Rev. Lett.*, vol. 76, p. 2503, 1996.

[35] Huang, E., Pruzinsky, S., and Russell, T. *Macromolecules*, vol. 32, p. 5299, 1999.

[36] Muthukumar, M. and Ober, C. *Science*, vol. 277, no. 5330, p. 1225, 1997.

[37] Bockstaller, M., Mickiewicz, R., and Thomas, E. *J. Am. Chem. Soc.*, vol. 17, p. 1331, 2005.

[38] Feynman, R., "There's plenty of room at the bottom," in *American Physical Society*, vol. 2, (California), California Institute of Technology, Engineering and Science, 1960.

[39] Ober, C. and Gabor, A. *J. Photopoly. Sci. Tech.*, vol. 9, p. 1, 1996.

[40] DeSimone, J., York, G., McGrath, J., Gozdz, A., and Bowden, M. *Macromolecules*, vol. 24, p. 5330, 1991.

[41] gabor, A., Lehner, E., Mao, G., Schneggenburger, L., and Ober, C. *Chem. Mater.*, vol. 6, p. 927, 1994.

[42] Vasilev, C., Heinzelmann, H., and Reiter, G. *J. Polym. Sci B: Polym. Phys.*, vol. 42, p. 1312, 2004.

[43] Yin, Y., Lu, Y., Gates, B., and Xia, Y. *J. Am. Chem. Soc.*, vol. 123, p. 8718, 2001.

[44] Ulman, A. *Adv. Mater.*, vol. 3, p. 298, 1996.

[45] Fendler, J. *Chem. Mater.*, vol. 8, p. 1616, 1996.

[46] Hurd, A. and Schaefer, D. *Phys. Rev. Lett.*, vol. 54, p. 1043, 1985.

[47] Rapaport, H., Moller, G., Knobler, C., Jensen, T., Kjaer, K., Leiserowitz, L., and Tirrell, D. *J. Am. Chem. Soc.*, vol. 124, p. 9342, 2002.

[48] Pozzo, D. and Walker, L. *Macromolecular Symposia*, vol. 227, p. 203, 2005.

[49] Gourishankar, A., Shukla, S., Pasricha, R., Sastry, R., and Ganesh, K. *Curr. Appl. Phys.*, vol. 5, p. 102, 2005.

[50] Mirkin, C., Letsinger, R., Mucic, R., and Storhoff, J. *Nature*, vol. 382, p. 607, 1996.

[51] Alivisatos, P., Johnsson, K., Peng, X., Wilson, T., Loweth, C., Bruchez, M., and Schultz, P. *Science*, vol. 382, p. 609, 1996.

[52] Kim, S., Solak, H., Stoykovich, M., Ferrier, N., dePablo, J., and Nealey, P. *Nature*, vol. 424, p. 411, 2003.

[53] Sundarani, D., Darling, S., and Sibener, S. J. *Nanoletters*, vol. 4, p. 273, 2004.

[54] Thurn-Albrecht, T., Schotter, J., Kästle, G., Emley, N., Shibauchi, T., Krusin-Elbaum, L., Black, C., Tuominen, M., and Russell, T. *Science*, vol. 290, p. 2126, 2000.

[55] Ahmed, S. and Kofinas, P. *Journal of Magnetism and Magnetic Materials*, vol. 228C, p. 219, 2005.

[56] Cummins, C., Schrock, R., and Cohen, R. *Chem. Mater.*, vol. 4, p. 27, 1992.

[57] Abe, J., Cohen, R., and Ross, C. *Chem. Mater.*, vol. 15, p. 1125, 2003.

[58] Boyen, H., Kastle, G., Zurn, K., Herzog, T., Weigl, F., Ziemann, P., Mayer, O., Jerome, C., Moller, M., Spatz, J., Garnier, M., and Oelhafen, P. *Advanced Functional Materials*, vol. 13, p. 359, 2003.

[59] Tannenbaum, R., Reich, S., Flennikin, C., and Goldberg, E. *Advanced Materials*, vol. 14, p. 1402, 2002.

[60] King, S., Hyunh, K., and Tannenbaum, R. *J. Phys. Chem. B*, vol. 107, p. 12097, 2003.

[61] Chiu, J., Kim, B., Kramer, E., and Pine, D. *J.Am. Chem. Soc.*, vol. 127, p. 5036, 2005.

[62] Bockstaller, M., Kolb, R., and Thomas, E. *Advanced Materials*, vol. 13, p. 1783, 2001.

[63] Hamdoun, B., Ausserre, D., Joly, S., Gallot, Y., Cabuil, V., and Clinard, C. *Journal of Physics II France*, vol. 6, p. 493, 1996.

[64] Lin, Y., Boker, A., He, J., Sill, K., Xiang, H., Clarissa, A., Wang, J., Emrick, T., Long, S., Wang, Q., Balazs, A., and Russell, T. *Nature*, vol. 434, p. 55, 2005.

[65] Sibener, S. J., Darling, S., Hahm, J., Lee, D.-C., Sundrani, D., L. Yu, L., Yufa, N., and Zheng, Q., "Defect dynamics and diblock copolymer alignment on smooth and nanoscale confining substrates," in *American Chemical Society, Division of Polymer Chemistry*, vol. 46(2), p. 541, 2005.

[66] Thompson, R., Ginzburg, V., Matsen, M., and Balazs, A. *Science*, vol. 292, p. 2469, 2001.

[67] Bockstaller, M., Lapetnikov, Y., Margel, S., and Thomas, E. *Advanced Materials*, vol. 125, p. 5276, 2003.

[68] Spontak, R., Shankar, R., Bowman, M., Krishnan, A., Hamersky, M., Samseth, J., Bockstaller, M., and Rasmussen, K. *Nanoletters*, vol. 6, p. 2115, 2006.

[69] Buxton, G., Lee, J., and Balazs, A. *Macromolecules*, vol. 36, p. 9631, 2003.

[70] Lee, J., Thompson, R., Jasnow, D., and Balazs, A. *Macromolecules*, vol. 35, p. 4855, 2002.

[71] Yeh, S., Chang, Y., Chou, C., and Wei, K. *Macromol. Rapid Commun.*, vol. 25, p. 1679, 2004.

[72] Yeh, S., Wei, K., Sun, Y., Jeng, U., and Liang, K. *Macromolecules*, vol. 38, p. 6559, 2005.

[73] Laiho, A., R.H.A., R., Valkama, S., Ruokolainen, J., Österbacka, R., and Ikkala, O. *Macromolecules*, vol. 39, p. 7648, 2006.

[74] Lopes, W. and Jaeger, H. *Nature*, vol. 414, p. 735, 2001.

[75] Ansari, I. and Hamley, I. *Journal of Materials Chemistry*, vol. 13, no. 10, p. 2412, 2003.

[76] Segalman, R. *Materials Science and Engineering*, vol. R 48, p. 191, 2004.

[77] Lega, J., "Lecture notes - www.math.arizona.edu/ lega." Website.

[78] Segalman, R., Hexemer, A., Hayward, R., and Kramer, E. *Macromolecules*, vol. 36, p. 3272, 2003.

[79] Harrison, C., Adamson, D.H. Cheng, Z., Sebastian, J., Sethuraman, S., Huse, D., Chaikin, P., and Register, R. *Science*, vol. 290, p. 1558, 2000.

[80] Trawick, M.L. adn Angelescu, D., Chaikin, P., Sebastian, J., Register, R., Adamson, D., and Harrison, C. *Bull. Am. Phys. Soc.*, vol. 47, p. 970, 2002.

[81] Fasolka, M., Harris, D., Mayes, A., Yoon, M., and Mochrie, S. *Phys. Rev. Lett.*, vol. 79, p. 3018, 1997.

[82] Yang, X., Peters, R., Nealey, P., Solak, H., and Cerrina, F. *Macromolecules*, vol. 33, p. 9575, 2000.

[83] Segalman, R., Yokoyama, H., and Kramer, E. *Adv. Mater.*, vol. 13, p. 1152, 2001.

[84] Lin, Z., Kim, D., Wu, X., Boosahda, L., Stone, D., LaRose, L., and Russell, T. *Advanced Materials*, vol. 14, p. 1373, 2002.

[85] Kim, S., Misner, M., Xu, T., Kimura, M., and Russell, T. *Advanced Materials*, vol. 16, p. 226, 2004.

[86] Kimura, M., Misner, M., Xu, T., Kim, S., and Russell, T. *Langmuir*, vol. 19, p. 9910, 2003.

[87] Knoll, A., Magerle, R., and Krausch, G. *J. Phys. Chem. B*, vol. 120, p. 1105, 2004.

[88] Lodge, T., Pudil, B., and Hanley, K. *Macromolecules*, vol. 35, p. 4707, 2002.

[89] Kim, G. and Libera, M. *Macromolecules*, vol. 31, p. 2569, 1998.

[90] Fukunaga, K., Elbs, H., Magerle, R., and Krausch, G. *Macromolecules*, vol. 33, p. 947, 2000.

[91] Huang, H., Hu, Z., Chen, Y., Zhang, F., Gong, Y., and He, T. *Macromolecules*, vol. 37, p. 6523, 2004.

[92] Huang, H., Zhang, F., Hu, Z., Du, B., and He, T. *Macromolecules*, vol. 36, p. 4084, 2003.

[93] Cavicchi, K., Berthiaume, K., and Russell, T. *Polymer*, vol. 46, p. 11635, 2005.

[94] Angelescu, D. E., *Physics and applications of diblock copolymer thin films*. PhD thesis, Pinceton University, 2003.

[95] Kim, S., Misner, M., and Russell, T. *Advanced Materials*, vol. 16, p. 2119, 2004.

[96] Keller, A., Pedemonte, E., and Willmouth, F. *Nature*, vol. 225, p. 538, 1970.

[97] Hadziioannou, G., Mathis, A., and Skoulios, A. *Colloid. Polym. Sci.*, vol. 257, p. 136, 1979.

[98] Almdal, K., Koppi, K., and Bates, F. *Macromolecules*, vol. 26, p. 4058, 1993.

[99] Cates, M. and Milner, S. *Phys. Rev. Lett*, vol. 62, p. 1856, 1989.

[100] Balsara, N., Dai, H., Kesani, P., Garetz, B., and Hammouda, B. *Macromolecules*, vol. 27, p. 7406, 1994.

[101] Koppi, K., Tirrell, M., and Bates, F. *Phys. Rev. Lett*, vol. 70, p. 1449, 1993.

[102] Fredrickson, G. H. *J. Rheol.*, vol. 38, p. 1045, 1994.

[103] Balsara, N. and Dai, H. *J. Chem. Phys.*, vol. 105, p. 2942, 1996.

[104] Angelescu, D. E., Waller, J., Adamson, D. H., Paru, D., Chou, S., Register, R. A., and Chaikin, P. M. *Adv. Mater.*, vol. 16, p. 1736, 2004.

[105] Angelescu, D. E., Waller, J., Register, R. A., and Chaikin, P. M. *Adv. Mater.*, vol. 17, no. 1878, 2005.

[106] Harrison, C., Cheng, Z., Sethuraman, S., Huse, D., Chaikin, P., Vega, D., Sebastian, J., Register, R., and Adamson, D. *Phys. Rev. E*, vol. 66, p. 011706, 2002.

[107] Park, C., Simmons, S., Fetters, L., Hsiao, B., Yeh, F., and Thomas, E. *Polymer*, vol. 41, p. 2971, 2000.

[108] Gupta, V., Krishnamoorti, R., and Kornfield, J. *Macromolecules*, vol. 28, p. 4464, 1995.

[109] Riise, B., Fredrickson, G., Larson, R., and Pearson, D. *Macromolecules*, vol. 28, p. 7653, 1995.

[110] Stangler, S. and Abetz, V. *Rheol Acta*, vol. 42, p. 569, 2003.

[111] Amundson, K., Helfand, E., Davis, D., Quan, X., and Patel, S. *Macromolecules*, vol. 24, p. 6546, 1991.

[112] Amundson, K., Helfand, E., Quan, X., and Smith, S. *Macromolecules*, vol. 26, p. 2698, 1993.

[113] Amundson, K., Helfand, E., Quan, X., Hudson, S., and Smith, S. *Macromolecules*, vol. 27, p. 6559, 1994.

[114] Morkved, T., Lu, M., Urbas, A., Ehrichs, E., Jaeger, H., Mansky, P., and Russell, T. *Science*, vol. 273, p. 931, 1996.

[115] Elhadj, S., Woody, J. W., Niu, V. S., and Saraf, R. F. *Applied Physics Letters*, vol. 82, no. 6, p. 871, 2003.

[116] Thurn-Albrecht, T., DeRouchey, J., Russell, T. P., and Jaeger, H. M. *Macromolecules*, vol. 33, p. 3250, 2000.

[117] Xu, T., Hawker, C., and Russell, T. *Macromolecules*, vol. 36, p. 6178, 2003.

[118] Böker, A., Knoll, A., Elbs, H., Abetz, V., Muller, A., and Krausch, G. *Macromolecules*, vol. 35, p. 1325, 2002.

[119] Brevel, E. *Journal of Materials Science*, vol. 38, p. 1347, 2003.

[120] Casavant, M., Walters, D., Schmidt, J., and Smalley, R. *Journal of Appled Physics*, vol. 93, p. 2153, 2003.

[121] Osuji, C., Ferreira, P., Mao, G., Ober, C., Vander Sande, J., and Thomas, E. *Macromolecules*, vol. 37, p. 9903, 2004.

[122] Naoki, T., Zhibao, L., Tomomichi, I., Corrie, T., Mitsu-aki, A., Masatoshi, T., and Watanabe, J. *Japanese Journal of Applied Physics*, vol. 44, p. L711, 2005.

[123] Bodycomb, J., Funaki, Y., and Kimishama, K. *Macromolecules*, vol. 32, p. 2075, 1995.

[124] Hashimoto, T., Bodycomb, J., Funaki, Y., and Kimishima, K. *Macromolecules*, vol. 32, p. 952, 1999.

[125] De Rosa, C., Park, C., Lotz, B., Wittman, J., Fetters, L., and Thomas, E. *Macromolecules*, vol. 33, p. 4791, 2000.

[126] De Rosa, C., Park, C., Thomas, E., and Lotz, B. *Nature*, vol. 405, p. 433, 2000.

[127] Ruoff, R., Tse, D., Malhotra, R., and Lorets, D. *J. Phys. Chem.*, vol. 97, p. 3379, 1993.

[128] Narayanan, T., *Synchrotron small-angle X-ray scattering, in Soft Matter: Scattering, Imaging and Manipulation*. Springer, 2007.

[129] Hamley, I. and Castelletto, V. *Progress in Polymer Science*, vol. 29, p. 909, 2004.

[130] Hammersley, A., "Fit 2d primer." http://www.esrf.eu/computing/scientific/FIT2D/.

[131] Huang, T., Toraya, H., Blanton, T., and Wu, Y. *J. Appl. Crys.*, vol. 26, p. 180, 1993.

[132] Campbell, D. and White, J., *Polymer Characterization*. Chapman and Hill, London, New York, 1989.

[133] "The transmission electron microscope." www.nobelprize.org.

[134] Palta, D., Bucknall, D., Leisen, J., and Beckham, H., "Effect of nanoparticle inclusions on the block copolymer morphology (to be submitted).".

[135] De Paul, S., Zwanziger, J., Ulrich, R., Wiesner, U., and Spiess, H. *J. Am. Chem. Soc.*, vol. 121, p. 5727, 1999.

[136] Ostrovskaya, L., Perevertailo, V., Ralchenko, V., Dementjev, A., and Loginova, O. *Diamond and related Materials*, vol. 11, p. 845, 2002.

[137] products, A., "Vca-optima xe system." Instruction Manual.

[138] Awada, H., Castelein, G., and Brogly, M. *Surface and Interface analysis*, vol. 37, p. 755, 2005.

[139] Krevelen, D., *Properties of Polymers - their correlation with chemical structure; their numerical estimation and prediction from additive group contributions*. Elsevier Science B.V., Amsterdam, The Netherlands, 3^{rd} ed., 1997.

[140] Ho, D. and Glinka, C. *J. Polym. Sci. : Part B: Polymer Physics*, vol. 42, p. 4337, 2004.

[141] Gervais, M. and Gallot, B. *Makromol. Chem.*, vol. 178, p. 1205, 1977.

[142] Canham, P., Lally, T., Price, C., and Stubbersfield, R. *J.C.S. Faraday I*, vol. 76, p. 1857, 1857.

[143] Pacific Nanotechnology, Inc., *Atomic force microscope - Instruction manual*, 2005.

[144] Levine, J., Cohen, J., Chung, Y., and Georgopoulos, P. *Journal of Applied Crystallography*, vol. 22, p. 528, 1989.

[145] Busch, P., Posselt, D., Smilgies, D., Rauscher, M., and Papadakis, C. *Macromolecules*, vol. 40, p. 630, 2007.

[146] Hamilton, W. *Current Opinion in Colloid and Interface Science*, vol. 9, p. 390, 2005.

[147] "Grazing incidence small angle x-ray scattering." Webpage of Dr. Detlef Smilgies (www.chess.cornell.edu).

[148] Schreiber, F., "X-ray and neutron reflectivity for the investigation of thin films." Website. www.physchem.ox.ac.uk/ fs.

[149] Ahn, H., Cuong, P., Park, S., Kim, Y., and Lim, J. *Wear*, vol. 255, p. 819, 2003.

[150] Krappe, U., Stadler, R., and Voigt-Martin, I. *Macromolecules*, vol. 28, p. 4558, 1995.

[151] Chu, J., Rangarajan, P., Adams, L., and Register, R. *Polymer*, vol. 36, p. 1569, 1995.

[152] Sakurai, S., Mori, K., Okawara, A., Kimishima, K., and Hashimoto, T. *Macromolecules*, vol. 25, p. 2679, 1992.

[153] Bigioni, T., Lin, X., Nguyen, T., Corwin, E., Witten, T., and Jaeger, H. *Nature Materials*, vol. 5, p. 265, 2006.

[154] Vacatello, M. *Macromolecules*, vol. 34, p. 1946, 2001.

[155] Mays, J., Hadjichristidis, N., and Fetters, L. *Macromolecules*, vol. 18, p. 2231, 1985.

[156] Waller, J., Bucknall, D., Leisen, J., and Beckham, H., "Effect of fullerene c_{60} nanoparticle inclusions on the ps-pdms block copolymer morphology (to be submitted).".

[157] Green, P., Christenon, T., Russell, T., and Jerome, R. *J. Chem. Phys.*, vol. 92, p. 1478, 1990.

[158] Balsara, N., Garetz, B., Chang, M., Dai, H., and Newstein, M. *Macromolecules*, vol. 31, p. 5309, 1998.

[159] Lambooy, P., Russell, T., Kellogg, G., Mayes, A., Gallagher, P., and Satija, S. *Phys. Rev. Lett.*, vol. 72, p. 2899, 1994.

[160] Jacobs, K., Herminghaus, S., and Mecke, K. *Langmuir*, vol. 14, p. 965, 1998.

[161] Stange, T. and Evans, D. *Langmuir*, vol. 13, p. 4459, 1997.

[162] Barnes, K., Karim, A., Douglas, J., Nakatani, A., Gruell, H., and Amis, E. *Macromolecules*, vol. 33, p. 4177, 2000.

[163] Mackay, M., Hong, S., Russell, T., Hawker, C., Vestberg, R., and Douglas, J. *Langmuir*, vol. 18, p. 1877, 2002.